

Dynamic Atomic Scale Sintering of Nanoparticle Catalysts

Thomas Edward Martin

PhD

University of York
Physics

May 2015

Abstract

The classical view of a chemical reaction involves the formation and breaking of bonds, facilitated by the transfer of electrons between atoms. To fundamentally understand the mechanisms occurring, atomic resolution of the catalysts enabling the reaction is required. Using the recently developed York JEOL Nanocentre Environmental Scanning Transmission Electron Microscope, single atoms and nanoparticles can be observed in representative industrial reaction conditions, allowing for atomic scale quantification of catalyst deactivation mechanisms, such as Ostwald Ripening.

This is initially understood through the industrially important process of methanol synthesis. Copper nanoparticles, one component of a methanol synthesis catalyst, are imaged under both Hydrogen and high vacuum conditions. This is the first use of ESTEM to study sintering, which is shown to be governed by the Ostwald Ripening mechanism and significantly enhanced by the presence of Hydrogen. Further understanding is developed by comparison with kinetic models to deconvolute the variables affecting Ostwald Ripening.

In order to study Ostwald Ripening at the single atom scale in Hydrogen, Platinum nanoparticles are used as a model system. Particle decay is found to be initiated by a lack of local single atoms, and a subsequent increase in single atom density suggests anchoring of atoms onto sites on the Carbon substrate. These observations build an atomic level understanding of Ostwald Ripening, informing both traditional nanoparticle, and the emerging field of single atom, catalysis.

Contents

Abstract.....	2
Contents.....	3
List of Figures	6
List of Tables	10
Acknowledgements.....	11
Author’s Declaration	12
1. Introduction	13
1.1. Overview of Thesis	13
2. Electron Microscopy Techniques	15
2.1. Introduction	15
2.2. Basics of (S)TEM	16
2.3. In situ Electron Microscopy.....	20
2.4. The Importance of ESTEM.....	22
3. Nano to Single Atom Catalysis	23
3.1. Introduction	23
3.2. Deactivation by Sintering.....	24
3.3. Sintering Mechanisms.....	26
3.3.1. Identification by PSD.....	26
3.3.2. Identification by Individual Particle Observations	27
3.4. Ostwald Ripening Theory	28
3.5. Imaging Ostwald Ripening	31
3.6. Environmental Effects on Ostwald Ripening.....	32
3.7. Single Atom Catalysis	33

3.7.1.	Support methods	33
3.7.2.	Applications.....	34
4.	Activation of a Cu catalyst via Reduction.....	36
4.1.	Introduction	36
4.2.	Specimen Preparation.....	37
4.3.	ETEM Reduction of CuO.....	38
4.3.1.	Experimental Conditions.....	38
4.3.2.	Effect of H ₂ Pressure on CuO Reduction	40
4.3.3.	Reduction Mechanisms of CuO	42
4.4.	Characterisation of Cu Nanoparticles Post Reduction.....	49
4.4.1.	Electron Beam Effects	49
4.5.	Conclusions	53
5.	Ostwald Ripening of a Model Cu Catalyst.....	55
5.1.	Introduction	55
5.2.	Experimental Conditions.....	58
5.2.1.	Particle Size Measurement and Error Estimation	59
5.3.	Cu/Si ₃ N ₄ at 500°C in 3 Pa H ₂	59
5.4.	Local Correlation and Mean Field Models of Ostwald Ripening.....	64
5.5.	Kinetic Monte Carlo Simulations of Ostwald Ripening	70
5.6.	The Effect of H ₂ and Substrates on Ostwald Ripening	72
5.6.1.	Cu/Si ₃ N ₄ at 500°C in HV Conditions.....	72
5.6.2.	Cu/C at 500°C in H ₂	74
5.6.3.	Cu/C at 500°C in HV.....	78
5.6.4.	Cu/Al ₂ O ₃ at 500°C in H ₂ and HV.....	81
5.7.	The Effect of Temperature on Ostwald Ripening	87
5.7.1.	Cu/C at 550°C in H ₂	87
5.7.2.	Cu/C at 400°C in H ₂	93
5.8.	Interface and Diffusion Limits.....	96
5.9.	Conclusions	98

6.	Quantitatively studying Single Atoms using ESTEM	101
6.1.	Introduction	101
6.2.	Optimising Single Atom Resolution	102
6.3.	In situ Ostwald Ripening at the Single Atom Level	105
6.3.1.	Experimental Conditions.....	106
6.3.2.	Quantifying Single Atom Density	109
6.3.3.	Relating Particle Decay to Single Atom Density.....	113
6.3.4.	Application of Local Correlation Models.....	118
6.4.	Single Atom Density as a Function of Environment.....	120
6.4.1.	Effect of Particle Structure.....	122
6.5.	Conclusions	125
7.	Final Remarks and Further Work	127
	List of Acronyms.....	130
	List of Symbols	132
	Bibliography	134

List of Figures

Figure 2.1: Diagram of the different signals produced by the interaction of a high energy electron beam with a thin specimen.	16
Figure 2.2: Diagram of the real space (left) and diffraction (right) imaging in TEM.....	17
Figure 2.3: Diagram of a STEM showing the probe formation by the condenser and objective lenses and raster scanning from the scan coils.	18
Figure 2.4: (a) Defines the simple effect of aberration.....	19
Figure 2.5: Schematic diagram of the double aberration JEOL 2200FS microscope at the University of York.....	21
Figure 3.1: A schematic representation of the concentration of adatoms and energetics on the substrate and nanoparticle.	29
Figure 4.1: Ball and stick models of Cu (face centred cubic), Cu ₂ O (fcc) and CuO (monoclinic, with lattice constants a, b, c. Cu atoms are blue, O atoms are red.....	37
Figure 4.2: Selected Area Diffraction Pattern of CuO	38
Figure 4.3: In situ reduction of CuO, completed by 350°C, temperature ramp of 50 °C per 30 mins in 3Pa H ₂	40
Figure 4.4: (a) HRTEM of Cu ₂ O nanoparticle in 1Pa H ₂ , 250°C after 1 hour. FFT shows [011] orientation. (b) SADP at camera length of 40cm showing majority of sample is Cu ₂ O	41
Figure 4.5: Typical Cu nanoparticles post reduction in 3Pa of H ₂ at 250°C.	42
Figure 4.6: MTP nanoparticle showing Cu/CuO interface.	43
Figure 4.7: Reduction is proceeding within the nanoparticle.....	45
Figure 4.8: Reduction (at 250°C, 3Pa H ₂) appears to occur at the nanoparticle surface.....	47
Figure 4.9: (a) Nanoparticle edge from Figure 4.6, with Cu(020) exposed, shown by d=0.186nm (b) Nanoparticle edge from Figure 4.8, with Cu (111) exposed, shown by d=0.211nm (c) calculated atomic arrangement of Cu[011] with (111) and (020) labelled.	48
Figure 4.10: Nanoparticle with single twin boundary and lamellae twin observed at a rate of 1/5 minutes.....	51
Figure 4.11: Nanoparticle with single twin boundary observed continuously over 10 mins	52
Figure 5.1: Cu/Si ₃ N ₄ sintering via the Ostwald Ripening mechanism in 3 Pa H ₂	61

Figure 5.2: Experimental results for r less than 3.5nm at $t=0$. Error in r measurement is ± 0.14 nm.	62
Figure 5.3: Experimental results for r greater than 3.5nm at $t=0$. Error in r measurement is ± 0.14 nm.	62
Figure 5.4: $t(r=0)$ against $r(t=0)$. Anomalous extinction times are observed for particles 7 and 16 (dashed lines). Particle extinction times are also not size ordered for $r=2.5-3.5$ nm particles.	63
Figure 5.5: Voronoi construction overlayed on Figure 5.1. Nearest neighbour particles, as defined by the construction, contribute to the local single atom concentration.	65
Figure 5.6: Interface limited mean field assumption used with $E_{\text{Tot}}=222.34$ kJ/mol to model Cu/Si ₃ N ₄ at 500°C in 3 Pa of H ₂	66
Figure 5.7: Interface controlled local correlation assumption used with $E_{\text{Tot}}=217.90$ kJ/mol to model Cu/Si ₃ N ₄ at 500°C in 3 Pa of H ₂	67
Figure 5.8: Using the nearest neighbour bond additivity model [67], the average number of broken bonds per atom at the surface is calculated for pyramidal FCC particles at different values of r . The number of broken bonds for bulk FCC is 3.	68
Figure 5.9: Interface limited local correlation assumption with $\gamma(r)$ [69] used with $E_{\text{Tot}}=217.90$ kJ/mol to model Cu/Si ₃ N ₄ at 500°C in 3 Pa of H ₂	69
Figure 5.10: KMC simulation of right hand area of Figure 5.1.	71
Figure 5.11: Cu/Si ₃ N ₄ at 500°C in HV conditions after (a) 0 mins and (b) 300 mins.	73
Figure 5.12: Map of experimental area used for observations of Cu/C at 500°C in H ₂	74
Figure 5.13: Experimental results for r greater than 3.5nm at $t=0$. Error in r measurement is ± 0.11 nm.	75
Figure 5.14: Experimental results for r less than 3.5nm at $t=0$. Error in r measurement is ± 0.11 nm. Observation frequency is 5-10mins.	75
Figure 5.15: Interface limited mean field assumption used with $E_{\text{Tot}}=213.25$ kJ/mol with an error of 1.69kJ/mol.	77
Figure 5.16: Interface limited local correlation assumption used with $E_{\text{Tot}}=209.50\pm 2.39$ kJ/mol.	77
Figure 5.17: Diffusion limited local correlation assumption used with $D\cdot E_{\text{Tot}}=453.50\pm 3.02$ kJ/mol.	78
Figure 5.18: (a) Particles at $t=0$ mins, at 500°C in HV, (b) $t=190$ mins, (c) individual particle radii tracking, showing extinction of particles 4 and 8.	80
Figure 5.19: (a) 500°C, HV, PSDs with lognormal fits applied (b) 500°C, H ₂ , PSDs with lognormal fit applied to $t=0$ mins. $t=120$ mins may be LSW-type or a double peak.	81

Figure 5.20: Production of model α - Al_2O_3 system by heating an 8nm thick Al film heated at 570°C for 1 hour in 5mBar air. SADPs were taken with a camera length of 30cm.	82
Figure 5.21: Comparison of particle size change of Cu/ Al_2O_3 in HV at 500°C at t=0 minutes and t=150 minutes.	83
Figure 5.22: Cu on amorphous Al_2O_3 in H_2 at 500°C.	84
Figure 5.23: (a) AFM (Atomic Force Microscope) scan of Al_2O_3 film.	84
Figure 5.24: Observation of inverse Ostwald Ripening of Cu nanoparticles on Al_2O_3 in 3Pa H_2 at 500°C.	85
Figure 5.25: Reduction of the temperature over 10s from (a,c) 500°C to (b,d) 20°C in 3Pa H_2 environment (a,b) and HV environment (c,d) for a Cu/C sample.	86
Figure 5.26: Map of experimental area used for observations of Cu/C at 550°C in H_2	88
Figure 5.27: Experimental particle radii for Cu/C system at 550°C in H_2 . Error in r is 0.3nm, calculated using the method developed in section 5.2.1. Particles 9, 10 and 11 are excluded due to migration being observed.	88
Figure 5.28: Magnified area of Figure 5.27 in the r=0-8nm regions.	90
Figure 5.29: Interface controlled mean field model applied using $E_{\text{Tot}}=177.83\text{kJ/mol}$ with an error of 3.44kJ/mol. Particles displayed have an initial r less than 9nm.	90
Figure 5.30: Interface controlled mean field model applied using $E_{\text{Tot}}=177.83\text{kJ/mol}$ with an error of 3.44kJ/mol. Particles displayed have an initial r greater than 9nm.	91
Figure 5.31: Interface controlled local correlation model applied using $E_{\text{Tot}}=184.0\text{kJ/mol}$ with an error of 4.47kJ/mol.	91
Figure 5.32: Diffusion controlled local correlation model applied using $D \cdot E_{\text{Tot}}=432.95 \pm 1.55\text{kJ/mol}$	92
Figure 5.33: Experimental particle radii for Cu/C system at 400°C in H_2 . Error is 0.12nm.	94
Figure 5.34: Map of experimental area used for observations of Cu/C at 400°C in H_2	94
Figure 5.35: Interface controlled mean field model applied using $E_{\text{Tot}}=221.23 \pm 2.01\text{kJ/mol}$	95
Figure 5.36: Interface controlled local correlation model applied using $E_{\text{Tot}}=216.58 \pm 1.96\text{kJ/mol}$	95
Figure 5.37: Diffusion controlled local correlation model applied using $D \cdot E_{\text{Tot}}=387.00 \pm 2.16\text{kJ/mol}$	96
Figure 5.38: r is normalised by dividing by the average individual particle size. All individual particles are then plotted for each different temperature and material used in the previous sections.	97
Figure 5.39: AFM linescans of regions on Carbon, Silicon Nitride and Alumina supports.	98
Figure 6.1: Plot of the visibility v_{AB} of single atoms against different acquisition parameters.	104
Figure 6.2: Observation of PMC at 400°C in 3Pa H_2	107

Figure 6.3: (a) Low magnification (1.2MX) image of experimental area after 75 minutes at 250°C, 3Pa H ₂ . (b) 4MX high magnification image of the 23.5nm x 23.5nm experimental area after 75 minutes, (c) PSD with lognormal fits of low and high (d) magnification images, showing that the mean particle size agrees within error.	108
Figure 6.4: (Top): Single atom heat map from t=0 to t=50 mins, at which point no particles have become extinct.	111
Figure 6.5: (a) Heat map of single atoms from Figure 6.4 with a Voronoi overlay (b) single atom densities calculated using the Voronoi overlay instead of the raster.	112
Figure 6.6: Observations taken in 3Pa H ₂ at 250°C.	114
Figure 6.7: Size of particles 17 and 18 during experimental time frame of 75 minutes.	115
Figure 6.8: Single Atom density in individual Voronoi cells of particle 17 and 18.....	116
Figure 6.9: The single atom density in the nearest neighbour regions of particles 3 and 8.....	117
Figure 6.10: Particle radius (r) against time for experimental HAADF STEM observations of the smallest four particles.....	118
Figure 6.11: Application of the local correlation interface controlled model with surface free energy (γ) of 1.7J/m ² , E _{Tot} =190kJ/mol.....	119
Figure 6.12: Application of the local correlation diffusion controlled model with $\gamma=1.7J/m^2$, D·E _{Tot} =368kJ/mol.....	119
Figure 6.13: Temperature profile during the experiment with a count of the number of single atoms and particles observed in each case.	121
Figure 6.14: (a) Heated to 20°C with many disordered particles present. As temperature is increased to (b)200°C and (c) 400°C, the number of disordered particles decreases , and more crystallinity is observed.....	124
Figure 6.15: Histogram of Voronoi cell local single atom densities at 20°C and 400°C.....	125

List of Tables

Table 4.1: Experimental techniques and conditions used to study CuO reduction. Note that MMO indicates a mixed metal oxide, EELS (Electron Energy Loss Spectroscopy), XANES (X-ray Absorption Near Edge Structure).....	39
---	----

Acknowledgements

The work in this thesis has both challenged and excited me over the course of the last few years. Perhaps the explanation for both of these is the degree of freedom that my supervisors, Profs Ed Boyes and Pratibha Gai, have granted me to follow where I am interested in taking this project. They have been generous with their time, advice and the technical capabilities they have developed at the York JEOL Nanocentre, and I wish to thank them for this. I would also like to thank the EPSRC and BP for funding.

Thanks go to Dr. Leonadro Lari, Dr. Michael Ward and Ian Wright for their help in using the array of equipment available at the Nanocentre. I'm grateful to them, and the excellent community present at the Nanocentre, for interesting conversations over the past few years.

This degree is my second in York, but I was accompanied mostly by friends from my first. That is a testament to the quality of friendship provided by those people: Ric, Becca and Nick.

An acknowledgement here doesn't really sufficiently thank my fiancé, parents and sister for the level of support and guidance they have given me during, and prior, to this project. My parents have always prioritised me and my sister and it is their generosity that has given me the ability to complete this thesis. Lastly, to my soon to be wife, Lucy, thanks for your love, support and making the last few years so much fun.

Author's Declaration

I declare that the work presented in this thesis is based purely on my own research, unless otherwise stated, and has not been submitted for a degree in this or any other university.

Publications and Conference Talks

Martin, T.E., Gai, P. L., & Boyes, E.. Dynamic imaging of Ostwald Ripening using Environmental Scanning Transmission Electron Microscopy. ChemCatChem, 2015, In Press. doi:

10.1002/cctc.201500830R1

Martin, T. E., Lari, L., Gai, P. L., & Boyes, E. D. IT-7-O-1567 In situ Scanning Transmission Electron Microscopy study of CuO reduction. Conference Talk presented at the International Microscopy Congress 2014.

1. Introduction

Catalysis occupies a rare position due to its dual role influencing both the economic state of the world and future or current environmentally friendly solutions. Economic gains can often lead to a positive environmental influence by reducing: emissions; the quantity of precious metals required or the barrier to green technology (e.g. fuel cells).

One approach to improving catalytic technology is to understand highly complex industrial systems at the atomic level. This is often undertaken using simplified model systems in order to reduce the difficulty of obtaining a statistically significant result [1]. Over the past 10-20 years there have been several key developments in the techniques used to image catalysts at the atomic scale. For instance, in electron microscopy: spherical aberration correctors have led to greatly improved resolution [2, 3]; microscopes have been developed with gas environments surrounding the sample [4]; and micro-scale heating holders have allowed for improved temperature control [5].

This has enabled atomic scale resolution of catalysts in environmental conditions that are representative of those used industrially. As the nature of a catalyst active site, along with the processes by which it deactivates, has often been shown to change both in magnitude and mechanism with reaction environment [6]-it is of fundamental importance to observe a catalyst *in situ*.

The work presented in this thesis applies these recent advances in order to understand how activation and deactivation mechanisms of nanoparticle catalysts progress at the atomic scale.

1.1. Overview of Thesis

An explanation of the electron microscopy techniques used in later work is given in Chapter 2. This introduces the concept of Environmental Scanning Transmission Electron Microscopy and its application to catalytic nanoscience. This leads to an overview in Chapter 3 of nanoscale

down to single atom catalysis. The theory of Ostwald Ripening is discussed, which is the deactivation of catalysts by the movement of single atoms.

Prior to Ostwald Ripening, industrial catalysts require activation. This influences the size, crystallinity and distribution of the nanoparticles and is thus of critical importance for improving catalysts. The focus of Chapter 4 is on the activation via reduction of a Copper Oxide nanoparticle catalyst, which is of industrial relevance in methanol synthesis. This is followed in Chapter 5 by an exploration of the environmental dependencies of Ostwald Ripening and deconvolution of their impact via the use of kinetic models. The low atomic number of Copper restricts imaging at the single atom level and thus, in Chapter 6, Platinum is used as a model system to further understand the deactivation of nanoparticle catalysts through Ostwald Ripening at an atomic level.

2. Electron Microscopy Techniques

2.1. Introduction

Improving microscope resolution has been a goal sought after since the first microscopes were produced in the 17th century. However, as discovered by Abbe in 1873 (and then refined by Rayleigh in 1896), the resolution of a microscope is a function of the wavelength used for observing the sample. This is shown by the Rayleigh criterion [7], where R is resolution, λ is wavelength, n_r is refractive index and ϕ is the semi-angle of collection.

$$R = \frac{0.61\lambda}{n_r \sin \phi} \quad 2.1$$

In an optical microscope the wavelength used is in the visible portion of the EM (Electromagnetic) spectrum, thus $\lambda=400-700\text{nm}$. Resolution is therefore limited to approximately 200nm unless the wavelength used for observation is decreased. Shorter wavelength portions of the EM spectrum, for example x-rays, offer much increased resolution. However, electrons provide the advantage of reduced wavelength (enabling resolution 200,000 times better than optical microscopes), whilst allowing influence on their trajectory by virtue of charge.

The history of electron microscopy began with the creation of the first TEM (Transmission Electron Microscope) in 1931 by Ernst Ruska and Max Knoll. Since that time many excellent and comprehensive texts have been written dealing with the wide range of techniques that have been developed [7-11]. The purpose of this chapter is to provide a brief overview of TEM and STEM (Scanning Transmission Electron Microscope), which are used for the majority of the experimental work in chapters 4, 5 and 6.

2.2. Basics of (S)TEM

In a TEM or a STEM the electrons are generated by either heating (thermionic emission) or application of an electric field (field emission) and pass through a series of electromagnetic lenses en route to the sample.

There are multiple ways in which the incoming electrons interact with matter [8], shown in Figure 2.1. Forward scattered electrons are used for imaging while the energy loss from inelastically scattered electrons can be measured by a spectrometer. This is called Electron Energy Loss Spectroscopy (EELS). Incident electrons can also excite atoms into higher energy states, which then returns to its ground state and emits an x-ray. Chemical composition can then be determined by measuring the energy of the x-ray- this is called energy dispersive x-ray spectroscopy (EDX). The detector generates a voltage pulse which is proportional to the x-ray energy and therefore characteristic of a certain element.

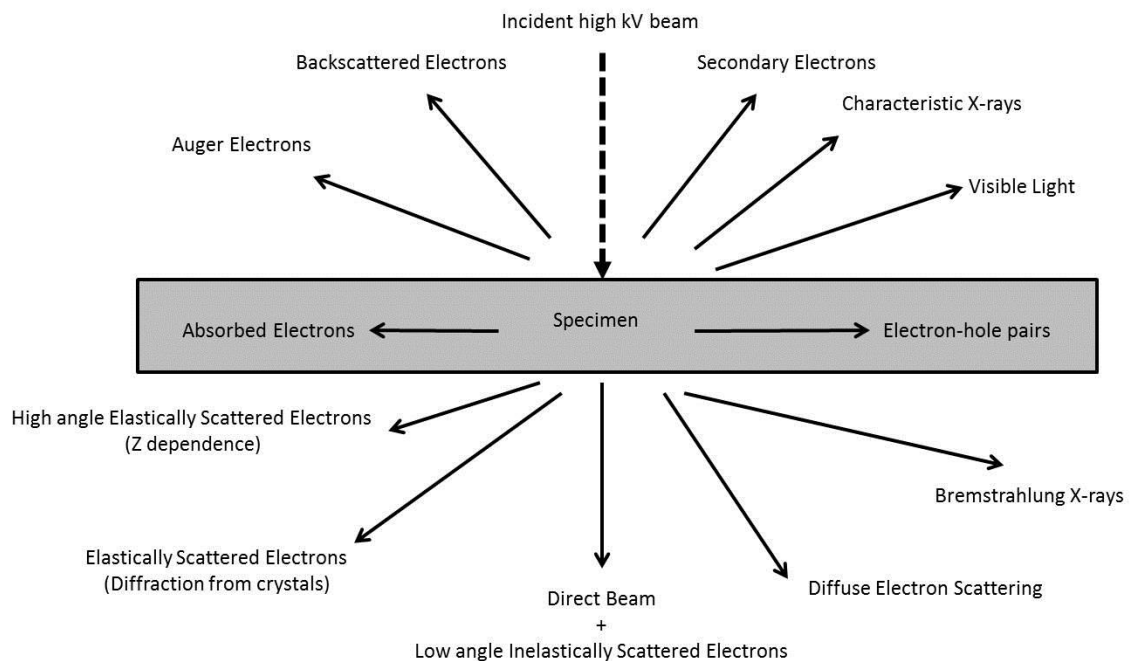


Figure 2.1: Diagram of the different signals produced by the interaction of a high energy electron beam with a thin specimen. Reproduced from [7].

Subsequent to generation, the electron beam passes through a series of condenser lenses which control the minimum spot size that is obtainable in the microscope and the beam convergence at the specimen. In TEM, the electrons are then projected as a parallel beam which is scattered by the sample, with transmitted electrons subsequently collected by the objective lens. In Figure 2.2, a simple schematic shows how the microscope can be switched

between real space imaging and diffraction modes by changing the strength of the intermediate lens.

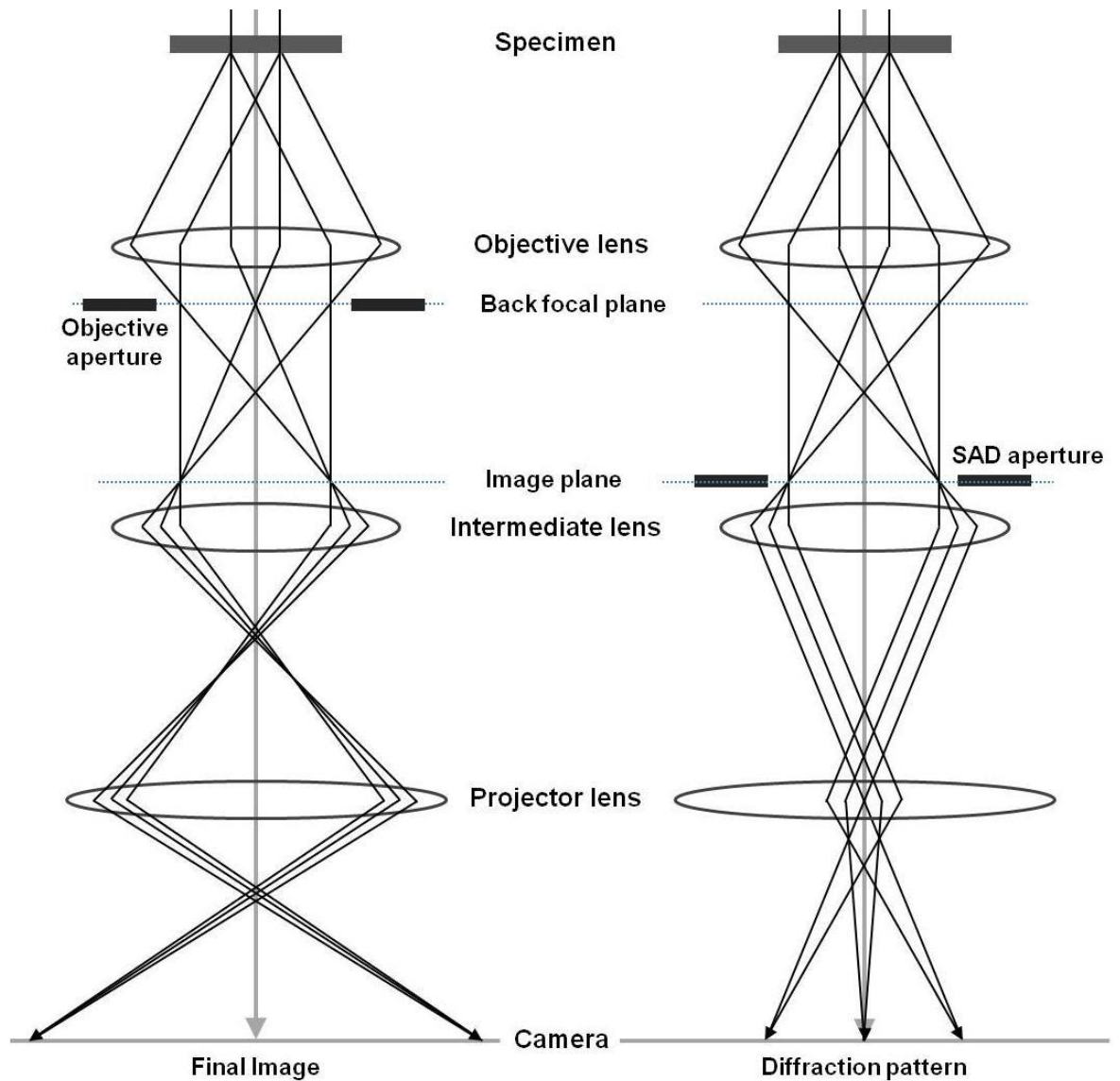


Figure 2.2: Diagram of the real space (left) and diffraction (right) imaging in TEM. Reprinted from [12]

The difference between STEM and TEM derives mostly from the fact that a STEM uses a small probe of electrons, focussed by the objective lens above the specimen, to raster scan across a sample. The resolution in STEM is limited by the electron probe size, which in turn is dependent on the lenses used to form the probe and the characteristics of the method used to accelerate the electrons. The lenses subsequent to the sample do not contribute to the performance of the instrument and thus the system has advantages in terms of flexibility of imaging conditions and a reduction in the number of resolution determining components. The STEM offers several other advantages over TEM in terms of the different signals that are

generated. Perhaps the most useful of these is a High Angle Annular Dark-field (HAADF) detector which enabled the first single atom detection by Crewe *et al.* [13]. The contrast of the signal is dependent upon the thickness of the sample and approximately the atomic number (Z) squared. This is often referred to as a Z -contrast image. There have been discrepancies between the observed and expected intensities from Z -contrast images and this disagreement in the Z power is referred to as the Stobbs factor [14].

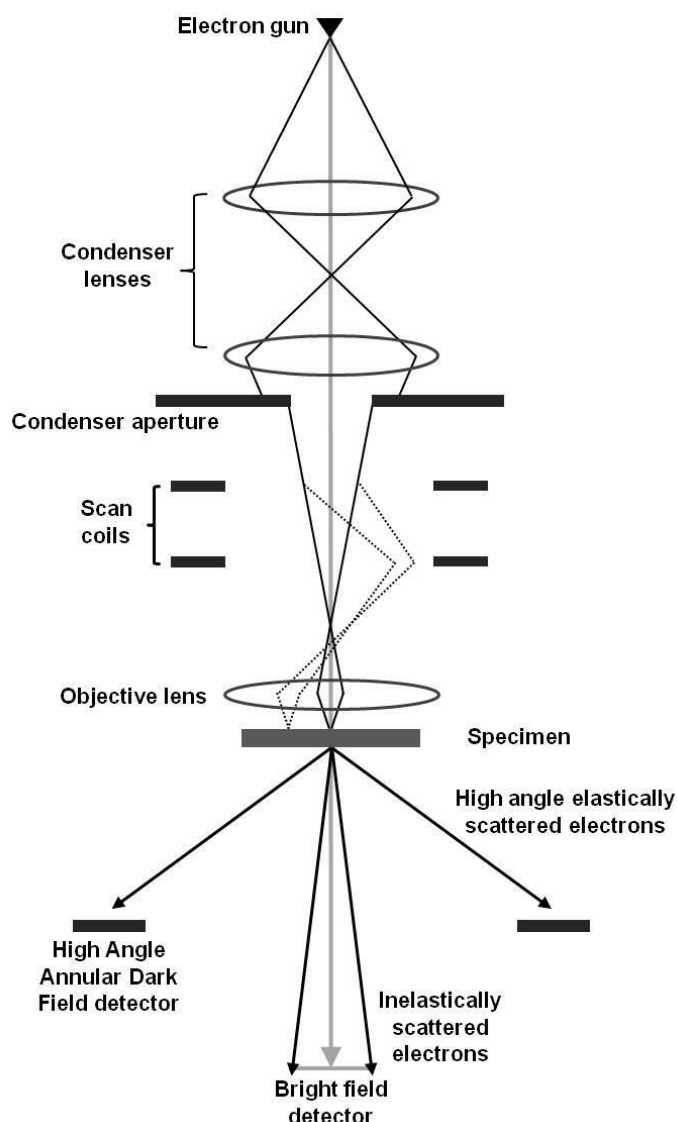


Figure 2.3: Diagram of a STEM showing the probe formation by the condenser and objective lenses and raster scanning from the scan coils. Reprinted from [12]

Another benefit of STEM is that EDX data can be obtained with spatial information about the acquired image. EDX has a spatial resolution limited by the ability to focus the beam of electrons in TEM and only allows for a spectrum of the beam illuminated area to be obtained.

In STEM the beam is already focused and thus spatial resolution at the sub-nanometre scale is achievable.

In the past decade the achievable resolution in (S)TEM has more than doubled, allowing sub Angstrom resolution [15]. The reason for this progress is the ability to correct major geometrical aberrations of the lenses, the most significant two being spherical and chromatic aberrations [11, 16] (Figure 2.4). The advantage of spherical aberration correction can be seen in Figure 2.4(d), where a plot of the phase contrast transfer function of a typical TEM is shown. At the points where the uncorrected systems (B) transfer function=0, no contrast is given, causing some spatial frequencies to be omitted. When aberration correction is applied (A), all spatial frequencies down to the information limit are incorporated.

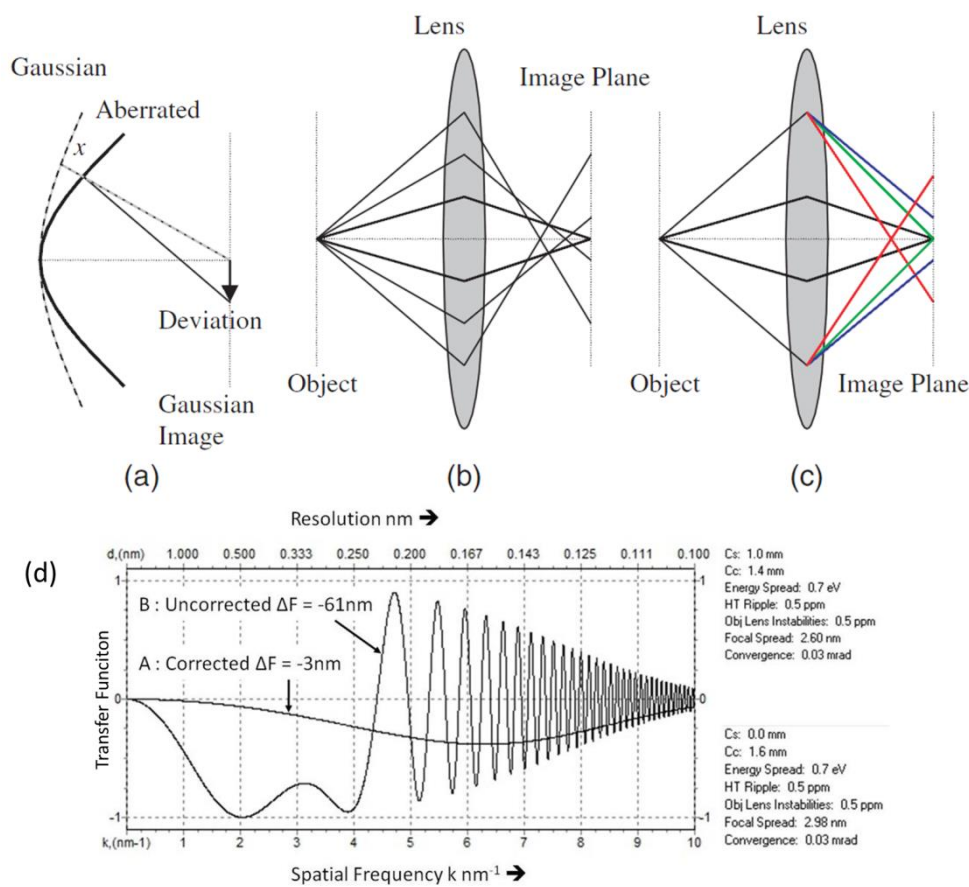


Figure 2.4: (a) Defines the simple effect of aberration. (b) Electrons incident at high angles are focussed too strongly due to spherical aberration. (c) Electrons with different energies are not focussed to the same positions, thus producing chromatic aberrations.(d) shows the calculated Contrast Transfer Function for a typical TEM in the uncorrected (B) and aberration corrected (A) conditions. Image is reprinted from [11].

The methods attempted to correct spherical aberrations vary considerably in their approach. The work by Gabor [17] on electron holography to correct aberrations won the Nobel Prize in

Physics in 1971 and led to optical holography once the laser had been developed in the 1960's. Removal of aberrations through image processing has also been attempted. One example of this is via a through focal series reconstruction method [18, 19], which works well for TEM images. However, the most complete solution is to introduce negative spherical aberration which combines with the objective lens aberrations to produce a total zero spherical aberration (note that in practice slight aberration remains and is desirable). Spherical aberration correction was originally formulated by Scherzer in 1947 [20] but was not implemented (partially because of limited computing power) until the 1990s by Haider *et al.* [3] for TEM and by Krivanek *et al.* [2] for STEM. The basic principle of spherical aberration correction is to introduce non rotational symmetry into the electron path. This is done by use of a multipole series to create an asymmetric magnetic field. Chromatic aberration is then reduced by minimising the energy spread of the electron beam [21].

2.3. In situ Electron Microscopy

A major drawback of conventional electron microscopy is that it requires HV (high vacuum) conditions for operation of the electron source. Also, interaction of electrons with matter (apart from the sample) degrades the image quality. This is obviously the converse of industrial conditions for heterogeneous catalysts, where pressures of up to 200 bars [22] can be experienced. To provide observation of a catalyst in TEM during a reaction then two different approaches have been taken.

The first of these uses a windowed cell where the sample is enclosed between two thin films, typically around 50nm in thickness [23] and composed of Silicon Nitride [5, 24, 25] or amorphous Carbon [26]. The gas (or liquid) is inserted through tubing systems which run through the specimen holder to provide pressures greater than 50 Torr [5, 23]. Despite the high pressure achievable, the windowed cells suffer from electron scattering by the enclosing material; although atomic resolution has recently been achieved [5, 23].

The second ETEM (Environmental TEM) approach was developed by Boyes and Gai using a differential pumping system [27]. This provided resolution of 0.23nm whilst allowing for pressures up to 50 mbar and temperatures (using a hot stage) of up to 1000°C. The design included an objective lens polepiece with radial holes allowing for the first stage of differential pumping. Molecular drag or turbomolecular pumps are then connected between apertures to permit high gas pressure close to the sample, whilst maintaining HV conditions in the rest of

the microscope. Further improvements were obtained to provide resolution of 0.14nm [28], before aberration correctors were developed [2, 3] and incorporated in ETEMs [29-31].

Boyes and Gai recently extended their original designs to incorporate double aberration correction, with both probe and image aberration correctors. The Environmental (Scanning) Transmission Electron Microscope (E(S)TEM) at the University of York is therefore the first double aberration corrected microscope which can provide sub angstrom resolution in both STEM and TEM modes [32]. The microscope can currently provide gas pressures of approximately 0.1mbar which equates to upwards of 10^4 monolayers of gas per second. Imaging nanoparticles at high temperatures in a reactant gas atmosphere allows for the dynamics of chemical reactions to be explored, but limits the total imaging time available. A compromise must be reached between obtaining high resolution images with large acquisition times, and the need to reduce beam damage or capture rapidly evolving intermediate states. Part of the solution to this is aberration correction.

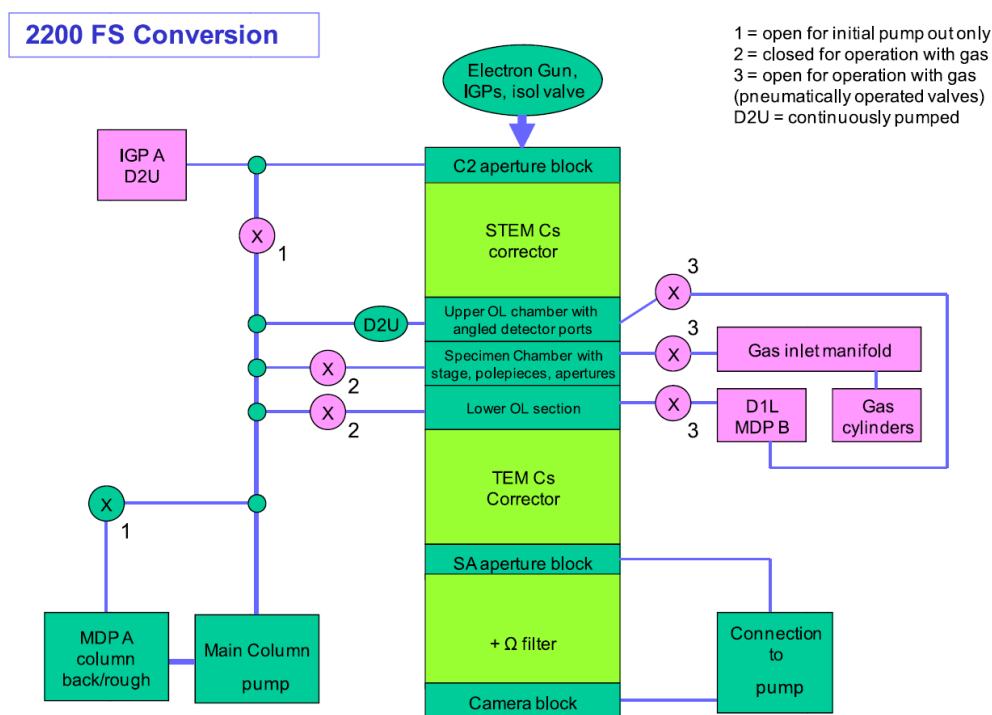


Figure 2.5: Schematic diagram of the double aberration JEOL 2200FS microscope at the University of York. Reprinted from [33].

The development of sub-Angstrom level resolution ESTEM is enabled by the probe size reduction from spherical aberration correction. However, the resolution is also limited by

sample drift. Traditionally a furnace type heater has been used which consists of a heated ceramic ring below the specimen. Unfortunately, there is no compensation for heat loss to the specimen tip or the gas environment. Recently, a new MEMS (micro-electromechanical system) heating holder [5] has been developed which minimises thermal drift in the specimen (due to the smaller volume being heated), gives more accurate temperature reading (due to a resistance feedback loop) and enables faster temperature increases (seconds as opposed to 30 minutes). This provides observation of a single specimen area during a heating experiment with minimal thermal drift.

2.4. The Importance of ESTEM

Catalytic reactions take place at the atomic level, yet understanding is often limited to observations of particles and supports. Despite considerable effort, the identification of catalyst active sites is still poorly understood [34]. The issue is complicated by the broad size distributions of typical industrial catalysts which often contain several different active sites, reducing the selectivity of the system [34, 35].

There has thus been a focus towards controlling and reducing the size of nanoparticles in order to improve their reactivity and specificity. Low coordination sites on kinks, corners and steps are more probable on smaller nanoparticles, which often enhances the activity of the catalyst [6]. This approach also provides an additional economic benefit by minimising the quantity of precious metal used.

Taking this idea to its fundamental level leads to the concept of single atom catalysts (SACs) [35-39], currently an area of great interest. It has recently become possible to prepare and characterise SACs in model systems [37], however their industrial relevance is limited due to a lack of understanding of the aggregation that occurs with ageing [34, 35].

ESTEM is the only technique capable of obtaining direct information about SACs in industrially representative conditions [32, 33, 36, 40]. When applied to nanoparticle catalysts, observation down to the single atom scale is attainable. ESTEM can provide unique insights in atomic scale catalysis and the following chapter will explore this potential.

3. Nano to Single Atom Catalysis

3.1. Introduction

Catalysis research is an extremely broad field, which only becomes wider once its application to the chemical industry is considered. Industrial catalysts aid more than 90% of the world's chemical manufacturing processes [41] and it is therefore important to understand how electron microscopy (and specifically ESTEM) fits within this expansive tapestry.

Starting with the fundamentals, industrial catalysts can be divided into two types: heterogeneous and homogenous. A homogenous catalyst involves the reaction of two species in the same phase e.g. liquid and liquid, whereas heterogeneous reactions involve different phases e.g. gas and solid. The benefits of a catalyst can be broadly conceptualised in two ways. Firstly, the catalyst provides a common surface for reactant molecules to bind to, thus significantly increasing the probability of reaction. Secondly, an alternative reaction pathway with lower activation energy may become accessible via bonding with a catalyst, reducing the reaction temperature and often improving selectivity.

Simplified models of chemistry often state that catalysts increase the rate of chemical reaction without undergoing any permanent change. Unfortunately, there are many ways in which a catalyst's activity will change with time; these are called deactivation mechanisms. The reaction rate is proportional to the active surface area of a catalyst and the deactivation mechanisms of catalysts reduce this area in several different ways: mechanical, chemical or thermal. Mechanical deactivation occurs when the catalyst surface becomes coated in reaction by-products, meaning that reactant molecules cannot access the catalyst active site. Chemical deactivation occurs when the binding of a reactant or product molecule is very strong and blocks the active site for use by other reactant molecules. The final mechanism is thermal deactivation, or sintering.

3.2. Deactivation by Sintering

Sintering is the thermally activated growth of (in this case) supported metal nanoparticles driven by a reduction in the surface free energy [42-44]. The reduction in total surface area due to an increase in the mean particle size causes a decrease in the surface to volume ratio of catalysts. Sintering is a significant deactivation mechanism in many catalytic processes and as such a fundamental understanding of it is of paramount importance due to the drastic economic consequences of reduced activity (and often selectivity) of industrial catalysts.

The instability of catalysts which causes sintering is a result of the increased Gibbs free energy with decreasing particle size. The common expression for the Gibbs free energy (G) is given in equation 3.1, where T is the temperature of the system, S is the entropy, P is pressure and V is volume. The final term is a sum of the chemical potential of the i^{th} atom (where there are n different atoms) μ_i over the number of atoms of that element N_i .

$$dG = TdS + PdV + \sum_{i=1}^n \mu_i dN_i \quad 3.1$$

Equation 3.1 describes a macroscopic system where the surface effects are negligible compared to the bulk. The energy attributed to surface molecules is obviously different to those in bulk, thus when observing a system at the microscopic scale a term must be introduced to correct for the difference in bulk and surface molecules. This is shown in equation 3.2, where γ is surface free energy per surface area (A).

$$dG = TdS + PdV + \sum_{i=1}^n \mu_i dN_i + \gamma dA \quad 3.2$$

At constant T,P and N the surface energy can be expressed as

$$\gamma = \left(\frac{\partial G}{\partial A} \right)_{T,P,N} \quad 3.3$$

Whilst at constant T and P the chemical potential μ can be expressed as

$$\mu_1 = \left(\frac{\partial G}{\partial N_1} \right)_{T,P,N_{i \neq 1}} \quad 3.4$$

Combining equations 3.3 and 3.4 yields the chemical potential of the surface, μ_A , assuming equilibrium and constant temperature and pressure.

$$\mu_A = \gamma \left(\frac{dA}{dN} \right)_{T,P} \quad 3.5$$

Assuming that the body in question is spherical and of radius r , the surface area $A=4\pi r^2$. The differential form of this is thus

$$dA = 8\pi r dr \quad 3.6$$

The volume per atom, V , can be expressed as

$$NV = \frac{4}{3}\pi r^3 \quad 3.7$$

$$\frac{dN}{dr} = \frac{4\pi r^2}{V} \quad 3.8$$

This then yields,

$$\mu_A = \gamma \frac{8\pi r dr}{\frac{4\pi r^2}{V} dr} = \frac{2\gamma V}{r} \quad 3.9$$

The total chemical potential of a single particle μ_r can be defined as the sum of the surface (μ_A) and bulk (μ_∞) contributions to the chemical potential.

$$\mu_r = \mu_\infty + \mu_A \quad 3.10$$

As expected, as $r \rightarrow \infty$, $\mu_r \rightarrow \mu_\infty$ for the macroscopic system.

Combining equations 3.9 and 3.10 leads to the Gibbs Thomson (GT) relationship, equation 3.11, where particle radius is shown to be inversely proportional to the particle's chemical potential [12, 43, 45].

$$\mu_r - \mu_\infty = \frac{2\gamma V}{r} \quad 3.11$$

Defining the chemical potential as equation 3.12, where S is the entropy, it is obvious that the increase in particle radius (thus a decrease in chemical potential) is driven by maximising the entropy of the system.

$$\mu = -T \left(\frac{\partial S}{\partial N} \right)_{P,V} \quad 3.12$$

3.3. Sintering Mechanisms

Two main mechanisms affect particle growth. These are 1) growth by particle migration and coalescence (PMC) and 2) Ostwald ripening (OR) [46]. Particle migration follows a Brownian type motion resulting in coalescence if two particles come into contact, in order to reduce the surface area and thereby the surface free energy of the system. OR is the emission of small clusters of atoms or single atoms by smaller particles which then increase the size of larger particles. This is due to the inverse relationship of chemical potential to the particle radius in the Gibbs-Thomson relationship. Smaller particles release single atoms in order to reduce their surface free energy and the atoms have a greater probability of interacting with larger particles, therefore resulting in a net movement of mass to larger particles [42].

3.3.1. Identification by PSD

The kinetics of OR are governed by Lifshitz-Slyozov-Wagner (LSW) theory [47] which results in a particle size distribution (PSD) with an asymmetric skew towards lower particle sizes and a cut off in the distribution at greater than twice the mean diameter [48, 49]. The PSD for the PMC mechanism was determined by Granqvist and Burrman [50] and shown to be a log normal distribution function. The assumption made is that the change in volume between each collision of particles is a random variable so:

$$V_j - V_{j-1} = \epsilon_j V_j \quad 3.13$$

where ϵ_j is a set of mutually independent random variables, V is the volume of the particle and j denotes the step number (assuming the collision process can be modelled as a discrete event). After j collisions the volume of the particle is thus:

$$V_j = V_0 \frac{1}{1 - \epsilon_1} \times \dots \times \frac{1}{1 - \epsilon_j} \quad 3.14$$

Taking the logarithm of equation 3.14 means that $\ln(V_j/V_0)$ becomes a sum of independent random variables. From central limit theorem it is known that this is a Gaussian. Particle coalescence therefore conforms to a lognormal distribution function.

Coalescence usually occurs via the formation of a neck which facilitates the movement of mass between the two particles [51]. The relaxation times for particle coalescence have been

studied by Wynblatt and Gjostein [43]; and Ruckenstein and Pulvermacher [52]. Both studies agree that the melting point of the particle increases with particle diameter leading to smaller particles undergoing faster coalescence events.

The obvious differences in the PSD of the PMC and OR mechanisms should provide the ability to differentiate between the mechanisms occurring in a system by observing the PSD. However the simulations of OR by De Smet *et al.* [53], did not corroborate the asymmetric skew towards lower particle diameters seen for an LSW distribution [54].

The ability to infer mechanism by PSD was questioned by Wanke [55], who argued that factors such as sintering being a function of initial particle distribution prevents the differentiation between OR and PMC via PSD. Wanke [55] also suggested that TEM artificially limits the PSD due to the resolution limits for particle radii below 1.5nm [56, 57]. This was further corroborated by Datye *et al.* [48] who biased experiments to favour the OR mechanism when sintering a Pd catalyst, and the PMC mechanism when sintering a Pt catalyst. This resulted in a log normal distribution for all PSDs, which was believed to derive from the Taylor series expansion of the GT equation. By using the GT equation in its exponential form (with no Taylor expansion) Jak *et al.* [58] derived an OR PSD with no left skew. The conclusion of Datye along with [55, 58, 59] is that PSDs are not a definitive method to deduce sintering mechanism, unless the initial PSD is well controlled, as performed by Wettergren *et al.* [60].

3.3.2. Identification by Individual Particle Observations

A recent approach by Hansen *et al.* [42, 46] to determining sintering mechanisms using ETEM looks at the change in individual particle size with time. A step in particle size indicates the PMC mechanism, whereas a gradual change is indicative of OR. The result of KMC (Kinetic Monte Carlo) simulations show the smallest particles lose mass, whilst the largest particles steadily increase in size. A similar study by Simonsen *et al.* [61] using ETEM reaches the same conclusion. However, both studies contain peak to peak changes in particle size of approximately 0.5nm, thus the determination of sintering mechanism from changes in the particle size gradient is difficult due to noise. Using TEM also limits the magnification (due to the phase contrast dependence) and therefore restricts the sample size. The use of ESTEM should allow for improved particle size measurement and a greater FOV (field of view) due to the Z-contrast dependence. Particle imaging down to the single atom level is possible, thus providing improved understanding of particle extinction.

The original theory for OR formulated by Wynblatt and Gjostein (WG) [43] provides information on the change in size of individual particles with time. By comparing the theoretical results with those obtained experimentally, it is possible to deconvolute factors that are not incorporated into OR theory. Previous work has looked at the influence of local particle size [1, 44, 61-66]; the change in surface free energy with particle size [67]; the influence of gas environment [68-70] and the OR rate dependence on surface chemistry and morphology [71]. Other studies have attempted to construct an extremely simple (ideally with only a single variable) model system and then verify OR theory. For example, Wettergren *et al.* [60] controlled OR by using bimodal and unimodal PSDs to drive or inhibit sintering in each case. Another approach by Alloyeau *et al.* [72], was to control the chemical composition of CoPt nanoparticles. As the Pt adatom migration speed is greater than Co, the fractional Pt composition of larger nanoparticles increases as OR proceeds. The approach taken in these studies is to modify the original Wynblatt-Gjostein equations to improve their experimental relevance. To explore this, the origins of OR theory must be understood.

3.4. Ostwald Ripening Theory

In the following, the outline of the Wynblatt-Gjostein OR equations is given. In this work, nanoparticles are assumed to be hemispherical and thus the volume is given by $V=2/3\pi r^3$, with a surface area of $S_A=2\pi r^2$.

Assuming that the total catalyst mass is conserved; there are two important rates to observe. The first is the net rate at which single atoms attach to the nanoparticle from the substrate (J_r) and the second is the net rate at which single atoms diffuse toward the nanoparticle on the substrate (J_s).

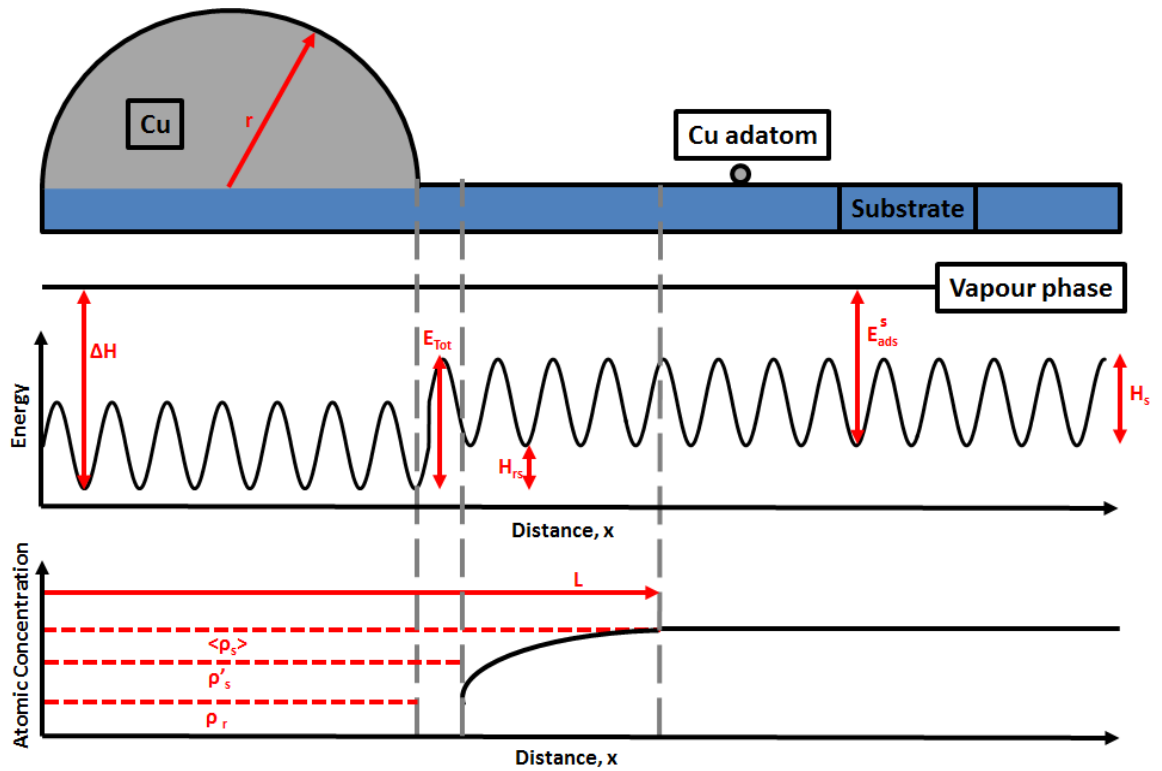


Figure 3.1: A schematic representation of the concentration of adatoms and energetics on the substrate and nanoparticle. Note that E_{Tot} is the heat of sublimation of the metal (ΔH) minus the energy of adsorption of a metal adatom (E_{Ads}^s) on the substrate plus the activation energy for diffusion of the adatom on the substrate surface (H_s).

The concentration of adatoms on the substrate sites adjacent to the particle is ρ_s and $\langle \rho_s \rangle$ is the concentration at L , the distance for the concentration to be a function of the average particle size, referred to as the critical radius r_c (as opposed to r). The concentration of adatoms on the edge of the particle is given by ρ_r . Using the GT relation (equation 3.11) ρ_r and $\langle \rho_s \rangle$ can be expressed as

$$\langle \rho_s \rangle = \rho_s^\infty e^{\left(\frac{2\gamma\Omega}{kTr}\right)} \quad 3.15$$

$$\rho_r = \rho_r^\infty e^{\left(\frac{2\gamma\Omega}{kTr}\right)} \quad 3.16$$

The rates for adatom movements are given by

$$\beta = \frac{v_r}{v_s} e^{\left(\frac{-H_{rs}}{kT}\right)} \quad 3.17$$

$$\beta' = v_s e^{\left(\frac{-H_s}{kT}\right)} \quad 3.18$$

where ν_s and ν_r are the vibrational frequencies of atoms on the support and on the particle, respectively. From Figure 3.1, H_s is the energy barrier between support sites, H_{rs} is the energy barrier between a support site and the particle edge site, Ω is the atomic volume, k is Boltzmann's constant and T is the temperature. The rate at which atoms attach to the particle is then given by the adatom concentration near to the particle (i.e. at x is greater than L) $\rho'_s a S \beta'$, where a is the interatomic spacing (distance between binding sites). The rate of single atoms leaving the particle is then given by $\rho_r a S \beta' \beta$, so that the net rate of addition to particle (J_r) is

$$J_r = \rho'_s a S \beta' - \rho_r a S \beta' \beta = 2\pi r a \beta' (\rho'_s - \rho_r \beta) = X_I (\rho'_s - \rho_r \beta) \quad 3.19$$

Where X_I can be thought of as a coefficient for adatom addition to the particle. The rate of single atom migration (J_s) through a circle with radius x around the particle is given by Fick's diffusion law:

$$J_s = 2\pi x D \left(\frac{d\rho}{dx} \right) \quad 3.20$$

Integrating x between r and L (corresponding concentrations of ρ'_s and $\langle \rho_s \rangle$) then gives

$$J_s = \frac{2\pi D (\rho'_s - \langle \rho_s \rangle)}{\ln \left(\frac{L}{r} \right)} = X_D (\rho'_s - \langle \rho_s \rangle) \quad 3.21$$

Where X_D can be thought of as a coefficient for adatom migration over the substrate. The adatom concentration close to the particle, ρ'_s , can be expected to equilibrate quickly (as it is a small region). Therefore the assumption of $d\rho'_s/dt=0$ can be made and equations 3.19 and 3.21 used to solve for ρ'_s .

$$X_D (\rho'_s - \langle \rho_s \rangle) = X_I (\rho'_s - \rho_r \beta) \quad 3.22$$

$$\rho'_s = \frac{X_D \langle \rho_s \rangle - X_I \rho_r \beta}{X_D - X_I}$$

Substituting this into equations 3.19 gives

$$J_r = \frac{X_D X_I}{X_D - X_I} (\langle \rho_s \rangle - \rho_r \beta) \quad 3.23$$

The original work by WG (Wynblatt-Gjostein) [43] only uses the first two terms of the Taylor expansion applied to the exponential term in the GT equation 3.15. However, Campbell *et al.* [67] showed that this assumption is incorrect for particles with radii below 5nm and thus to

accurately model systems in this size regime the GT relation must not be simplified. Thus, using equations 3.15, 3.16 and 3.23

$$J_r = \frac{X_D X_I}{X_D - X_I} \left(\rho_s^\infty e^{\left(\frac{2\gamma\Omega}{kTr}\right)} - \beta \rho_r^\infty e^{\left(\frac{2\gamma\Omega}{kTr}\right)} \right) \quad 3.24$$

In the case where the migration of adatoms is rapid, then X_D is much greater than X_I . This is referred to as the interface limited case. The diffusion limited case occurs when X_I is much greater than X_D . The mass in nm^3 that is added to the particle per second is then J_r multiplied by the atomic volume, Ω . Relating this to the volume change of the hemispherical particle yields equation 3.25, which can be combined with equation 3.24 to provide the rate of change of the particle radius, r , in either the interface or diffusion limited regimes.

$$\frac{dV}{dt} = \frac{d}{dt} \left(\frac{2}{3} \pi r^3 \right) = 2\pi r^2 \left(\frac{dr}{dt} \right) = \Omega J_r \quad 3.25$$

3.5. Imaging Ostwald Ripening

As discussed in section 3.3.1, investigating Ostwald Ripening using PSDs can often lead to misleading results due to variations in the initial PSD and TEM resolution limits [48, 55-57]. TEM images only represent a projection of the sample in the direction of the beam and are dependent on phase contrast. Heinemann and Soria [73] established in the 1980's that the visibility of small particles of around 1nm depends very strongly on the imaging conditions so that if astigmatism, focus or specimen drift are not optimised, the particle is indistinguishable from the support. TEM aberration correction reduces, but does not eliminate, this problem.

Many small particles are therefore undetectable above the noise from the substrate due to weak contrast. This artificially averages PSDs by cutting off nanoparticles below the resolution limit, but unfortunately also has the potential to skew more recent approaches that track particle size with time using (E)TEM [42, 44, 46]. Equation 3.24 has an $\exp(1/r)$ dependence which results in asymptotic particle decay prior to extinction. It is difficult to corroborate this model, however, as if a particle becomes undetectable below a certain critical size, the size trace will always appear to have an $\exp(1/r)$ dependence. Since the development of aberration corrected HAADF STEM, there has been a trend towards using this technique to image small supported metallic nanoparticles [74]. Zhang *et al.* [75] show the drastic difference in contrast capability between HAADF STEM and TEM, and its effect on the measured PSD.

3.6. Environmental Effects on Ostwald Ripening

The study of Ostwald Ripening is complicated by the number of different variables in the systems of interest. The rate of ripening is affected by nanoparticle material and size, as well as the support, the temperature and the reaction environment.

Firstly, discussing the support, there are two aspects of support morphology (independent of material) that affect sintering: these are roughness magnitude and roughness homogeneity. Both will be explored in chapter 5. Industrial catalysts often contain pores (sometimes by design), which provide a large surface area and greater distances between particles. There are also surface defects, steps and contaminants that inhibit the migration of particles or single atoms [59]. Clearly, the binding between the nanoparticle and support provides significant influence on the sintering rate and method. The effect of the support has proven to be very difficult to establish experimentally due to the large variation in both materials studied and in the preparation methods utilised [1].

The temperature has a clear effect on OR (equation 3.24) through the GT relation. Perhaps because of this, verification of the theory against an experimental temperature range has surprisingly not previously been studied. This will be elaborated on in chapter 5.

It is commonly thought that the presence of reactants will affect the rate of emission and migration of single atoms [69, 76-78]. One example relevant to the Cu systems that will be studied in chapters 4 and 5 is the Cu/ZnO catalyst used by Hansen *et al.* [79]. Reversible morphological changes were observed of a Cu nanoparticle in different gas environments. A change in shape will clearly influence the coordination number of individual atoms, and therefore affect the emission probability. Other examples include the dissociation of Cu and Ni clusters on TiO₂ after exposure to O₂, [80], the enhanced atomic Pt migration in oxidising conditions [48], Ostwald Ripening of Pt in O₂ [1, 44, 45, 61], and enhanced sintering of Cu particles in the presence of CO [81]. Rasmussen *et al.* [82] have used DFT (Density Functional Theory) to assess the stability and mobility of Cu-OH complexes on ZnO, but a clear mechanistic understanding, with a quantitative description of the effect of reactants on nanoparticle disintegration and single atom mobility, remains unavailable [68].

Clearly, it is necessary to observe OR in the relevant industrial reaction environment, demonstrating the importance of environmental electron microscopy. As discussed in section 3.5, HAADF STEM is required to provide resolution of particles with radii less than 1nm.

Therefore, ESTEM allows for the potential to image single atoms and small particles in reaction conditions to corroborate OR. Interestingly, single atoms are also of interest from a catalytic point of view; this is a new research topic referred to as single atom catalysis.

3.7. Single Atom Catalysis

The ability to both image and model sintering at the atomic scale provides the opportunity to investigate the increasingly important area of single atom catalysis. Efficient use of a catalyst involves maximising the surface area in order to provide increased access to catalytically active components. Recent theoretical and experimental work has shown that sub-nanometer catalysts can have improved activity/selectivity compared to nanometer sized particles [37]. However, it is currently unclear whether single atoms provide better performance than sub nanometer particles [34], with some studies instead suggesting that it may be possible to tune catalytic activity with particle size [83]. The reduced coordination number of single or small clusters of atoms often allows them to function as excellent active sites whilst retaining improved cost effectiveness, therefore explaining why minimising particle size has become a topic of such great interest. The main obstruction to this is the propensity for single atoms to sinter when exposed to typical industrial reaction conditions and methods of anchoring single atoms using supports have thus received much recent attention.

3.7.1. Support methods

Kyriakou *et al.* [84] took the approach of embedding single Pd atoms in a Cu support to maintain their dispersion, and found that the energy barrier of hydrogen uptake and subsequent desorption is lowered. A similar approach was also taken by Mao *et al.* [85], who used vacancy defects on Boron Nitride supports to stabilise Au atoms. Instead of utilising defects, Ranocchiari *et al.* [38] used pores in Metal Organic Frameworks (similar in structure to zeolites) to trap single atoms.

Binding to oxide supports has been shown to be a good method to anchor single atoms. Kwak *et al.* [86] found that coordinatively unsaturated Al³⁺ centres of γ -Al₂O₃ supports provide the binding site for Pt single atoms. Another similar method of stabilising single atoms is through the use of FeO_x supports, where the Pt atom locates exactly at an Fe vacancy [35, 37].

3.7.2. Applications

The Pt/FeO_x system is thought to be 2-3 times more active (based on the TOF) than a Au/FeO_x system for CO oxidation. The source of this activity is the highly vacant d-orbitals of the Pt single atoms, which also contribute to the support binding [37]. This work was further developed by comparison with an Ir/FeO_x single atom catalyst. The adsorption energy of CO on the Ir single atoms was found to be higher than on the Pt single atoms. Strong CO adsorption inhibits the activation of O₂, and therefore the weaker adsorption strength of Pt to CO is more favourable than that of Ir [87]. Application of Pt single atoms to other oxidation reactions shows increased activity compared to nanoparticles [88, 89].

The above application of Pt single atoms deal with oxidation reactions, however there are several other areas of single atom research that are currently extremely active. Zhai *et al.* [90] investigated the active site in the Pt catalysed WGS (Water Gas Shift reaction). They found that it is not the nanoparticle, but single species of ionised Pt that function as the active sites for catalytic turnover.

Another application of the Pt/FeO_x system is in the hydrogenation of substituted nitroarenes [91]. The TOF (Turnover Frequency) was found to be 20 fold higher than the best alternative (Pt nanoparticles on TiO₂) due to the preferential adsorption of nitro groups. This was due to positively charged Pt centres and the absence of Pt–Pt metallic bonding.

Pt single atoms on TiO₂ and FeO_x have been shown to be excellent photocatalysts [92-94]. The active site for H₂ evolution was shown to be oxidised Pt species embedded in the TiO₂ support [92, 93].

Recently the activity of a Pt single atom sample was compared to a Pt nanoparticle sample (mean size approximately 2.1nm) for the removal of NO_x when controlling emissions in diesel engine exhausts [95]. The Pt nanoparticles were deposited using a colloidal method which, according to [96], means no species smaller than 1nm exist. The single atom Pt exhibited higher NO conversion and N₂ selectivity than the nanoparticulate Pt. This was due to stronger adsorption of NO on the single atom Pt and facile dissociation to N and O atoms.

Single atom catalysis, especially Pt stabilised on FeO_x, is clearly currently a topic of great interest. It may be that the adatom species have always existed in industrial catalysts [35], but are only now detectable due to the improvement in HAADF STEM image resolution from spherical aberration correction [2]. The activity and selectivity of single atoms has been shown

in several applications [35, 37, 88-95] to be improved relative to a range of different nanoparticle sizes. Some understanding has also been gained to explain the improvement in terms of absorption/desorption energies of the reactant molecules. The electronic structure of single atoms is vastly different to metallic nanoparticles. Electron donation between single atom centres and supports modifies the band structure so that the metallic species binding site must be known for any understanding of electronic structure to be obtained [35]. This has mostly been understood via DFT or MD (Molecular Dynamics) calculations combined with some spectroscopy experiments [35, 37, 88-95]. The identification method commonly used for distinguishing single atoms is HAADF STEM, but the problem is that as discussed by [29, 33, 97] the nature of the active site often changes between ex situ identification and in situ activity measurements.

This is perhaps best illustrated by the recent MD study by Wang *et al.* [98]. They suggest that Au single atoms emerge from nanoparticles when binding to CO, then once oxidation has occurred, reintegrate with the nanoparticle. This touches on a very important aspect of heterogeneous catalysts, namely that the active site may only be present under reaction conditions and therefore difficult to identify in ex situ studies.

The capability at the York JEOL Nanocentre to study single atoms in gas environments at high temperature is thus vitally important for application in both single atom catalysis and studies of Ostwald Ripening. It allows for accurate particle size determination and single atom detection in reaction conditions [32, 33, 36, 40].

The present study seeks to understand Ostwald Ripening in a model methanol synthesis (Cu on various supports) catalysts using ESTEM. Typically, Cu catalysts are produced by reducing a CuO precursor. This will be the focus of the next chapter, which is followed by a study of Cu OR.

4. Activation of a Cu catalyst via Reduction

4.1. Introduction

Methanol is one of the most important basic components in the chemical industry with worldwide production of approximately 40 million tons in 2010 [99]. Furthermore, it has potential as an in situ source of hydrogen for fuel cells [79, 100] due to its ease of storage and transportation, combined with a 5-7 times higher energy density compared to compressed H₂ [101]. Cu is one component used to catalyse methanol synthesis and consequently, understanding of the activation and deactivation mechanisms of Cu is necessary to improve both catalyst activity and lifetime. Due to the scale of methanol production, small improvements in catalytic technology can lead to large economic impacts and make green technologies, such as fuel cells, more financially viable whilst also providing improved function. The activation process (in this case reduction) required to transform the precursor, CuO, into catalytically active Cu is very significant in determining the final size, structure and distribution of catalytic nanoparticles [79].

The importance of observing catalysts, and more specifically Cu, under reaction conditions (reactant gas and elevated temperature) has been demonstrated in [102-107]. Observation of chemical processes in situ, not only reduces contamination and spurious results, but allows for understanding of how the shape, size and structure of specific nanoparticles change [108] under reducing conditions, which may be altered when compared to ex situ studies [104]. Many in situ reductions of CuO have been investigated using XRD (X-ray Diffraction) and concentrate on determining if there are intermediate phases (Cu₂O) produced during the reaction, showing a strong dependence on reaction conditions (i.e. low pressures produce an intermediate) [102, 104, 109, 110]. Of the ETEM studies that have been performed on CuO, several have recently concentrated on crystal plane/activity relationships with associated DFT calculations, showing that certain crystal planes are more facile to be reduced than others

[111-113]. Other ETEM studies have shown the gas-Cu shape dependence [79], as well as the formation of a Cu_2O intermediate [103].

The fundamental aim of this chapter is to understand CuO reduction mechanisms and how they are a result of atomic scale interactions between the defects, catalyst support and environment (pressure, temperature). This knowledge can then be used to tune parameters of catalysts (in this case Cu) to produce more active, selective, durable and economical catalysts, which may enhance the commercial viability of alternative energy sources such as fuel cells.

4.2. Specimen Preparation

Copper nanoparticles were produced by deposition of a thin Cu film onto a Carbon support using a JEOL JFC2300HR sputter coater. This procedure provides several advantages over the alternative nano-particulate method such as minimisation of contamination and fine control of particle size. A 0.7nm film of Cu was deposited on to a C substrate which provided crystal sizes that were easily observable in TEM, produce a strong diffraction pattern and are also comparable in size (approximately 10nm diameter) to an industrial Cu catalyst [114-116]. Analysis of an industrial Cu/ZnO/Al₂O₃ catalyst (5-20nm crystal diameters at 2σ) further confirmed this.

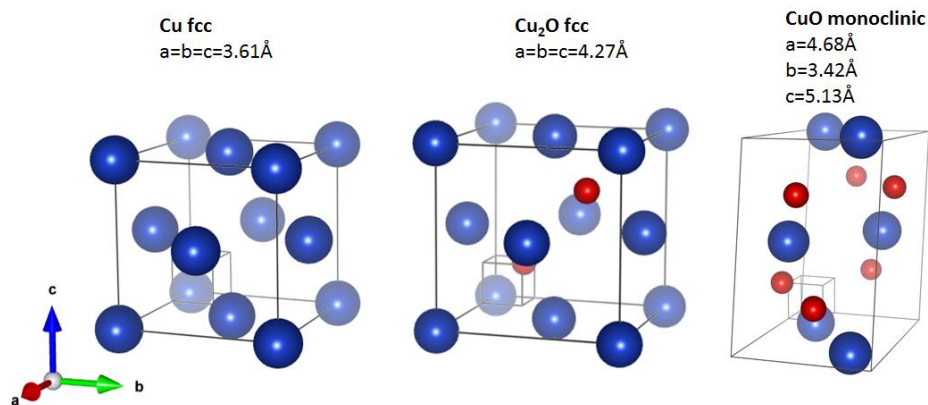


Figure 4.1: Ball and stick models of Cu (face centred cubic), Cu_2O (fcc) and CuO (monoclinic, with lattice constants a, b, c. Cu atoms are blue, O atoms are red.

The Cu thin films on TEM grids were annealed and oxidised with a baking unit in 5.5 mbar air at 350°C for 1 hour, which produces the CuO form of Copper Oxide (Figure 4.2). Initially, ceramic heating holders were used in this work due to the unavailability of MEMS heating holders. Once this equipment became available, in situ production of CuO was achieved using a MEMS chip holder (discussed in section 2.3) to oxidise the Cu film by heating at 250°C in 3Pa of O₂,

then spiking the temperature for 5s to 500°C. The MEMS chip Carbon films are continuous and therefore have a greater surface tension and fragility than standard holey Carbon film Copper TEM grids. Thus, when utilising MEMS chips, an in situ technique is preferable compared to use of the baking unit. This is because an understanding of the effect of oxidation on the C-film can be easily obtained. Identification of the Copper Oxide form is undertaken by analysis of selected area diffraction patterns (Figure 4.2) along with some characterisation of the exposed crystal planes via FFT (Fast Fourier Transform) of crystals orientated on the zone axis [117]. The crystal structure and lattice constants of Cu, Cu₂O and CuO can be seen in Figure 4.1.

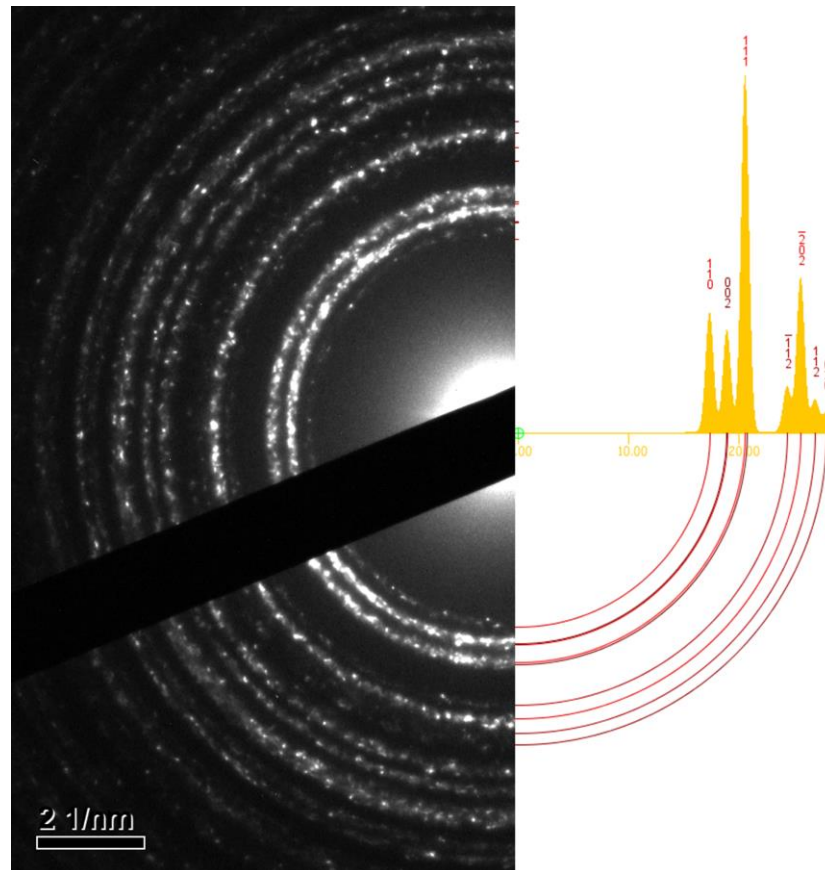


Figure 4.2: Selected Area Diffraction Pattern of CuO nanoparticles produced using a controlled pressure oven at 5.5mbar, 350°C for 1 hour.

4.3. ETEM Reduction of CuO

4.3.1. Experimental Conditions

To reduce the CuO precursor into the catalytically active Cu, nanoparticles were heated in situ under 3Pa of H₂ at 250°C. This allowed partial reduction and observation of the interface between Copper and Copper Oxide, thus permitting elucidation of the oxide reduction

mechanism. Previous work [102, 104, 109, 110, 118] indicates that reduction of CuO initiates at around 150-300°C for approximately 10nm diameter nanoparticles. However, the mixture (H₂, CO concentrations) of the reducing atmosphere along with both the method of pressure measurement (e.g. flow rate entering a reaction cell, pressure at entrance/exit) and the pressures reported vary immensely. This makes comparison of gas pressure between CuO reduction experiments extremely difficult, however some reviews have been undertaken by Thalinger [110] and Pike [109]. A summary of different techniques and experimental conditions explored for determining CuO reduction mechanism is shown in Table 4.1. This is intended as an illustration of the range of experimental approaches undertaken rather than a comprehensive survey.

Author	Technique	Particle Diameter	Gas	Temperature	Substrate
Rodriguez <i>et al.</i> [102]	XRD	Powder	H ₂ 20cm ³ /min	150-300°C	None
Pike <i>et al.</i> [109]	XRD	5-12nm	CO+ H ₂	200-600 °C	None
Kim <i>et al.</i> [104]	XRD	Powder	H ₂ 5-15cm ³ /min	150-300°C	None
Ciston <i>et al.</i> [103]	ETEM	4.6nm	H ₂ 1.5 Torr	0-400 °C	CeO ₂ MMO
Yanase <i>et al.</i> [118]	Optical Transmission	4-10nm	CO/H ₂ 200cm ³ /min	150-300°C	None
Thalinger <i>et al.</i> [110]	TEM (ex situ) +EELS	12nm	H ₂ 1 mL/s	0-600 °C	SiO ₂
Lee <i>et al.</i> [119]	XPS	Bulk	Vacuum	>400 °C	None
Zhou <i>et al.</i> [120]	TEM+Raman	Nanorods+particles	H ₂ 20mL/min	0-500 °C	CeO ₂ MMO
Bao <i>et al.</i> [113]	Gas Analyser+ TEM (ex situ)	?	H ₂ 20mL/min, CO 40mL/min	5 °C /min	?
Liu <i>et al.</i> [121]	STEM+various spectroscopy	?	H ₂	2 °C /min	CeO ₂ MMO
Garcia <i>et al.</i> [122]	XANES TEM (ex situ)	?	H ₂	500 °C	Al ₂ O ₃ (CuO impregnated)
Wang <i>et al.</i> [105]	XRD+XANES	Powder	CO 1-5mL/min	25-725 °C	None

Table 4.1: Experimental techniques and conditions used to study CuO reduction. Note that MMO indicates a mixed metal oxide, EELS (Electron Energy Loss Spectroscopy), XANES (X-ray Absorption Near Edge Structure)

Pressure has been shown to effect the formation of intermediate phases such as Cu_2O and Cu_4O_3 . Under limited CO or H_2 atmospheres at $200\text{--}300^\circ\text{C}$, Cu_xO_x phases have been reported using in situ XRD [102, 104, 105, 118], XPS (X-ray Photoelectron Spectroscopy) [119], ex situ TEM [110, 113, 123, 124], or a combination of these. The only ETEM studies of CuO are by Hulse *et al.* [125], Creemer *et al.* [23], and Ciston *et al.* [103] where industrial systems such as Cu/ZnO and Cu/CeO_2 are studied. Both Hulse *et al.* [125] and Ciston *et al.* [103] report Cu_2O intermediate phases, but are primarily interested in the synergistic effects of Cu on either ZnO or CeO_2 respectively. Due to the complex and interactive nature of both environmental and structural parameters, a model system Cu/C system is used in these experiments. The effect of pressure in this case is discussed below.

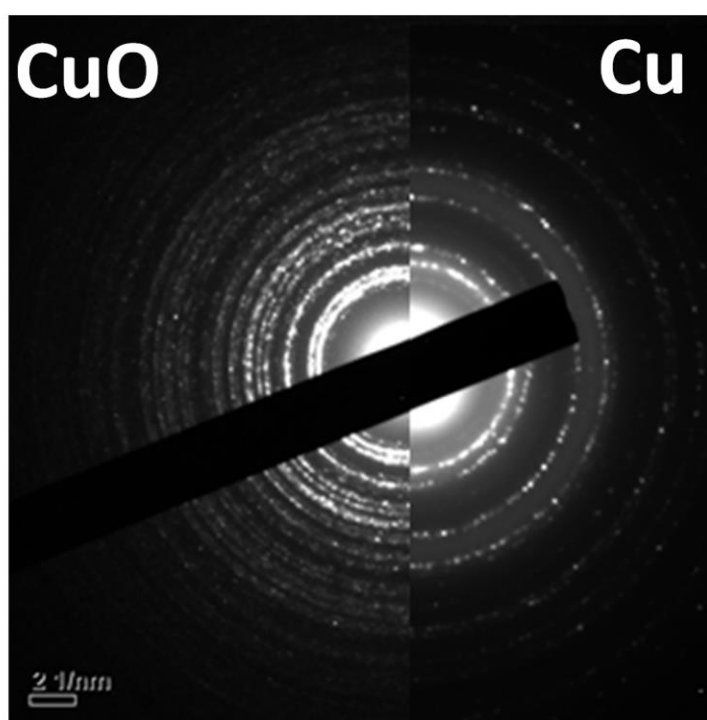


Figure 4.3: In situ reduction of CuO , completed by 350°C , temperature ramp of 50°C per 30 mins in 3Pa H_2 . Diffraction rings indicative of Cu are observable at temperatures of 250°C . Left hand CuO diffraction pattern was observed pre-reduction, right hand Cu was observed after heating in H_2 at 350°C .

4.3.2. Effect of H_2 Pressure on CuO Reduction

Previous CuO reduction studies [104, 105, 109, 110, 123, 124] have clearly shown that limited H_2 or CO flow result in intermediate phases forming. Rodriguez *et al.* [102] performed the first in situ XRD of CuO reduction, finding that a direct CuO to Cu transformation occurs at

atmospheric pressures of H_2 . However, at lower pressures (10^{-4} Torr) a Cu_2O intermediate was formed.

Using 1Pa of H_2 (in contrast to other experiments performed here at 3Pa), led to the formation of Cu_2O . The Cu_2O phase was repeatedly observed for lower H_2 pressures. Smaller (below 5nm) diameter nanoparticles appear to have reduced to Cu_2O , Figure 4.4 (a), however larger nanoparticles often contain Cu or CuO phases. SADPs (Selected Area Diffraction Patterns) clearly show that the primary phase observed is Cu_2O , Figure 4.4 (b).

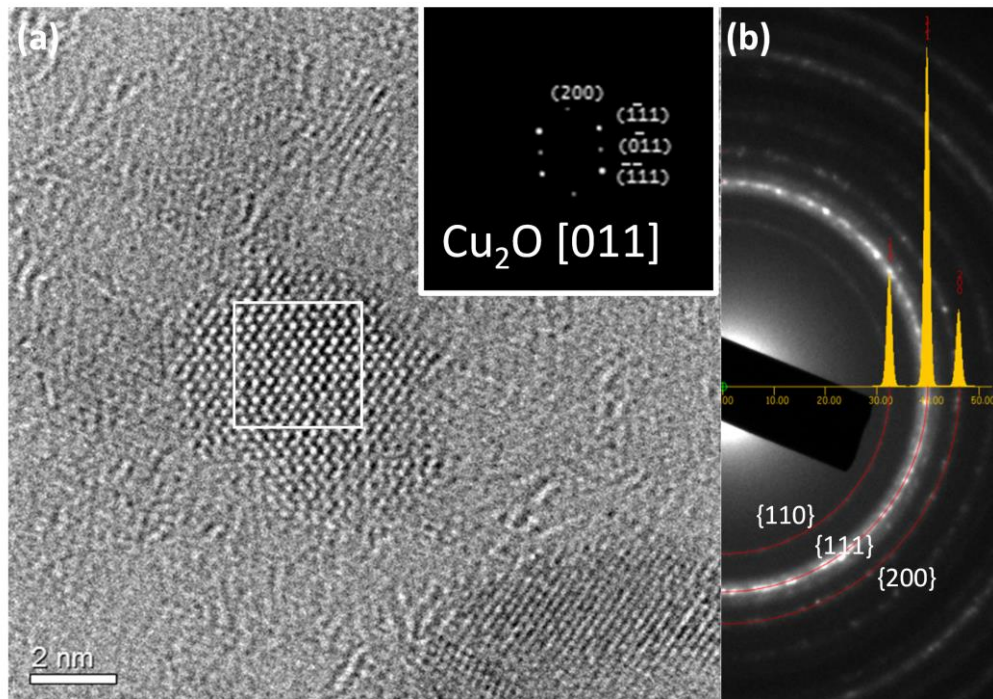


Figure 4.4: (a) HRTEM of Cu_2O nanoparticle in 1Pa H_2 , 250°C after 1 hour. FFT shows [011] orientation. (b) SADP at camera length of 40cm showing majority of sample is Cu_2O with (110), (111) and (200) rings labelled.

This result suggests that the pressure regime being operated in (1-3Pa H_2) is sufficient to achieve the same chemical reactions that are reported elsewhere at pressures of 1.5Torr H_2 [103]. As discussed in section 2.3, the criterion for surface reactions likely has more to do with monolayers of gas per second, rather than requiring industrial reactor conditions-which in some cases can extend up to 100bar [40, 117]

4.3.3. Reduction Mechanisms of CuO

There are many previous pieces of work on reduction mechanisms and the interaction of defects [12, 41, 102, 104]. In order for complete reduction, bulk oxygen atoms must either migrate out to the surface of the crystal or H atoms migrate inwards. Either of these mechanisms requires the formation of extended defects, perhaps explaining the prevalence of defects in the Cu particles observed (Figure 4.5).

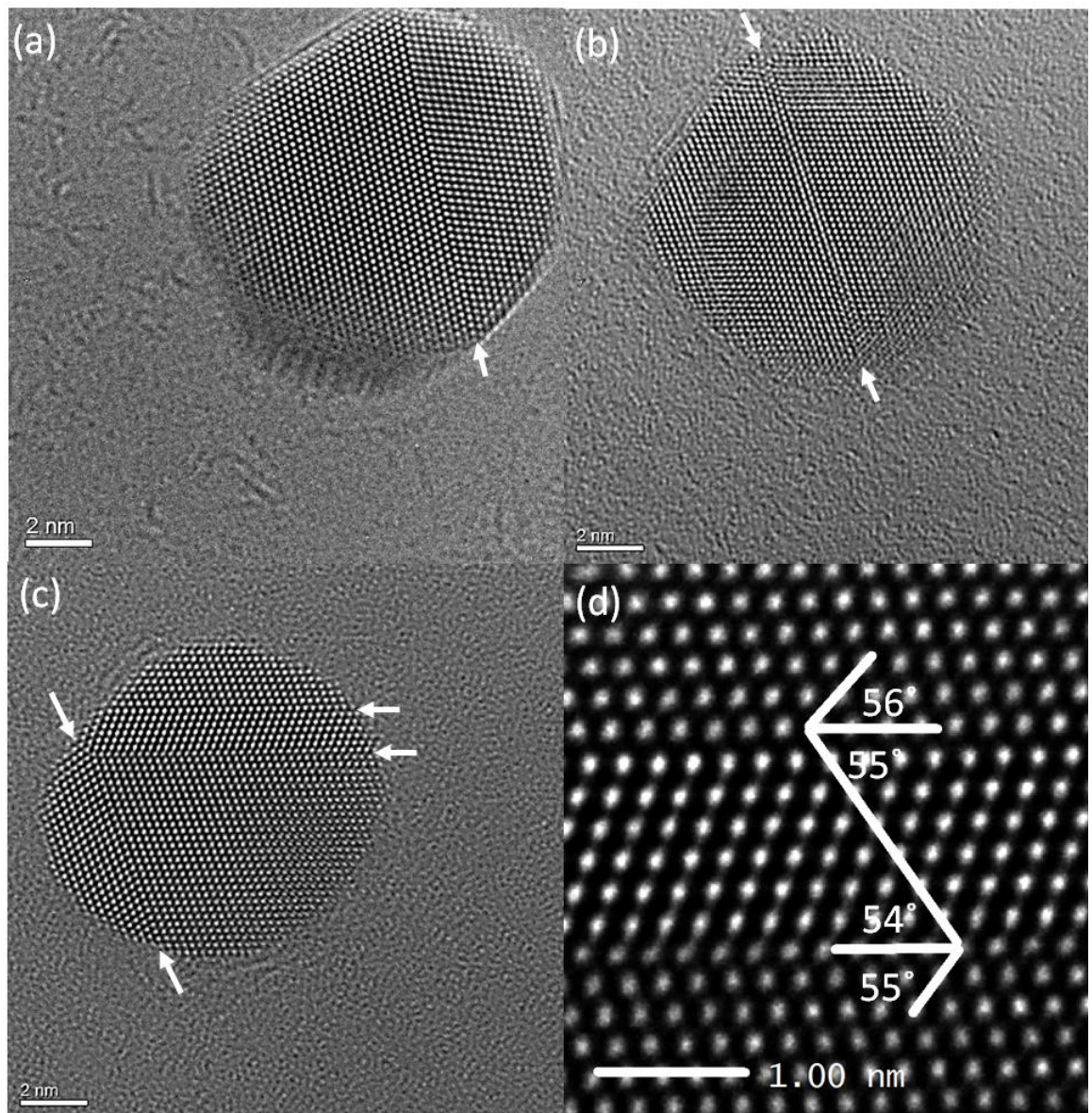


Figure 4.5: Typical Cu nanoparticles post reduction in 3Pa of H₂ at 250°C. Particles are in [011] orientation with (a) single twin boundary (b) probable dislocation, (c) single twin and lamellae twin boundary, (d) enlarged view with adjusted contrast of lamellae twin from (c), showing analysis of twin with angle of approximately 55°.

Previous work exploring CuO reduction mechanisms has been limited to ex situ HRTEM studies or ETEM industrial systems (as discussed in section 4.1). This is therefore believed to be the first ETEM study of CuO reduction mechanisms.

Observation of nanoparticles on a C-support at 250°C, 3Pa H₂ was undertaken at 5 minute intervals in order to minimise exposure to the electron beam. Beam effects in TEM are more fully discussed in section 4.4.1. In Figure 4.6, a partially reduced MTP (multiply twinned particle) is shown. The nanoparticle is composed mostly of Cu[101], excluding one twin boundary where CuO [-101] is present. The interface between the Cu and CuO is not oriented on the zone axis, however planes with 0.215nm spacing are observed, suggesting CuO (111) or Cu (111). This allows for prediction of the reduction mechanism where CuO[-101] reorients so that CuO(111) planes are visible(spacing 0.215nm), which are similar in spacing to Cu(111) (spacing 0.211nm). Reorientation to Cu[-101] then occurs, which can be seen at the edge of the particle, labelled (d) in Figure 4.7.

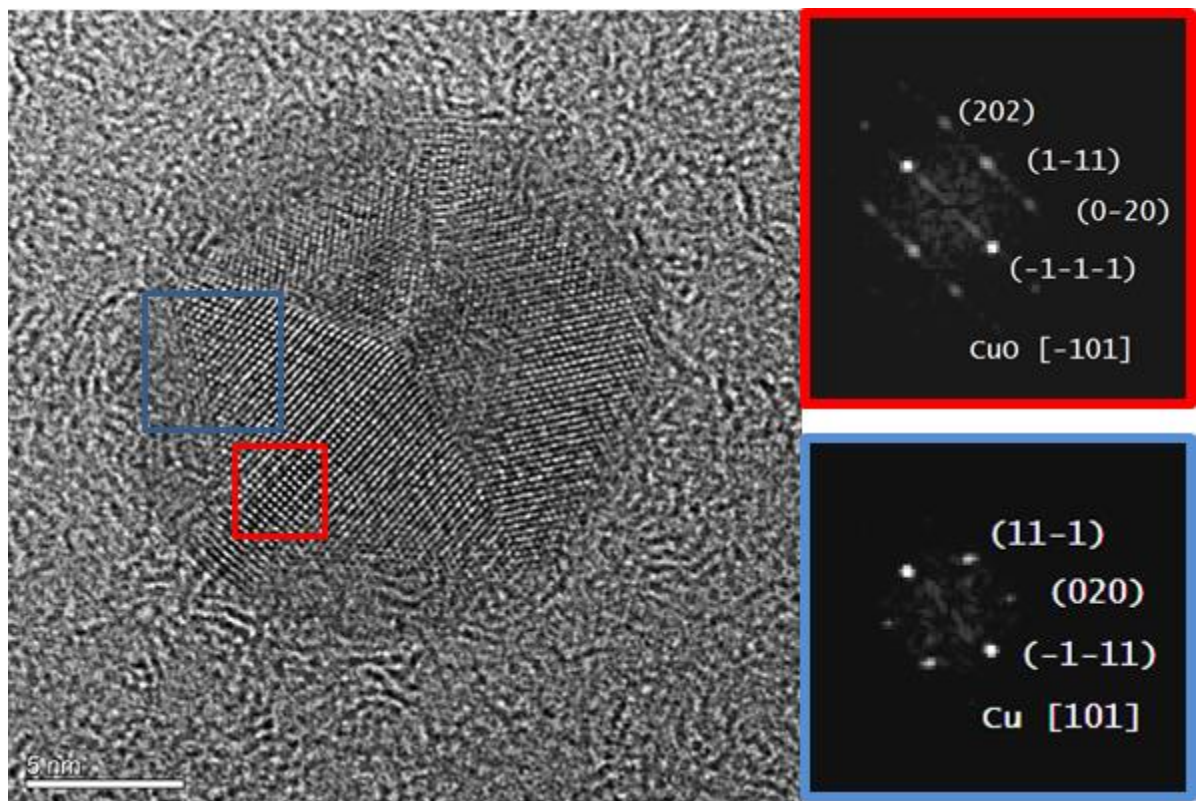


Figure 4.6: MTP nanoparticle showing Cu/CuO interface. The CuO [-101] FFT is clearly distinguished from similar Cu cubic regions by the presence of the CuO (202) plane with a spacing of $d=0.158\text{nm}$.

Interestingly, this process appears to leave CuO at the surface of the nanoparticle, with the reduction to Cu occurring internally. Progression of the reduction can be observed by

comparing the width of the CuO[-101] phase parallel to the nanoparticle surface in Figure 4.7 (i) at 30 mins, with that in (ii) at 40 mins. Here, a shift from 8 atoms wide to 5 atoms is measured. In the perpendicular direction, the depth of the CuO[-101] phase (i) is 15-16 atoms, compared to 10 in (ii).

Previous work has discussed two mechanisms by which metal oxides can be reduced. Firstly, O atoms can migrate out of the particle where they can react with dissociated hydrogen, leading to O vacancies [105, 126]. Secondly, the H atoms may diffuse into the bulk Cu of the particle until they reach the remaining oxygen (within the Copper Oxide), where they react to form a hydroxyl and diffuse out of the particle [12, 105]. The diffusion of H⁺ into the nanoparticle would logically suggest that reduction would proceed from the surface into the bulk [104]. The mechanism by which the OH diffuses through the outer layer of Cu is poorly understood, however similar studies have been performed on NiO [12, 127, 128], including one ETEM observation of the process [129]. The conclusions of these papers suggest that the overall reduction rate slows due to a build up of OH/H₂O molecules at the NiO/Ni interface.

As the reduction is clearly progressing inside the particle, rather than at the surface, it is suggested that O must be diffusing out of the nanoparticle. Maimaiti *et al.* [126] hypothesise that subsurface O diffuses to the surface and reoxidises the metal in competition with H reduction, leading to a surface oxide and subsurface O vacancies. Kim *et al.* [104] show using DFT calculations that the difference in stability between CuO with many O vacancies, Cu₄O₃ and Cu₂O is negligible, allowing for sequential reduction (as opposed to a direct reduction from CuO to Cu) to occur. Kim *et al.* [104] also state that a shrinkage in the a and c axes of the unit cell should occur when enough O vacancies are present to induce sequential reduction. This argument is supported by the change from CuO(1-11) 0.233nm spacing, to 0.215nm shown in Figure 4.7 (b). However, it is difficult to corroborate the sequential reduction proposed by Kim *et al.* [104], due to the off zone axis orientation of the inner part of the nanoparticle during this stage of reduction.

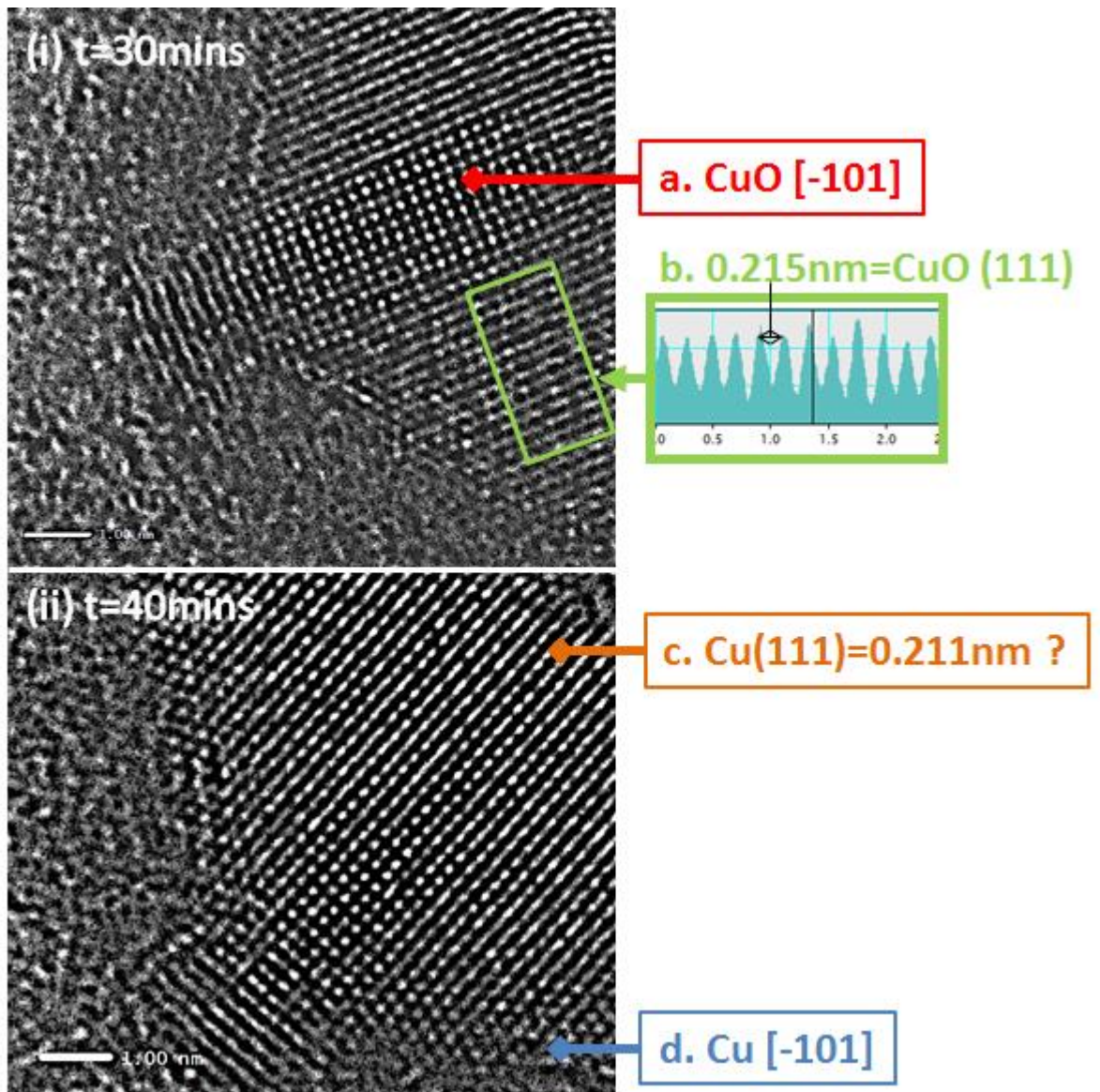


Figure 4.7: Reduction is proceeding within the nanoparticle from Figure 4.6, with a reduction in the width and depth of the $\text{CuO}[-101]$ penetration observed between (i) and (ii). The reduction mechanism is suggested to be (a) $\text{CuO}[-101]$ reorientating so that (b) $\text{CuO}(111)$ planes are visible ($d=0.215\text{nm}$), which are similar in spacing to (c) $\text{Cu}(111)$ ($d=0.211\text{nm}$). It is clearly difficult to distinguish between (b) and (c), however a clear reorientation to $\text{Cu}[-101]$ then occurred.

A second nanoparticle, observed under the same pressure and temperature conditions (3Pa H₂, 250°C) is shown in Figure 4.8. This nanoparticle appears to have multiple fivefold centres, as opposed to the one centre shown by the nanoparticle in Figure 4.6, but is similar in size and zone axis orientation. In contrast, the reduction appears to proceed from the surface of the nanoparticle. This implies the reduction proceeds via migration of H⁺ into the bulk structure and reduction ensues when interaction occurs with an O atom [104, 105]. This should result in expansion of the CuO lattice [104, 130]. The planes running either side of the fivefold axis have a spacing of 0.21nm far from the surface, which approaches 0.317nm at the point labelled with the orange arrow in Figure 4.8(i)-this may be a result of the expansion discussed, however precise measurements of the lattice constants are required.

The surface of the nanoparticle in Figure 4.8 is well defined with few kinks and steps. The nanoparticle in Figure 4.6 has what appears to be an amorphous layer coating the surface. It is suggested that this may be the surface formation of hydroxyl groups, after O has migrated out of the lattice. The amorphous layer is absent in the surface reduction of Figure 4.8 as H⁺ may migrate into the lattice and bond with an O, thus meaning the formation of hydroxyls occurs around the oxide/metal interface, as opposed to the nanoparticle surface.

Two reduction mechanisms have now been identified under broadly similar conditions. The distinguishing feature is the formation of Cu on the surface, or within the nanoparticle. Previous work [104, 126] has identified the controlling factor to be the density of H⁺ adsorption on the nanoparticle surface. This is corroborated by Rodriguez *et al.* [131], who identify sites for H₂ dissociation as the rate limiting factor. Many active sites lead to high H⁺ density, thus allowing for migration of the species into the nanostructure. It is known that the density of adsorbed H⁺ will vary with defects (as low coordination number surface atoms will be present)[116, 132], nanoparticle crystallinity [113]and pressure.

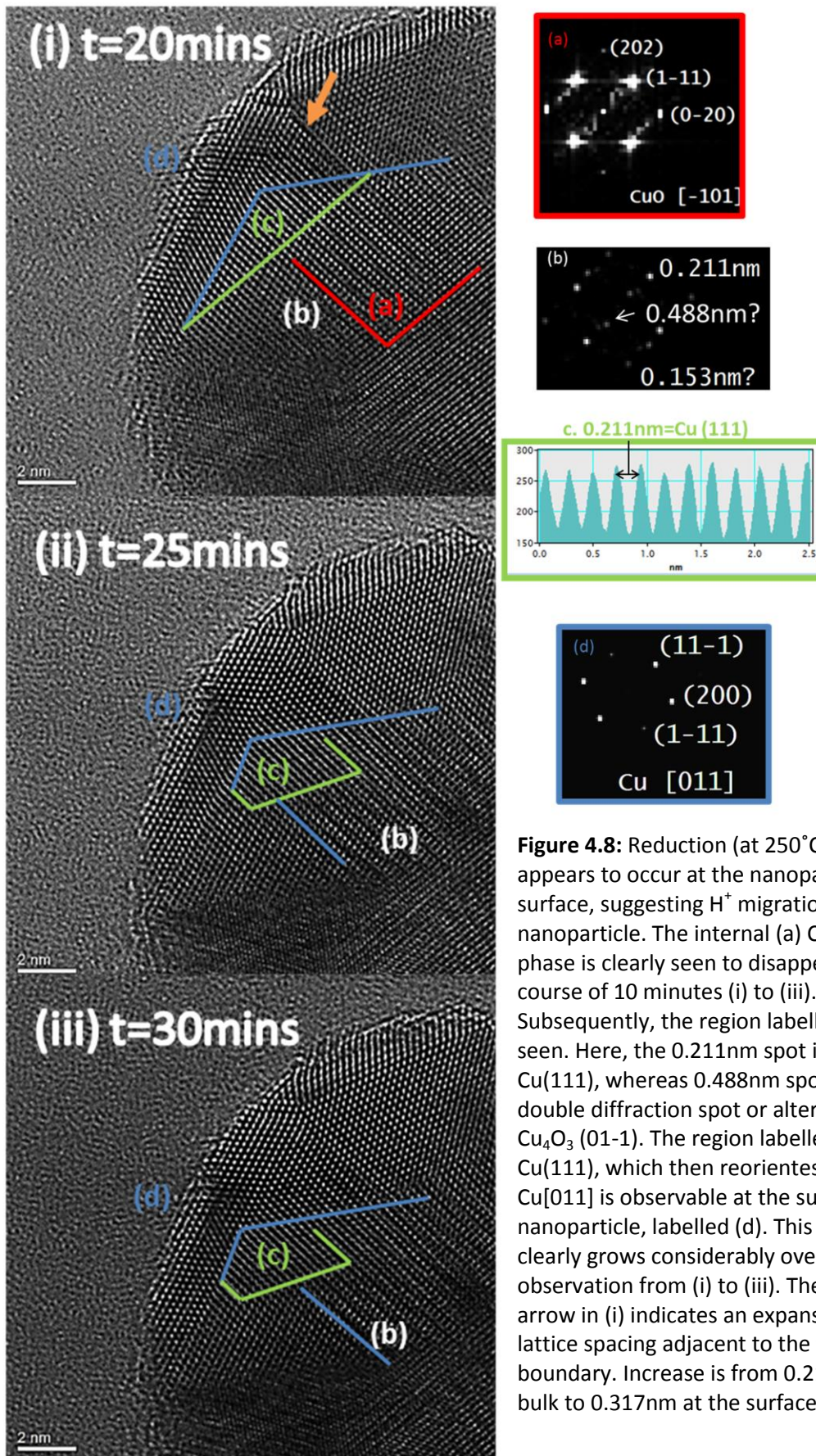


Figure 4.8: Reduction (at 250°C, 3Pa H₂) appears to occur at the nanoparticle surface, suggesting H⁺ migration into the nanoparticle. The internal (a) CuO[-101] phase is clearly seen to disappear over the course of 10 minutes (i) to (iii). Subsequently, the region labelled (b) is seen. Here, the 0.211nm spot is probably Cu(111), whereas 0.488nm spot may be a double diffraction spot or alternatively Cu₄O₃ (01-1). The region labelled (c) is Cu(111), which then reorients so that Cu[011] is observable at the surface of the nanoparticle, labelled (d). This region clearly grows considerably over observation from (i) to (iii). The orange arrow in (i) indicates an expansion in the lattice spacing adjacent to the twin boundary. Increase is from 0.21nm in the bulk to 0.317nm at the surface.

The pressure has been kept constant in both experiments and, as discussed in section 4.3.2, any significant decrease in pressure is likely to induce sequential reduction of small (less than 5nm diameter) nanoparticles. Cu_2O phases are not seen in the smaller nanoparticles observed at 3Pa thus, at least qualitatively, it can be assumed that gas supply fluctuations are not causing the variation in H species.

Low coordination sites at twins have been previously studied in Cu/Zn methanol catalysts by Behrens *et al.* [116] and Kasatskin *et al.* [132]. Here it was suggested that in Cu nanoparticles most bulk defects terminate at the surface, which enables the energetic stability of kinks and steps and thus provides low coordination sites for adsorption. These defects remain pinned by interfacial strain and the associated increase in activity is explained by the stronger binding of species, such as H^+ . The nanoparticles observed in Figure 4.6 and Figure 4.8 both contain twins and it therefore seems improbable that any difference in H^+ surface density is due to defect structure. However, both reductions occur around the twin boundary and as discussed by Behrens *et al.* [116], this may stabilise kinks and other low coordination features, allowing the nucleation of H^+ . The region of reduction is perhaps initiated by the twin boundary, even if this does not also explain the reason for dissimilar reduction mechanisms.

Figure 4.9 shows the exposed Cu surface plane is different between the two nanoparticles, thus suggesting a difference in initial CuO plane orientation. As investigated by Bao *et al.* [113], $\text{Cu}_2\text{O}(111)$ reduces faster than $\text{Cu}_2\text{O}(100)$ due to the presence of a coordination unsaturated Cu. $\text{Cu}_2\text{O}(111)$ therefore exhibits a higher H and CO adsorption, providing evidence of oxide shape dependent surface activity [112]. The exposed CuO crystal face clearly has an effect on the H^+ adsorption. However it cannot be ruled out that pressure variations or defect structure are having an additional impact on H species density. Further work using DFT studies of H-Cu bonding and atomic scale EELS to determine Cu oxidation states is required to fully explain the reduction mechanisms discussed here.

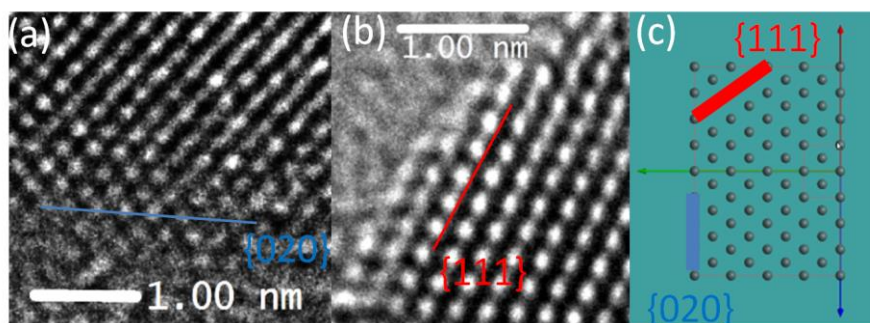


Figure 4.9: (a) Nanoparticle edge from Figure 4.6, with Cu(020) exposed, shown by $d=0.186\text{nm}$ (b) Nanoparticle edge from Figure 4.8, with Cu (111) exposed, shown by $d=0.211\text{nm}$ (c) calculated atomic arrangement of Cu[011] with (111) and (020) labelled.

4.4. Characterisation of Cu Nanoparticles Post Reduction

Subsequent to reduction, most nanoparticles appear with single or multiple twin boundaries. Larger nanoparticles (radii greater than 8nm) tend to have fivefold centres as seen in Figure 4.6. After activation, sintering of the Cu nanoparticles occurs. As discussed by Simonsen *et.al* [44, 61] this process can often take several hours, with observation of the same group of nanoparticles required. Clearly, beam induced effects could be a significant contributor to sintering. In section 5.2 the approach required to ensure that temperature effects dominate beam induced changes is investigated. To ensure that changes are observed, an imaging frequency of 1 acquisition every 5 minutes (hereafter referred to as 1/5 minutes) is applied. Using this imaging frequency at 400-550°C in 3Pa of H₂ the operating temperature is shown to dominate beam charging or heating effects, thus in the following experiments these conditions are similarly applied.

4.4.1. Electron Beam Effects

In the reduction study of section 4.3, beam effects were minimised by decreasing the acquisition time and imaging only once every 10-15 minutes. This approach was taken because the complex nature of reduction processes means that quantification of beam effects is extremely difficult. However, post-reduction analysis of beam effects is considerably simpler due to the accessibility of measurands such as particle size change. This approach is implemented successfully in [23, 44]. In chapters 5 and 6 a low magnification HAADF STEM image of the area exposed to the electron beam is used to determine at which temperatures beam induced effects dominate temperature driven ones. Observations of Cu indicate that temperatures below 400°C lead to electron beam inhibition of Ostwald Ripening. There are two main reasons why this approach will not work with the samples studied here using TEM. Firstly, the beam illumination area is significantly larger in TEM and less consistent, thus precise definition of the exposed area is more complex. In STEM the interaction area is clearly defined, due to the sharply defined scan area illuminated. Secondly, the particle density of these samples is such that the magnification required for atomic resolution images (greater than 600kX) provides a field of view with less than 5 particles. Often, high magnification (1 or 1.2MX) images of individual nanoparticles are required. Achieving these requires different

beam exposure times due to the need to adjust instrument operation conditions, thus the assumption that all nanoparticles observed receive the same electron dose is incorrect.

To mitigate for beam effects in post reduction studies, the continuous exposure condition is contrasted with the minimised exposure condition of 1/5minutes. Two similarly sized ($r=4.5$ and 4.7nm respectively) nanoparticles are observed in Figure 4.10 and Figure 4.11 over 10 minutes with continuous beam exposure and 1 hour with 1/5minute imaging. An individual image takes between 45s and 60s to acquire, thus the low exposure total dose is equivalent to 9-12 minutes of continuous exposure. The defect structure is slightly different between the two with the high beam exposure nanoparticle containing only a single twin boundary, whilst in the case of low beam exposure a lamellae twin and single twin boundary is observed. For the purposes of this discussion, the nanoparticles are treated as broadly identical.

In the low exposure regime of Figure 4.10, changes in the nanoparticle orientation are clearly occurring. In (a), Cu[011] is clearly exposed, whilst by (f) these regions (excluding the lamellae twin) tend to have moved to Cu(111). This makes it difficult to identify the twin boundary on the left hand side of the particle, however the shape of the nanoparticle indicates that it is probably still present. There does appear to be some loss of mass at the bottom right of the particle, but the nanoparticle is broadly intact after an hour at 500°C , in 3Pa H_2 .

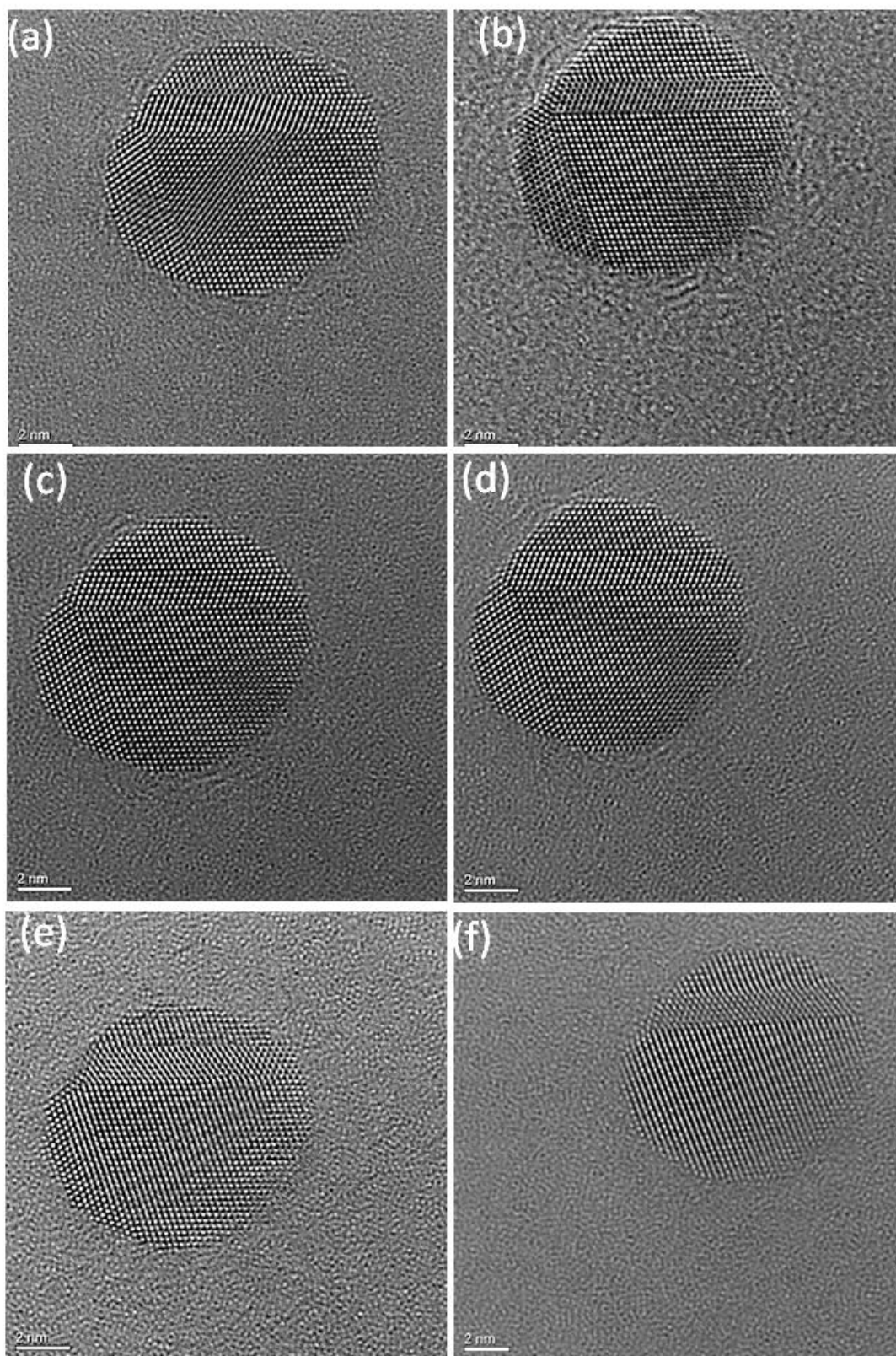


Figure 4.10: Nanoparticle with single twin boundary and lamellae twin observed at a rate of 1/5 minutes. (a) 0 mins, (b) 10 mins (c) 20 mins (d) 30 mins (e) 40 mins (f) 50 mins. Low beam exposure shows that there is little effect on nanoparticle size due to environment or beam induced Ostwald Ripening. There is also no discernible damage to the C-film.

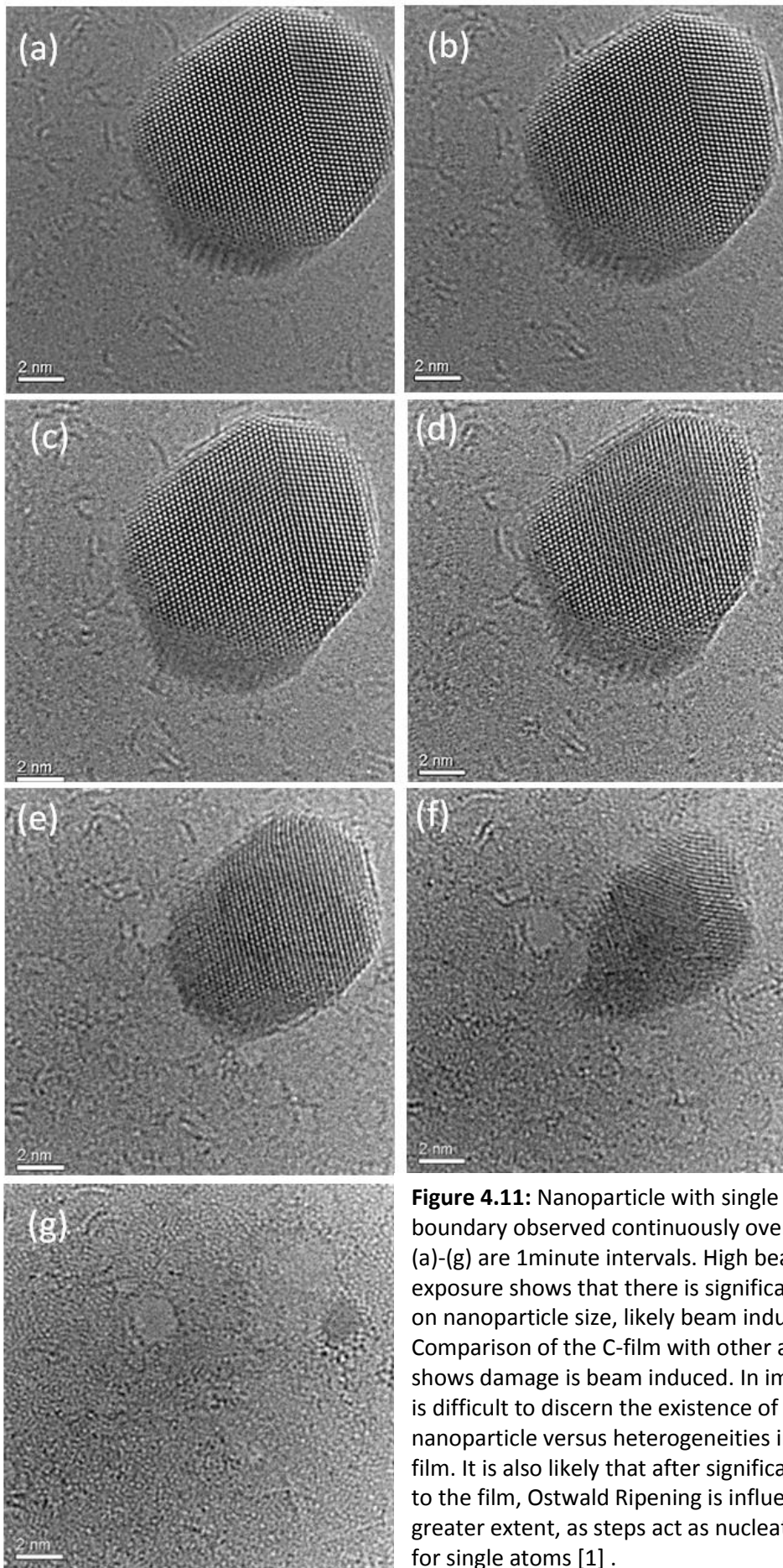


Figure 4.11: Nanoparticle with single twin boundary observed continuously over 10 mins, (a)-(g) are 1minute intervals. High beam exposure shows that there is significant effect on nanoparticle size, likely beam induced. Comparison of the C-film with other areas shows damage is beam induced. In image (g), it is difficult to discern the existence of the nanoparticle versus heterogeneities in the C-film. It is also likely that after significant damage to the film, Ostwald Ripening is influenced to a greater extent, as steps act as nucleation sites for single atoms [1] .

In contrast, the nanoparticle observed in Figure 4.11 decays to a size below the detection limit [103] over the course of 10 minutes. The detection limit for small particles in TEM was previously discussed in sections 3.3.2 and 3.5. Interestingly, the nanoparticle retains the twin boundary until (f) with most mass loss occurring at the nanoparticle edges either side of the defect. Examination of the boundary suggests that there is no obvious reduction in the coordination number of Cu atoms at this point. This provides some evidence of size, as opposed to defect, driven Ostwald Ripening.

The previous observations indicate beam enhanced Ostwald Ripening of Cu nanoparticles. Compared to reaction rate studies (such as the reduction mechanism), Ostwald Ripening utilises particle size as a direct measurand which allows a simpler deconvolution of beam effects from parameters such as pressure, temperature and defect structure. An OR based beam effects study requires the particle to be detectable throughout the experiment and enough data to average out unusual nanoparticle features (e.g. support roughness). This translates to a requirement of high magnification imaging for optimised detectability and a low magnification study to provide the number of nanoparticles necessary for statistical significance. This introduces several problems. Firstly, as seen in Figure 4.11 (g), it is difficult to differentiate particles and support degradation with phase contrast imaging [1, 103]. Secondly, to achieve this level of detectability, high magnification is required (1-1.2MX) of individual nanoparticles. Ideally, low magnification images of many nanoparticles would be used to reduce the variation in beam dose between nanoparticles. This is clearly one advantage of ESTEM. As discussed in section 2.4 the Z-dependence can provide resolution of nanoparticles down to a single atom in gas environments. This enables: low beam dose experiments; homogenous exposure over the sample area; a simple measurand of particle size; and detectability down to the single atom level. The application of ESTEM to calculate beam effects via OR will be further discussed in section 5.2.

4.5. Conclusions

ESTEM was applied to investigate the CuO reduction pathway and ascertain the influence of structural and environmental parameters on the mechanism. Under reduced H₂ pressure (1Pa compared to 3Pa nominal) a Cu₂O intermediate was identified, in agreement with several other CuO reduction studies [102, 103, 105, 109, 110, 118, 119, 122, 133]. The pressure dependent presence and absence of intermediates in the reduction process suggests that

despite the low (relative to a chemical reactor) pressure, the gas supply at the sample surface is sufficient to simulate, in this respect, much higher pressure conditions [40, 117].

A reduction mechanism is proposed of CuO[-101] to Cu[-101], potentially reorientating through CuO(111) and/or Cu(111). However, the location of the reduction interface clearly varies when examining what appear to be similar nanoparticles. It is suggested that formation of Cu within the nanoparticle derives from H⁺ deficiency at the nanoparticle surface, resulting in O migration. With high H⁺ surface density, hydroxyl formation inside the nanoparticle is assumed. Here, formation of Cu is observed to progress from the nanoparticle edge. The variation in surface H⁺ may be a result of different exposed Cu planes, pressure fluctuations or defect structure. Further work utilising atomic scale EELS and DFT is required to investigate this.

Analysis of studies on beam induced post reduction Ostwald Ripening suggest that ESTEM is required to provide: improved particle detectability [33]; better control of individual nanoparticle electron dosages; and well defined beam exposed areas. This problem will be further explored in the following chapters 5 and 6.

A model system has been studied to understand the process by which Cu is activated when utilised industrially in methanol synthesis. After reduction, deactivation mechanisms cause the Cu catalysts activity to reduce with time. This will be explored in the subsequent chapter.

5. Ostwald Ripening of a Model Cu Catalyst

5.1. Introduction

The most common catalysts for methanol production are copper based [134]. These typically consist of Cu/ZnO or Cu/ZnO/Al₂O₃ systems in mixtures of H₂, CO and CO₂. Currently the two main areas of technical concern centre around the nature of the metal-support synergy in Cu/ZnO [79, 116, 132, 135], and the stability of Cu based catalysts under reaction conditions [115, 136]. The deactivation of the system due to sintering causes approximately 1/3 of the initial catalyst activity to be lost within the first 1000 hours of operation [137].

There is currently no reliable way of predicting the sintering of either industrial or model catalytic systems [138]. The lack of reliable methods of predicting sintering behaviour means that newly developed catalysts must be tested in real time for the entire required lifetime (greater than 1 year). Thus accurate models, combined with in situ observations, can provide valuable information for developing catalysts for use in methanol synthesis and other reactions.

The sintering of metal nanoparticles on a support is thought to occur via two different mechanisms: (a) Particle Migration and coalescence (PMC) and (b) Ostwald Ripening (OR), where single atoms/small clusters migrate from smaller to larger particles. The atomic migration mechanism was originally suggested by Ostwald [139] whilst studying the growth of particles in solution. This was then extended by Lifshitz, Slyozov [49] and Wagner [140] (LSW) who considered Ostwald ripening of 3D clusters in a 3D environment for both diffusion and interface limited regimes. Further work by Chakraverty [141] and Wynblatt and Gjostein (WG) [43] extended this to 2 or 3D clusters on a 2D support.

Ostwald Ripening is driven by the reduction of surface energy (γ) which can be explained by examining the Gibbs-Thomson relation (GT). The concentration of single atoms is greater close

to smaller particles. This means there is a concentration gradient, so a net flux of atoms will diffuse from smaller to larger particles.

$$\rho_r = \rho_\infty e^{\left(\frac{2\gamma\Omega}{kTr}\right)} \quad 5.1$$

Here, Ω is atomic volume, T is temperature, k is Boltzmann's constant, ρ_∞ is the concentration of adatoms on the substrate in equilibrium with an infinitely sized particle and ρ_r is the concentration of adatoms on the substrate adjacent to a particle.

The WG Ostwald Ripening model can be thought of as operating in two regimes: interface and diffusion controlled [43]. In the interface controlled regime, the diffusion across the support surface is assumed to be much faster than the rate of detachment of single atoms. The diffusion controlled regime assumes the activation energy for single atom migration is large and thus diffusion is slow compared to single atom detachment. Both of these regimes include the mean field assumption: that the concentration of single atoms on the support is constant beyond the screening distance, L , from the edge of the particle. The original work by WG [43] also uses only the first two terms of the Taylor expansion applied to the exponential term in the GT equation 5.1. Campbell *et al.* [67] showed that this assumption is incorrect for particles where r is less than 5nm and thus, to accurately model systems in this size region, the GT relation must not be simplified during the derivation of equation 5.2. Equation 5.2 applies to the interface limited regime, where ν is substrate site vibrational frequency, a is the interatomic spacing, r_c is average particle radius, θ is the particle/support contact angle and E_{Tot} is the heat of sublimation of the metal minus the energy of adsorption of a metal adatom on the substrate plus the activation energy for diffusion of the adatom on the substrate surface [138].

$$\frac{dr}{dt} = \frac{K\Omega}{r} e^{\left(\frac{-E_{\text{Tot}}}{kT}\right)} \left[e^{\left(\frac{2\gamma\Omega}{kTr_c}\right)} - e^{\left(\frac{2\gamma\Omega}{kTr}\right)} \right] \quad 5.2$$

$$K = \frac{(2 \sin \theta)\nu}{(2 - 3 \cos \theta - \cos^3 \theta)a} \quad 5.3$$

$$E_{Tot} = \Delta H - E_{Ads} + H_s \quad 5.4$$

A power law expression can be used to estimate which Ostwald Ripening regime the system is operated within [43].

$$\langle r \rangle \propto t^n \quad 5.5$$

The value of n is $1/3$ for interface controlled and $1/4$ for diffusion controlled regimes. As discussed above, equation 5.5 requires the assumption that a first order Taylor expansion can be applied to the exponential term in Gibbs-Thomson relationship (equation 5.2). The power law expression has therefore proven invalid for small particles (sub 5-6nm) [63, 138, 142] but has still been utilised successfully by many authors [65, 143-145] to determine whether interface or diffusion controlled ripening occurs.

As stated by Challa *et al.* [76] the diffusion barrier of metal adatoms on substrates is usually between 0.2-0.5eV, whilst the activation energy for emission of single atoms is high, approximately 2.5eV. An interface controlled model is thus likely to dominate in this work. However, Simonsen *et al.* [44] demonstrated that the interface and diffusion controlled ripening models often do not have a strong influence on the size ordering of nanoparticle decay times, affecting only the time dependence (which is obviously also dependent on material specific parameters). Simonsen *et al.* [44] found modifications to the mean field assumption affected the WG model far more than the assumption of interface or surface controlled ripening.

In the following work, ESTEM is used to determine the sintering mechanism via observation of individual particles. The use of ESTEM allows for resolution of the nanoparticles down to $r=0$, compared to TEM which is limited by its phase contrast dependence. An alternative method often used to discriminate between mechanisms uses Particle Size Distributions (PSDs). As discussed in section 3.3.1, previous work [48, 55, 58, 59] suggests that PSDs are not a definitive method of deducing the dominant sintering mechanism as the initial PSD is usually poorly controlled.

Use of ESTEM allows for improved (relative to TEM) detectability of small particles combined with in situ observation of sintering [32]. This enables determination of the sintering mechanism via the observation of individual nanoparticles in a gas environment, as opposed to using PSDs with an external reactor.

5.2. Experimental Conditions

A model system of Cu/Si₃N₄ has been used to allow for a simplified understanding of the sintering of industrial catalysts. Si₃N₄ is also extremely resistant to high temperature reducing environments and thus provides a system where long term observations can be made at high temperatures and gas pressures. Cu/Si₃N₄ samples were produced by depositing 0.7nm of Cu onto MEMS (micro-electromechanical systems) chips [23]. The deposition was performed via the use of a JEOL JFC2300HR sputter coater. This provides crystal sizes that are easily observable in TEM and STEM, produce a strong diffraction pattern and are also comparable in size (approximately 5nm radius) to an industrial Cu catalyst (examination of Cu/ZnO/Al₂O₃ catalyst confirmed 3-10nm Cu particle radii).

The temperature range used during experiments was 400-550°C. At lower temperatures (below 300°C) differences in PSD between the beam exposed and unexposed areas are observed. This suggests that sintering mechanisms are not dominated by sample holder induced temperature changes and thus results are dependent on beam exposure time. By increasing the temperature the sintering rate is enhanced and thus the necessary total beam exposure is reduced (as the experimental time frame required decreases). This allows for observation at a rate of 1/5 minutes, with a 19.5µs dwell time, 1024x1024 pixels with an area of 0.23x0.23nm.

At temperatures greater than 500°C, PMC is observed to occur. Previous work has suggested that PMC occurs at lower temperatures and then progresses to Ostwald Ripening at higher temperatures [146, 147]. However, clearly the particle size, support binding and environmental factors will influence this scenario. Smaller nanoparticles have reduced binding strength to the support and migration becomes more facile [71]. Depending on the atom detachment and particle binding energies, a change in temperature will switch the energetically favourable mechanism. This is the likely explanation of the high temperature PMC observed here and has been previously discussed in detail by Chen and Ruckenstein [148].

Observation of the particles was undertaken at a magnification of 600kX using a modified JEOL 2200FS Environmental (Scanning) Transmission Electron Microscope (E(S)TEM) at the University of York. This is the first double aberration corrected environmental microscope which can provide sub-angstrom resolution in both STEM and TEM modes [32]. The microscope can currently provide gas pressures of approximately 3Pa which equates to

upwards of 10^4 monolayers of gas supply per second. Obviously particle size determination is highly dependent on microscope imaging conditions and these are discussed below.

5.2.1. Particle Size Measurement and Error Estimation

Each ESTEM sintering experiment was performed with constant microscope brightness and contrast settings. Changes in substrate and particle size sometimes necessitated adjustment between experiments, however. The particle size analysis was performed using a standard thresholding technique. Within a single image the relative sizes of each particle have an error based on the pixel size of 0.23nm (at a magnification of 600k with 1024x1024 pixels). This could obviously be reduced by decreasing the pixel size (2048x2048 pixels were used thus reducing pixel size to 0.125nm) however, thermal drift during image acquisition then becomes a problem. The absolute determination of particle size will be affected by focussing errors (or the microscopes information limit). As the threshold was kept constant throughout the experiment, the focal error will interact with threshold level to alter the magnitude of the error in each image. Each particle is also altering its actual size based on the single atom flux. As the motion of the single atoms is governed by random walk [149], there is an additional random component of r change between images. Change in r between images is thus a quadratic sum of the measurement error as a function of focal change and the random component of r change (noting that this component contains the Δr trend). The error for all calculations of r was thus taken by measuring the average image to image change in r . This calculation was only performed for particles where a trend in particle size change was (by eye) indiscernible from noise (i.e. not including a particle which is undergoing decay).

5.3. Cu/Si₃N₄ at 500°C in 3 Pa H₂

Sintering of the Cu nanoparticles on the Silicon Nitride substrate was observed in a H₂ 3 Pa environment at 500°C over the course of 210 minutes. As previously mentioned in section 5.1, there are two main sintering mechanisms: OR and PMC. In order to determine the mechanism of sintering, individual particle tracking is used. Looking at the pentagon of particles 8, 9, 10, 14, 16 in the centre of Figure 5.1, it can be seen that over the course of the experiment they begin to disappear and by the end of the experiment at 210 mins they are extinct. The larger particles grow in size, whereas smaller shrink. All particles remain immobile relative to each other; thus this mechanism is clearly OR.

This is further demonstrated by looking at the individual particle radii change with time (Figure 5.2), where particles smaller than 4nm all become extinct within the experimental time frame. The largest 4 particles show an average increase in radius of 0.45nm (Figure 5.3). The particle size increase should be roughly the same as the volume lost by smaller particles. The total volume change over the course of the experiment (assuming hemispherical particles) is 230nm^3 . Excluding the particles surrounding the experimental area and assuming an equal distribution of the lost mass between the remaining particles; means each particle increases in size by 26nm^3 . This provides an increase in radius of the average 7.21nm ($V=786\text{nm}^3$) particle of just 0.08nm. This is well within the estimated error of $\sigma_r=0.14\text{nm}$ calculated using the method outlined in section 5.2.1.

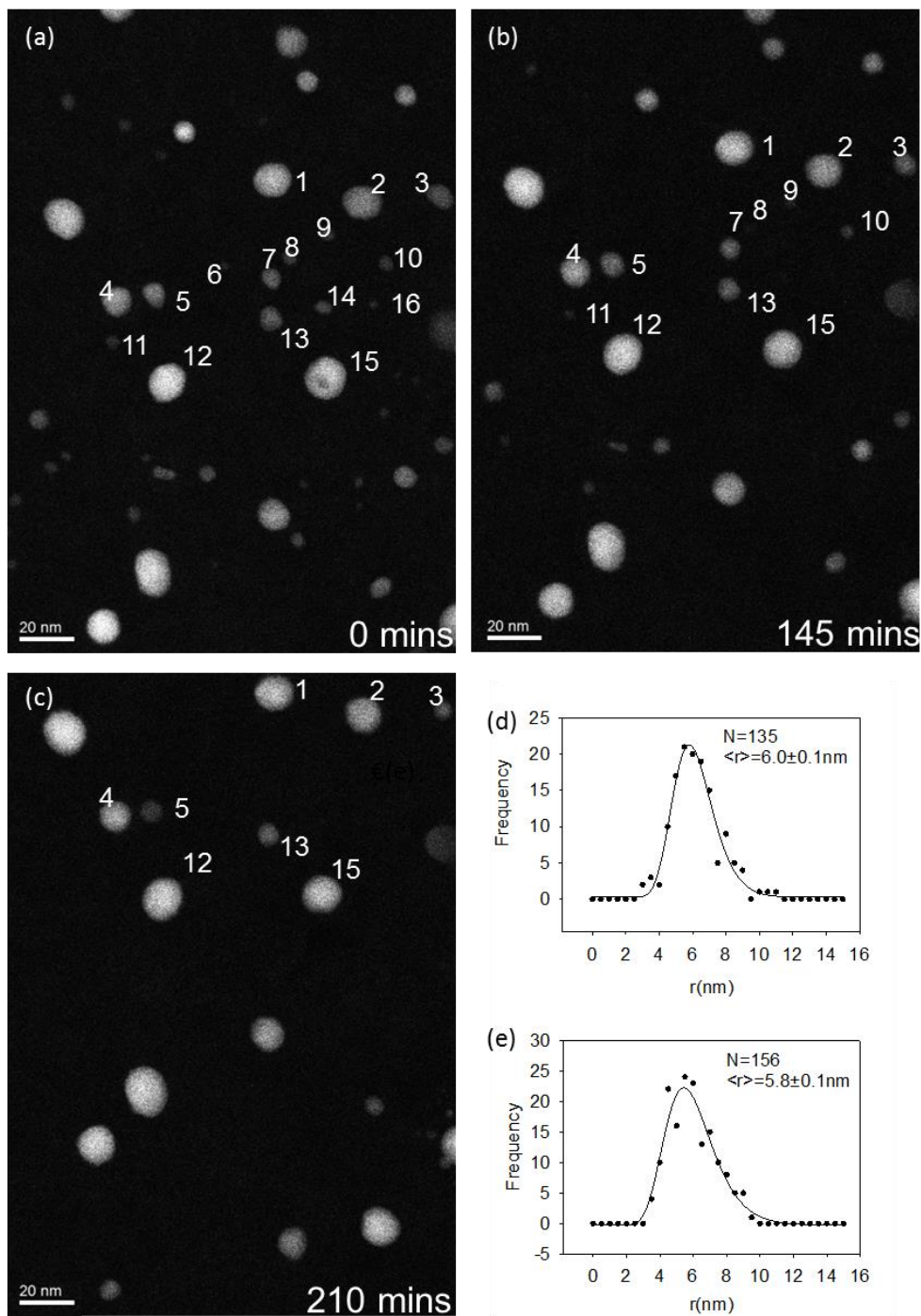


Figure 5.1: Cu/Si₃N₄ sintering via the Ostwald Ripening mechanism in 3 Pa H₂ (a) after 0 mins, (b) 145 mins, (c) 210 mins and (d) PSD (particle size distributions) of exposed beam area after 210 mins (e) PSD of unexposed area after 210 mins, indicating that beam effects do not significantly affect OR results.

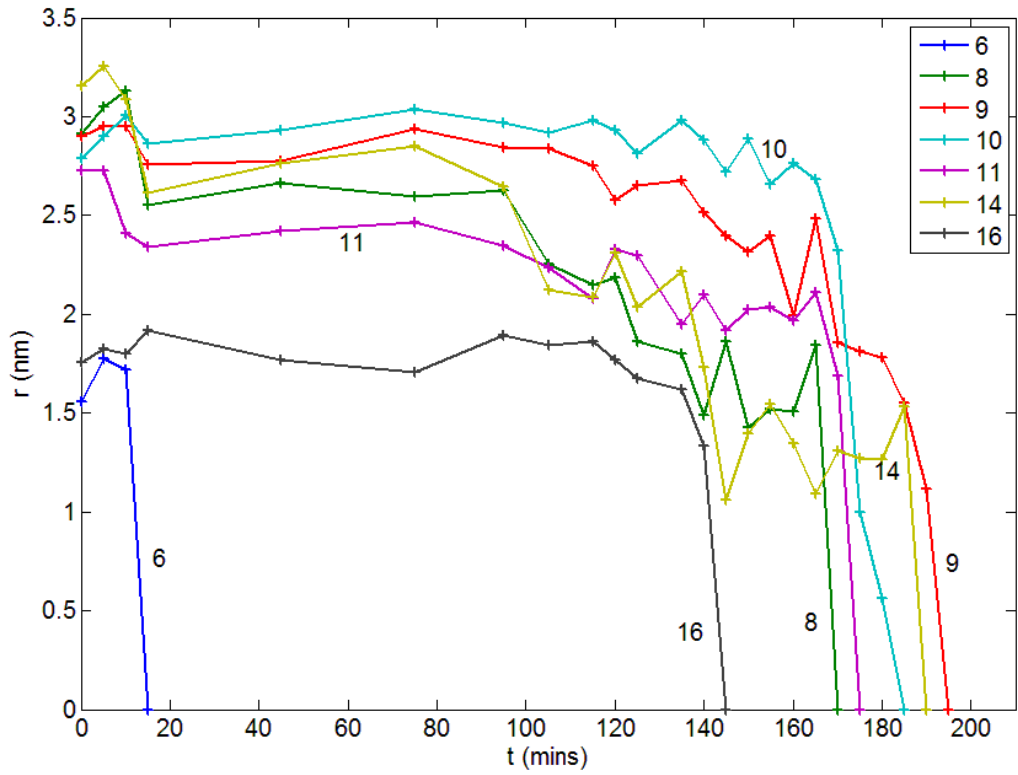


Figure 5.2: Experimental results for r less than 3.5nm at $t=0$. Error in r measurement is ± 0.14 nm.

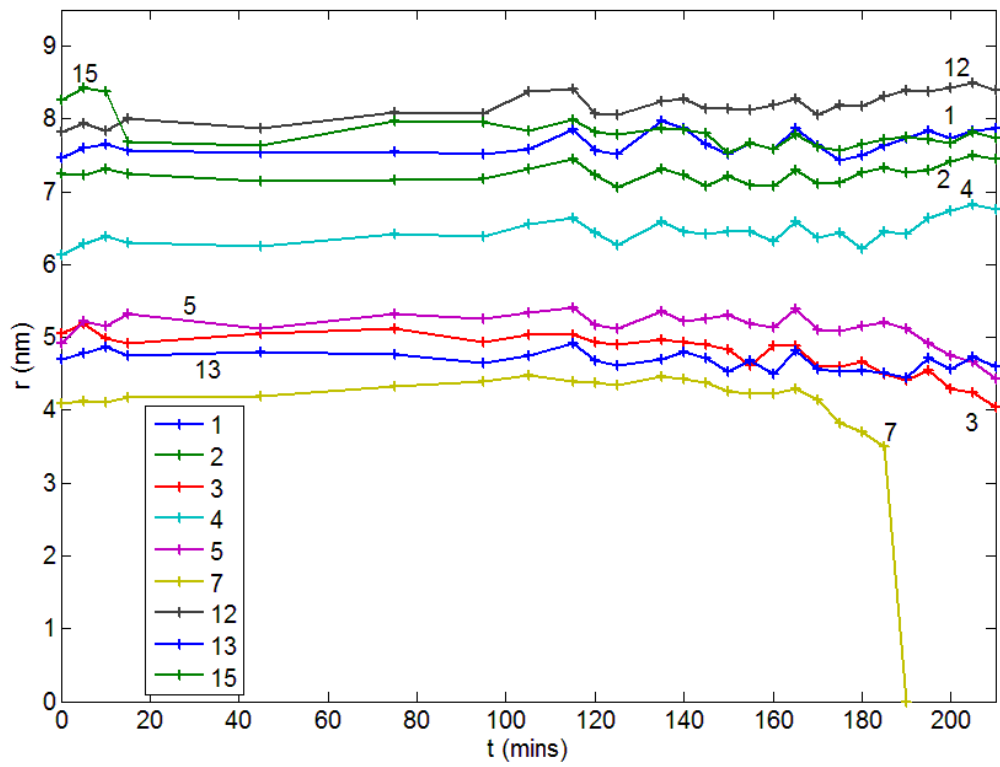


Figure 5.3: Experimental results for r greater than 3.5nm at $t=0$. Error in r measurement is ± 0.14 nm.

As discussed in section 5.1, the mean field assumption leads to size ordering of particle extinction times, $t(r=0)$. There are 2 obvious anomalous results observed from Figure 5.4. The low $t(r=0)$ value of particle 7 (comparable to approximately 3nm particles) and the high $t(r=0)$ value of particle 16 (compared to particle 6). Looking at Figure 5.1, it can be seen that particles 8,9,10 and 14 are close to particle 7 and become extinct at around the same time. This suggests that a ‘Domino’ effect may be observed, whereby particles are stabilised by a higher local concentration of atomic species due to decaying smaller particles. Once the smaller particles have decayed, these particles are then subject to interactions with larger local particles (in this case interactions of particle 7 with particles 1 and 2).

This concept was originally explored by Bartelt *et al.* [65] by examining the screening of diffusion fields of individual particles. If an OR system is interface limited, then diffusion is assumed to be infinitely fast and thus the diffusion field screening is ineffective. However, by assuming a finite value of D (diffusion coefficient), nearest neighbour screening was accounted for. The assumed value of D was still large enough that OR occurred well within the interface limited regime.

The change in particle size is driven by the difference in chemical potential between the particle and its surrounding area and is interface limited. However, the distance over which the surrounding areas chemical potential is in equilibrium is diffusion limited and thus gives rise to strong local correlations in OR [66]

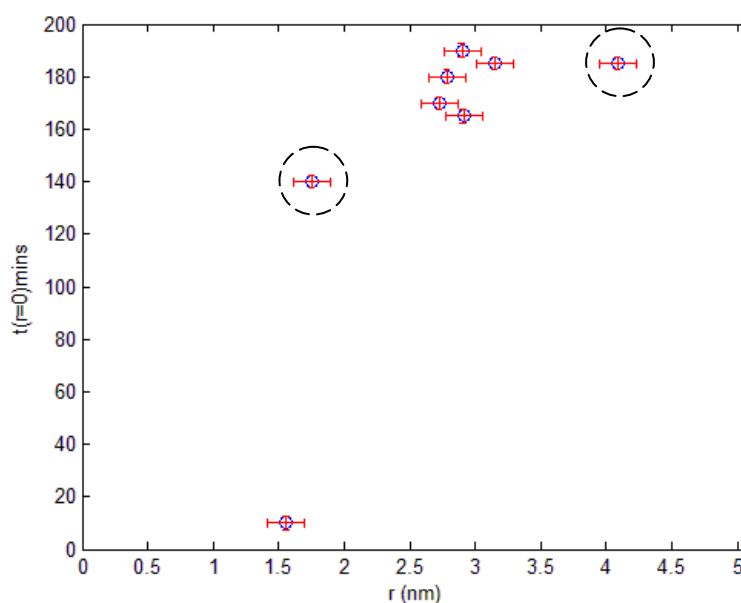


Figure 5.4: $t(r=0)$ against $r(t=0)$. Anomalous extinction times are observed for particles 7 and 16 (dashed lines). Particle extinction times are also not size ordered for $r=2.5-3.5$ nm particles.

5.4. Local Correlation and Mean Field Models of Ostwald Ripening

The original WG model is governed by the GT relation and uses the mean field assumption. This states that individual particles exchange atomic species with a constant concentration of single atoms which exist on the substrate, thus ensuring size ordering of extinction times. The substrate atomic concentration is determined by the average particle size (equation 5.1) and thus when r is less than r_c , dr/dt is negative, and vice versa. Obviously, this model does not take different particle environments (e.g. size/number of surrounding particles) into account.

Bartelt *et al.* [65] used a Voronoi construction (Figure 5.5) to define the interaction range of particles and thus determine the local atomic concentration (ρ_{local}). This approach was utilised by several other authors to provide an improved understanding of: Ag with STM (Scanning Tunnelling Microscopy) [64]; Si with low energy electron microscopy [66]; and Pt/SiO₂ with TEM [44].

The interface limited local single atom concentration was calculated using equations 5.6 and 5.7 which consists of contributions from each of particle i 's nearest neighbours (j). These contributions are weighted according to the exposed surface area of particle j ($2\pi r_j$) and the interparticle distance (d_{ij}). Note that j' refers to other nearest neighbour particles in order to normalise the weighting.

$$\rho_{local} = \sum_j \frac{1}{2} (\rho_{r_i} + \rho_{r_j}) \sigma_{ij} \quad 5.6$$

$$\sigma_{ij} = \frac{\left(\frac{2\pi r_j}{d_{ij} - r_i - r_j} \right)}{\sum_{j'} \left(\frac{2\pi r_{j'}}{d_{ij'} - r_i - r_{j'}} \right)} \quad 5.7$$

The diffusion limited local single atom concentration is calculated by assuming a pairwise exchange of atomic species between particle i and its neighbours, j . As with the interface controlled model, the interaction is weighted by the distance between the particles (d_{ij}). However, each neighbour interacts directly with particle i , as opposed to through the averaged local concentration calculated in the interface controlled mode. Derivation of these differential equations can be found in section 3.4.

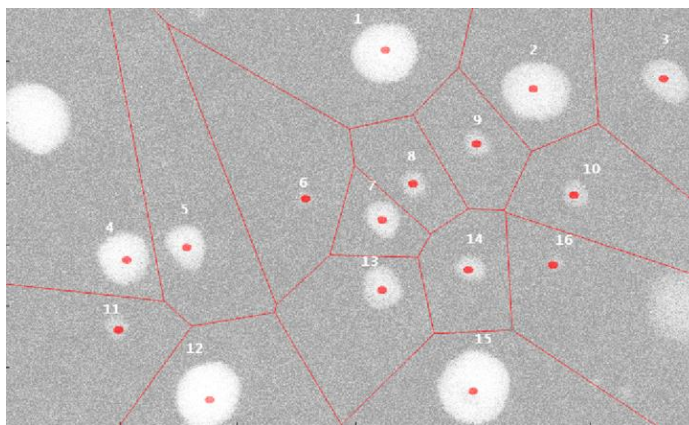


Figure 5.5: Voronoi construction overlaid on Figure 5.1. Nearest neighbour particles, as defined by the construction, contribute to the local single atom concentration.

To calculate dr/dt with both the mean field and local correlation concentration assumptions, determination of E_{Tot} is required. This can be performed in two different ways: (i) a nonlinear least squares fit to the experimental data in Figure 5.2 and Figure 5.3 or (ii) minimisation of difference between $t(r=0)_{\text{sim}}$ and $t(r=0)_{\text{exp}}$ via iterating over a varying value of E_{Tot} . The former procedure has the advantage of having a greater E_{Tot} resolution, as all data points are accounted for (rather than just $t(r=0)$). However, this also allows fluctuations in the experimental r to determine E_{Tot} . As the weight of all data points is constant (no artificial weighting was applied), then the ordinary differential equation solving algorithm used can easily become trapped in a local minima, where fluctuations whilst r is greater than r_c (critical radius) are satisfied. This leads to poor fitting in regions when r is less than r_c , which is enhanced for large $t(r=0)$ particles (as there is a greater proportion of time where r is large than r_c). The second procedure removes this issue, but is less accurate due to only the $t(r=0)$ data point being used. To minimise the disadvantages of both of these effects, procedure (ii) is used to provide an initial estimate for input into procedure (i).

Values of the bulk surface energy of Cu(111) are determined either theoretically or experimentally at melting temperature or over a temperature range. Values in [150-155] are between 1.952-2.14 at 500°C in UHV and values in HV and H_2 are obtained from [79]. The surface energy γ , is initially assumed to be constant with r , but Campbell *et al.* [67] obtained an improvement in model predictions by use of the Modified Bond Additivity (MBA) model, which allowed for introduction of size dependent surface energy and scaling of this to other FCC metals [67, 138, 156]. Ouyang *et al.* then adapted this approach to incorporate reaction environment dependent surface energies [68]. The lattice parameter of Cu is 0.361nm in bulk [154], v is usually taken to be between 10^{-12} - 10^{-14} [76] and K (equation 5.3) simplifies to v/a when a hemispherical particle shape is assumed (thus $\theta=90^\circ$).

Using the fitting procedures for E_{Tot} outlined above, a value of 222.93kJ/mol was obtained from procedure (ii), which was then input into (i) to obtain $E_{\text{Tot}}=222.35\pm 1\text{kJ/mol}$. Note that the fitting was only performed on particles 8,9,10, 11 and 14. This was because the remaining particles either do not reach $t(r=0)$ in the experimental time frame, or were identified as anomalous in section 5.3 (particles 6, 16 and 7).

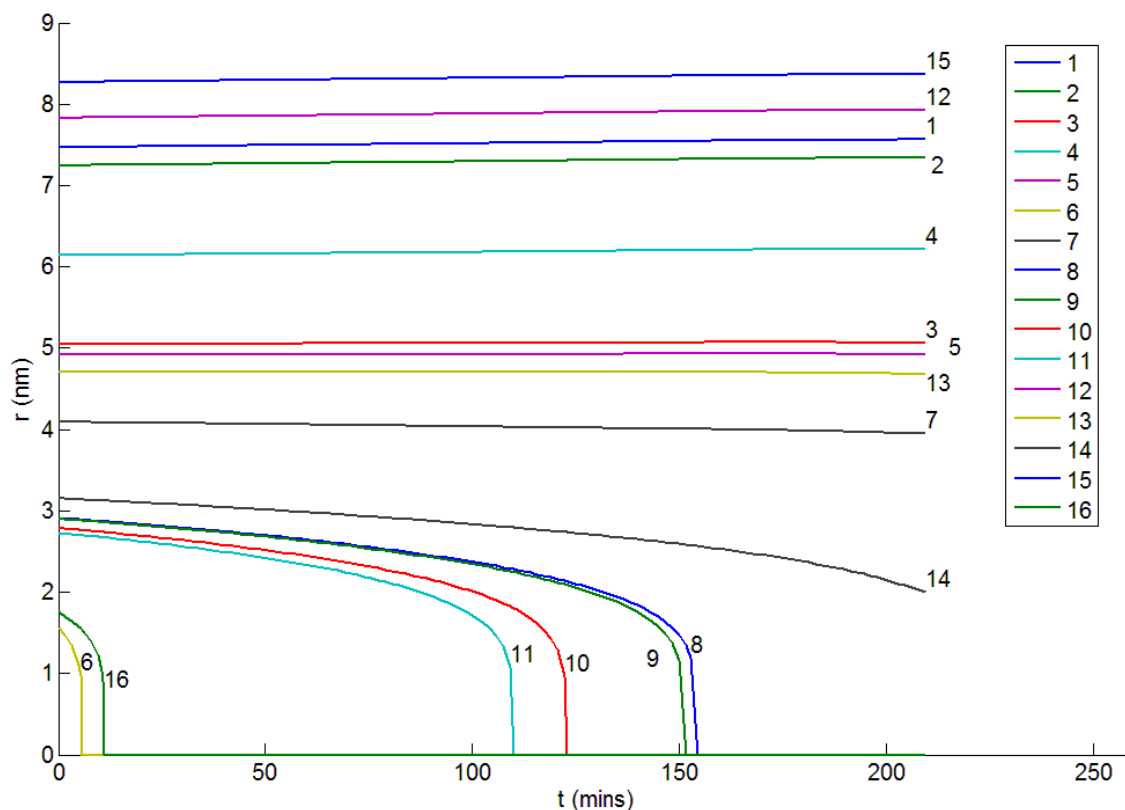


Figure 5.6: Interface limited mean field assumption used with $E_{\text{Tot}}=222.34\text{kJ/mol}$ to model Cu/Si₃N₄ at 500°C in 3 Pa of H₂.

Repeating procedure (ii) for the local correlation model gives $E_{\text{Tot}}=217.50\text{ kJ/mol}$ and applying (i) $E_{\text{Tot}}=217.90\pm 0.4\text{kJ/mol}$. Note that the E_{Tot} value used with the local correlation model is less than that obtained previously with the mean field assumption. This is explained by examining r_c as particles become extinct. For the mean field model, all particles are affected by the decay of a single particle, as the substrate concentration of single atoms will decrease. However, as the local model only accounts for nearest neighbour variations, the substrate concentration of single atoms will be unaffected by a particle decay. As E_{Tot} simply reflects the activation energies for diffusion and detachment of single atoms [138], it must decrease in the local model case to reflect the overall higher substrate concentration of single atoms.

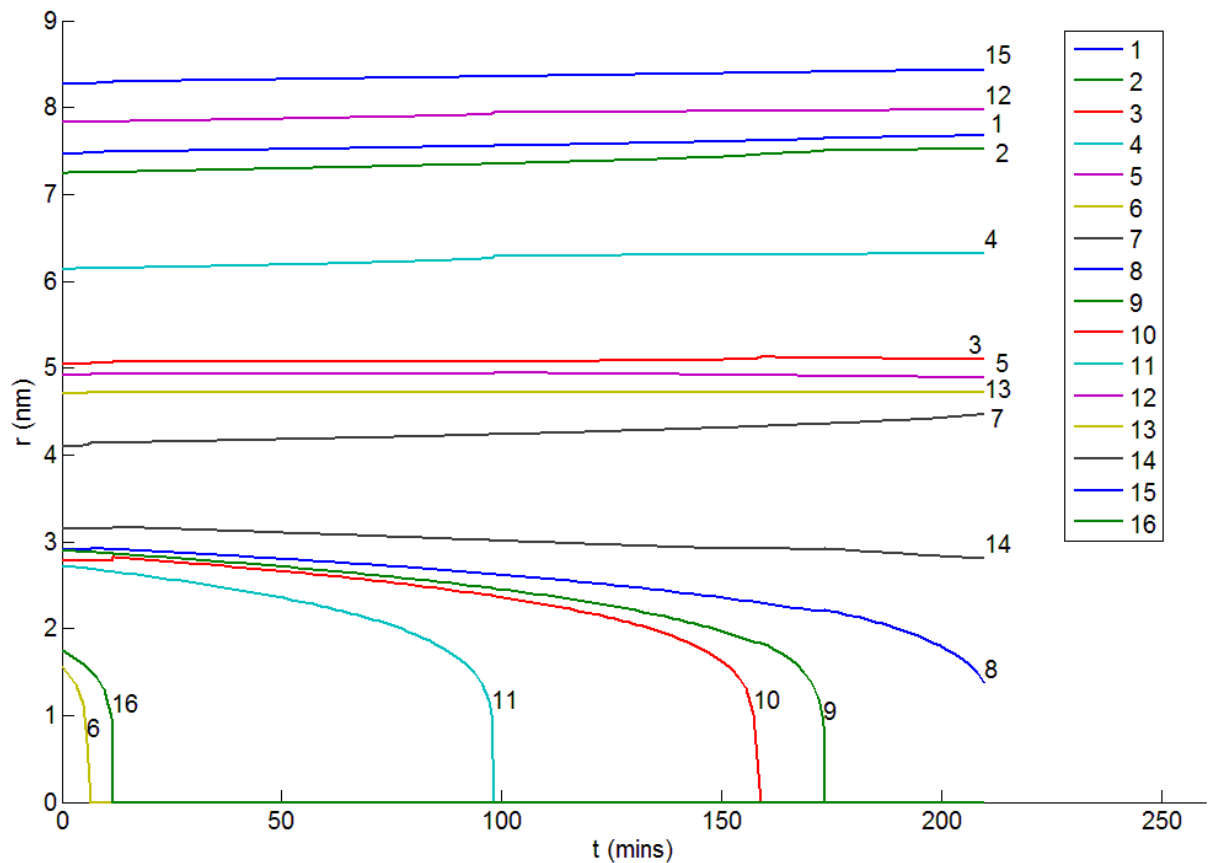


Figure 5.7: Interface controlled local correlation assumption used with $E_{\text{Tot}}=217.90\text{kJ/mol}$ to model $\text{Cu/Si}_3\text{N}_4$ at 500°C in 3 Pa of H_2 .

From Figure 5.6 and Figure 5.7 it can be seen that neither kinetic model predicts a non size-ordered extinction time, which is observed experimentally for r approximately 3nm particles. Both models also fail to predict the low extinction time of particle 7 and the high extinction time of particle 16 (relative to particle 6). The spread of $t(r=0)$ for particles 2-4nm initial radii is considerably smaller when the mean field assumption is made instead of the local correlation. This implies a better fit with ESTEM experiments for the mean field model. The reason for this is the sensitivity of the local correlation model to a size dependent surface energy. By its nature, the local correlation model has the substrate concentration of adatoms determined by a smaller region than the mean field model. As previously discussed, this leads to a lower estimate of E_{Tot} and also a greater spread of $t(r=0)$ (as particle extinctions will have only local effects). This also means that a change in the surface energy of a particle will be enhanced in the local correlation model as it is damped less by averaging. Thus, to improve this model γ could be taken to be a function of r . As previously discussed, the surface energy has been shown to vary with r and reaction environment but it is currently difficult to quantify this effect. Attempts have been made by Campbell *et al.* [67] and Ouyang *et al.* [68]. Their modifications allow for an increase in surface energy with decreasing r , thus leading to a faster decay of smaller particles. However, Simonsen *et al.* [44] found an almost linear decay of $r(t)$

and suggested size dependent gas effects as a possible complication. The approach taken here is that used by Yang *et al.* [69] where it was assumed that below $r=3\text{nm}$, $\rho(r)$ is much greater than ρ_{local} or ρ_{r_c} , thus modifying equation 5.2 to:

$$\frac{dr}{dt} = \frac{-K\Omega}{r} e^{\left(\frac{-E_{T0t}}{kT}\right)} e^{\left(\frac{2\gamma\Omega}{kTr}\right)} \quad 5.8$$

To find the r limit at which $\rho(r)$ is much greater than ρ_{local} , the nearest neighbour bond additivity model used by Campbell *et al.* [67] has been applied. Starting from a single atom, three atoms are added for every one atom in the layer above to produce an FCC pyramid structure. The number of broken bonds (coordination number for bulk FCC is 12) is then calculated for different particle sizes. In Figure 5.8 it can be seen that an increase in the number of broken bonds is observed at $r=3\text{nm}$, corroborating the applicability of the work by Yang *et al.* [69].

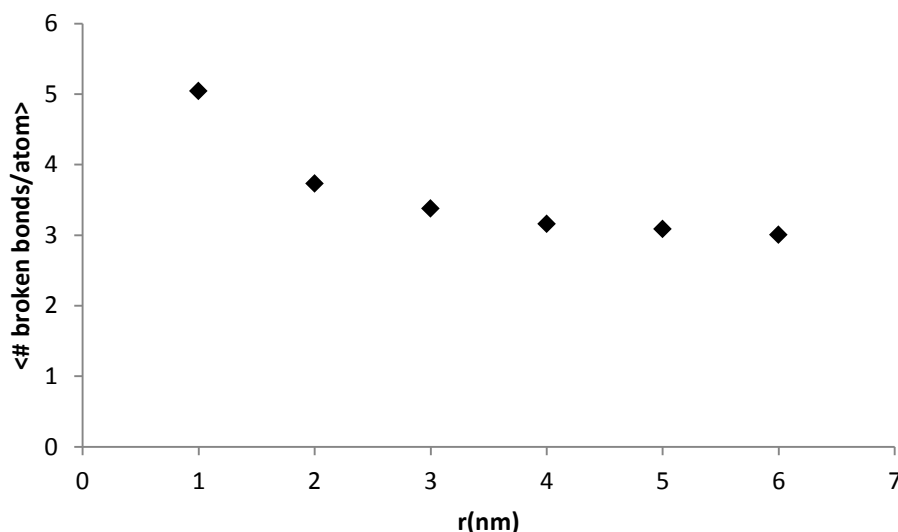


Figure 5.8: Using the nearest neighbour bond additivity model [67], the average number of broken bonds per atom at the surface is calculated for pyramidal FCC particles at different values of r . The number of broken bonds for bulk FCC is 3.

Taking the local correlation model with the assumptions of equation 5.8 for particle radii of less than 3nm produces Figure 5.9. Particles with r approximately 3nm have a $t(r=0)$ spread of 100 mins, compared to around 150 mins without $\gamma(r)$, thus meaning that particle 8 is observed to decay within the experimental time frame. This demonstrates the significant effect surface energy has on WG models of particle sintering and the importance of further work adapting kinetic models to fully account for particle size.

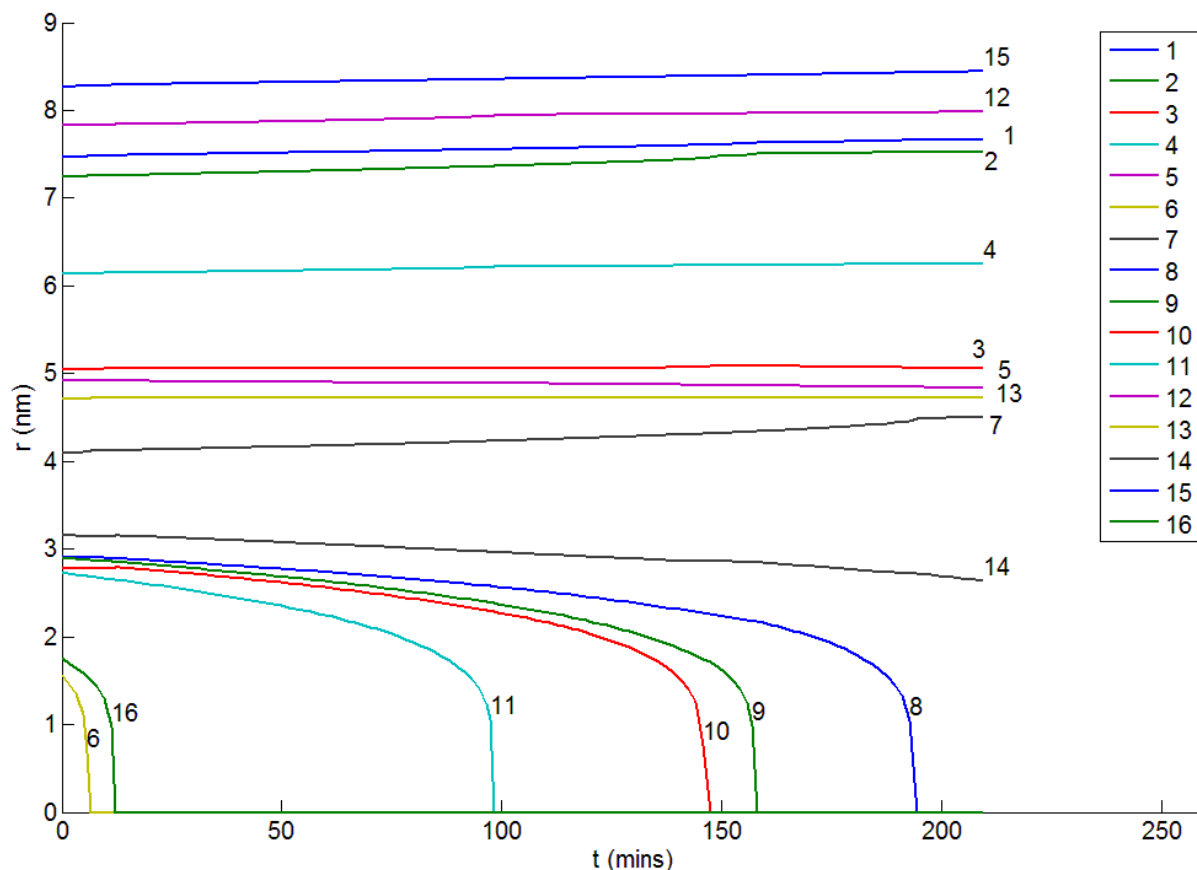


Figure 5.9: Interface limited local correlation assumption with $\gamma(r)$ [69] used with $E_{\text{Tot}}=217.90\text{kJ/mol}$ to model $\text{Cu/Si}_3\text{N}_4$ at 500°C in 3 Pa of H_2 .

There are several other factors that are not included in the kinetic models: particle shape; next nearest neighbours and particle height. As HAADF STEM is sensitive to the number of protons in an atomic column, intensity is a function of both Z (atomic number) and the number of atoms in the column. Although atomic column resolution of Cu is challenging, due to the low Z , variation in particle height will still produce intensity changes. These were investigated by looking at linescans and average particle intensities. This showed that particle height is a linear function of r , suggesting that there is a constant width:height relationship between particles. The hemispherical assumption of particle shape is therefore reasonable in terms of also providing a constant width:height relationship. As previously performed by Bartelt *et al.* [65] and Simonsen *et al.* [44], local correlation was assumed to only be influenced by nearest neighbour particles. This assumption is valid in that single atoms can be thought of as random walkers and are thus subject to a Gaussian concentration profile [149, 157]. However, this neglects particle size effects and the concept of a weaker or stronger next nearest neighbour interaction depending on the screening provided by the nearest neighbour. To account for next nearest neighbour interactions a Kinetic Monte Carlo model has been implemented. This provides the advantage of making no prior assumptions about the endpoint of a single atom,

thus allowing interaction at scale between the mean field and nearest neighbour interactions which is determined by the system under observation.

5.5. Kinetic Monte Carlo Simulations of Ostwald Ripening

KMC is designed to input information on fundamental processes and mechanisms and then examine the time evolution of them stochastically. The rate of the processes is usually parameterised by production of an activation energy via the Arrhenius equation:

$$P(\Delta E) = e^{\left(\frac{-\Delta E}{kT}\right)} \quad 5.9$$

The value ΔE is the activation energy for the process in question (e.g. adatom diffusion), T is temperature, k is Boltzmann's constant and $P(\Delta E)$ is the probability of transition. The KMC code produced by Lucas *et al.* [158] has been used in this study.

The main advantage of KMC is overcoming the 'time scale problem' suffered by Molecular Dynamics (MD) by analysing the problem with a state to state method. Rather than observing atomic vibrations, an assumption that atoms undergo diffusive jumps is made, with the result being that vastly longer timescales can be observed (greater than 1s) compared to MD[159].

Particles have been assumed to be circular and 2D, with locations and sizes matching particles measured in the above ESTEM experiment. There is some error in the particle size representations due to the constraints of producing a circular structure in atomic units. This results in similarly sized particles such as 6 and 16 being represented with equal area in the KMC simulations.

Input parameters were calculated for KMC simulations by using the E_{Tot} value derived from the local correlation model of 217.90kJ/mol in order to attempt to simply quantify the effect of substrate and gas environment. Assuming that diffusion energies are typically 40% of adsorption energies [138] then equation 5.4 simplifies to the diffusion energy= $(\Delta H_{\text{sub}} - E_{\text{Tot}})/1.5 = 0.83\text{eV}$, where $\Delta H_{\text{sub}} = 337.4\text{kJ/mol}$ [154]. The energy to leave a cluster is a sum of the activation energies for bond breaking (3 bonds are assumed in this 2D FCC system) and diffusion to one atomic step away from the cluster [160, 161]. The energy to leave a cluster is then found to be $(0.83 + 0.32 * 3) = 1.8\text{eV}$, where the bond energy is assumed to be 0.32eV from

[162]. These values compare well with the parameters used by Lucas *et al.* [158] for simulations of OR. It should be noted that these simulations are only intended as an investigation into particle interaction regions, rather than a quantitative study of KMC OR. Thus, parameters such as adatom diffusion along an island edge have been chosen to maintain a circular equilibrium shape (as implemented in [158]).

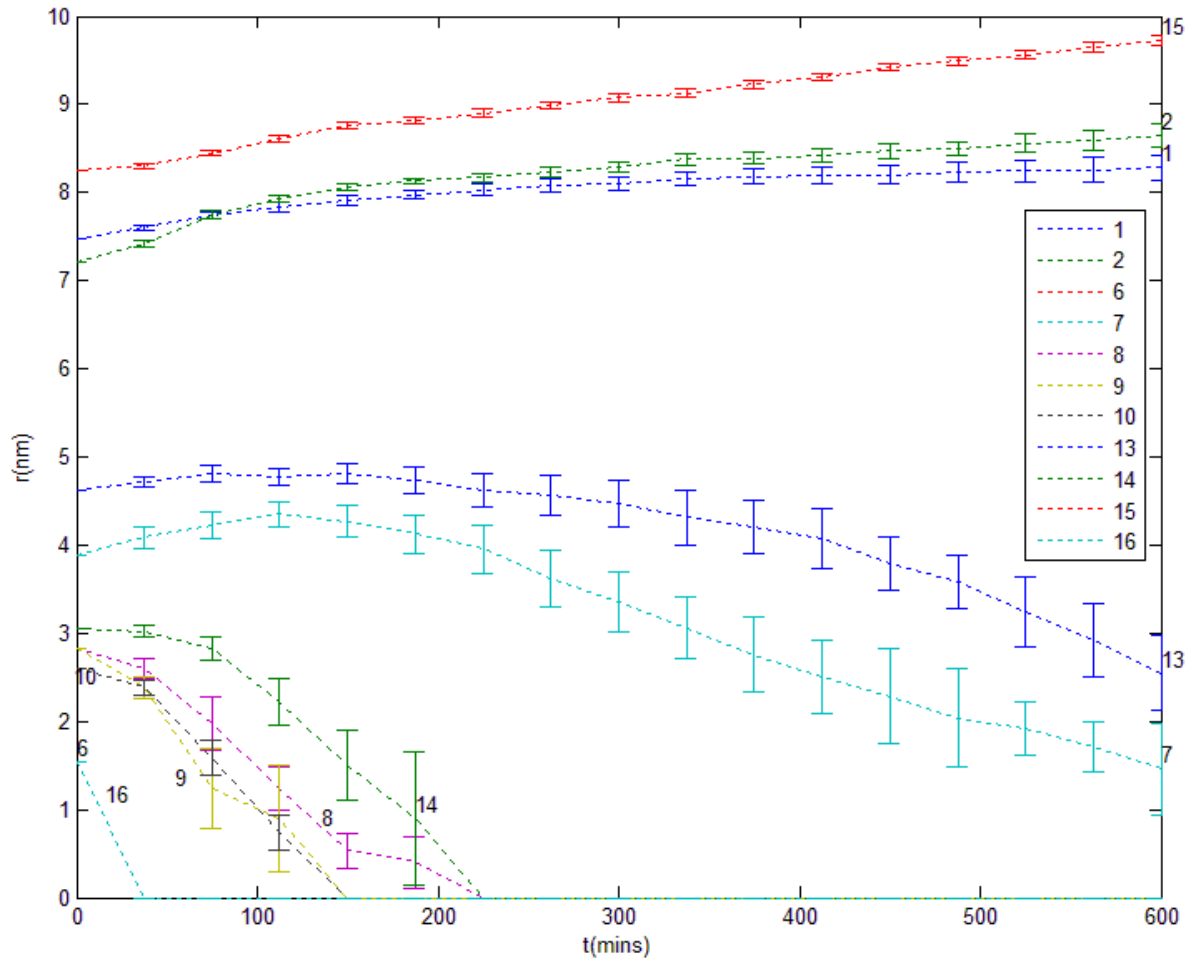


Figure 5.10: KMC simulation of right hand area of Figure 5.1. A reduced area is used in order to decrease the simulation time. Particles have a constant adatom emission probability and dr/dt is thus dependent on the single atom concentration and a particles collision cross-section. In the kinetic models the single atom concentration is dependent on $\exp(1/r)$ from the GT relation (equation 5.1). Simulations are averages of 50 iterations (errors are the standard deviation of these runs). This averaging technique was performed by both Morgenstern *et al.* [163] and Zoontjens *et al.* [164] in similar KMC simulations.

KMC simulations of particle 7 (Figure 5.10) show that as its surrounding particles become extinct there is a decrease in the number of atom captures by particle 7 (due to the lower local concentration of single atoms). This results in a change in the sign of dr/dt and a steady decrease in particle size (after approximately 120mins), which is due to the constant atom emission probability. In the differential models the atom emission probability has a reciprocal exponential dependence on r . The KMC model shows the same size dependent extinction

times as predicted by both the mean field and local correlation models. This suggests that the nearest neighbour approximation is not limiting the system, as otherwise non-size ordered extinction times would be observed.

Other WG model assumptions (discussed in section 5.4) are based on the shape of nanoparticles and the homogeneity of the support. Although Si_3N_4 usually approaches a flat, amorphous support, local inhomogeneities cannot be ruled out. This will impact both the concentration and diffusion vector of atomic species thus affecting both the shape and size of nanoparticles [79, 165, 166]. These factors are certainly influenced by the gas environment. A HV study under the same experimental conditions as used in the H_2 Cu/ Si_3N_4 experiment is discussed next.

5.6. The Effect of H_2 and Substrates on Ostwald Ripening

5.6.1. Cu/ Si_3N_4 at 500°C in HV Conditions

Using the same specimen preparation technique discussed in section 5.2, Cu sintering was observed under HV (approximately 1.2×10^{-7} mbar). To ensure beam effects were not inhibiting the particle sintering, low magnification (300k) images were taken of the area surrounding the region in Figure 5.11 and 3 other areas. A lognormal distribution was then fitted to each providing an average particle size of 4.5 ± 0.1 nm for the beam exposed region and 4.6 ± 0.1 nm for the unexposed regions.

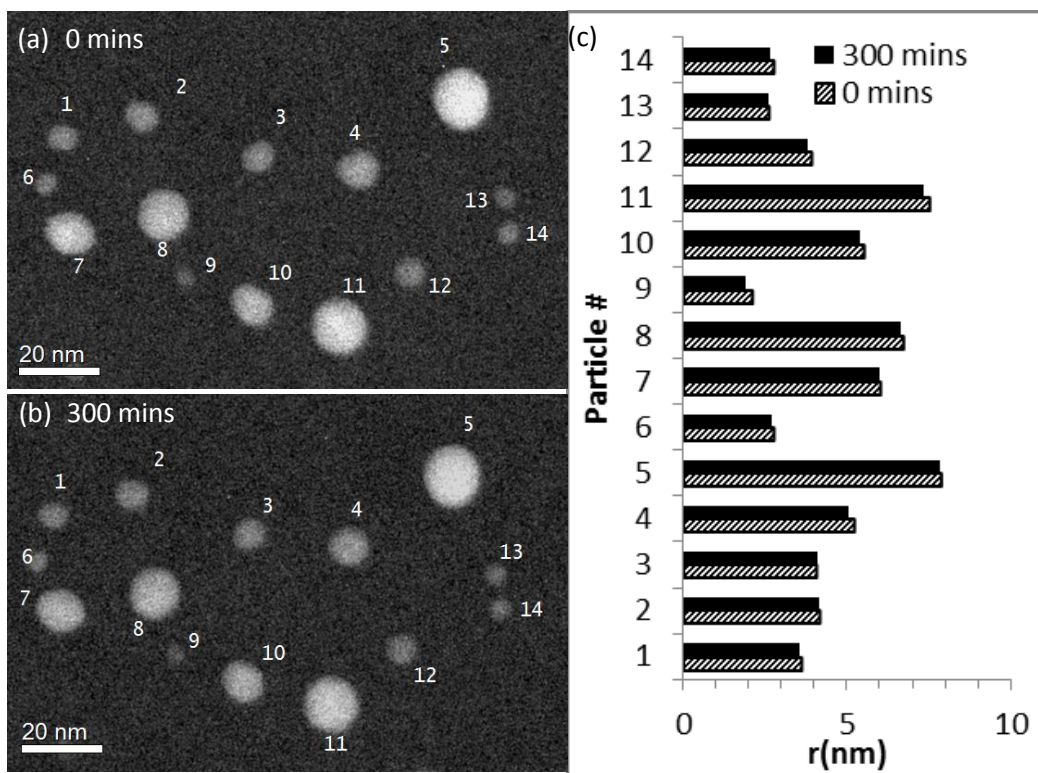


Figure 5.11: Cu/Si₃N₄ at 500°C in HV conditions after (a) 0 mins and (b) 300 mins showing an $\langle \Delta r \rangle = 0.07$ nm from (c), the particle r at 0 and 300 mins. Note that the apparent loss of mass from 0-300 mins is likely due to systematic error as corresponding increases in mass are observed in other images.

As can be seen from Figure 5.11, despite particles remaining in the same location, no discernible movement of atomic species is observed between particles. This suggests that H₂ is enhancing OR via detachment and/or diffusion rates. Previous work on the sintering of Cu in a gas environment has focussed on the industrially relevant system of Cu/ZnO/Al₂O₃. Sun *et al.* [167] measured activity over a 50 hour period at 523K and observed accelerated ageing on increasing the H₂ or CO partial pressures. Using Cu/ZnO, Kuechen [81] observed enhanced sintering of Cu particles with the presence of CO. Rasmussen *et al.* [82] use DFT (Density Functional Theory) to assess the stability and mobility of Cu-x (where x is Cu, OH, CO, CH₃O, HCOO) species on Cu particles and a ZnO support. They investigate the stability of the various species at different temperatures and pressures, then assess the diffusion energy barriers in each case. PMC is shown to be the preferential sintering mechanism in industrially relevant Water Gas Shift reactions, however when the particle size is sufficiently large (such that bonding to the substrate restricts migration) Ostwald Ripening becomes the dominant mechanism. Gas induced shape changes are investigated in CO and H₂ with Cu/ZnO systems [79, 168] and Cu/graphite [169].

In conclusion, significant Ostwald Ripening is observed in H₂ with 8 particle decays over a 200 minute period. After observation for 300 minutes there has been no detectable changes in a system under the same experimental conditions, but in HV. Further work will now look to establish whether the influence of H₂ on OR is a support independent result.

5.6.2. Cu/C at 500°C in H₂

A simple model system to further investigate gas dependent sintering is Cu/C. Carbon is a widely used support in electron microscopy due to the capability to fabricate it amorphously. Initial experiments showed that exposure to O₂ or prolonged (greater than 5 hours) exposure to H₂ at high temperature (greater than 700°C) leads to any tears in the film propogating. This clearly makes individual particle tracking impossible. Using experimental conditions of 500°C in 3Pa of H₂ causes no noticeable effect to the C-film stability within the experimental time frame of around 120 minutes. The geometry of the observed nanoparticles can be seen in Figure 5.12, with the individual particle sizes as a function of time shown in Figure 5.13 and Figure 5.14.

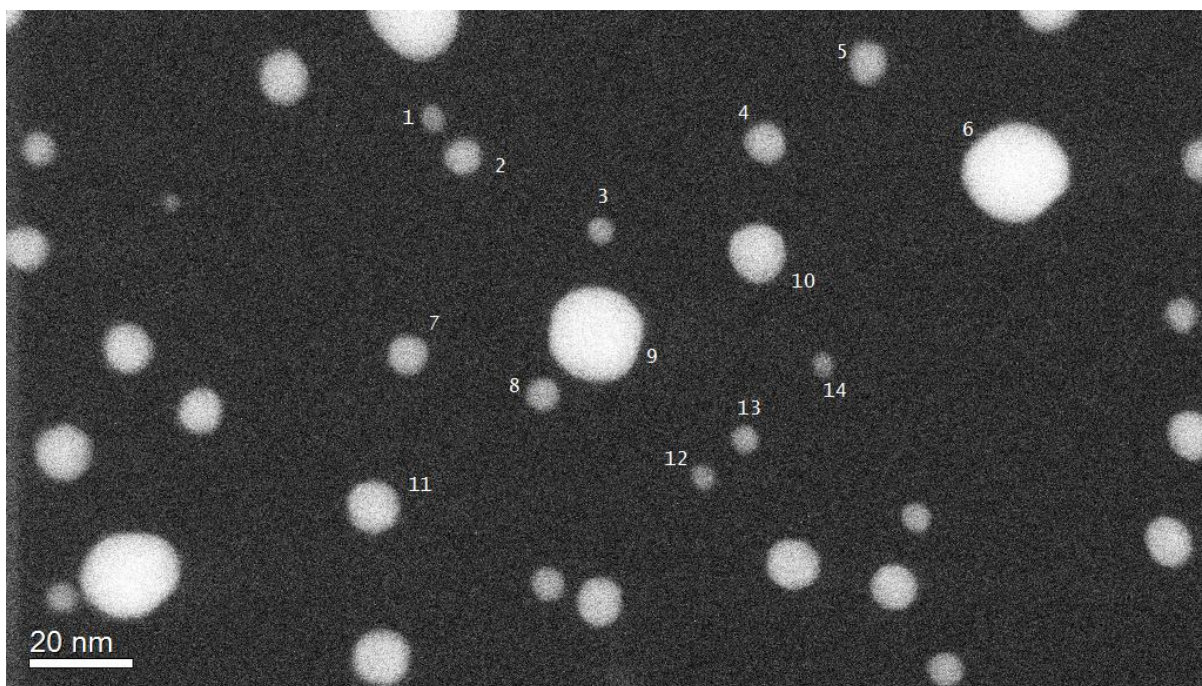


Figure 5.12: Map of experimental area used for observations of Cu/C at 500°C in H₂.

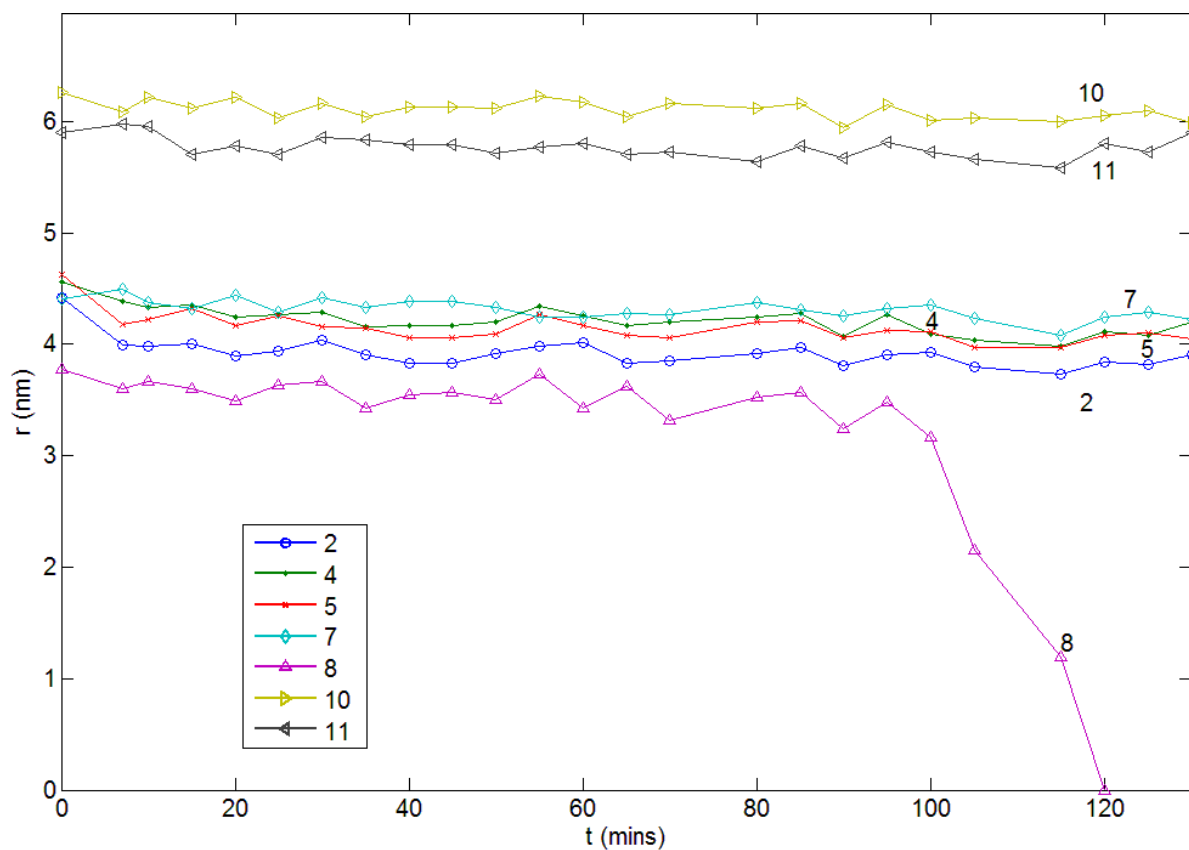


Figure 5.13: Experimental results for r greater than 3.5nm at $t=0$. Error in r measurement is ± 0.11 nm.

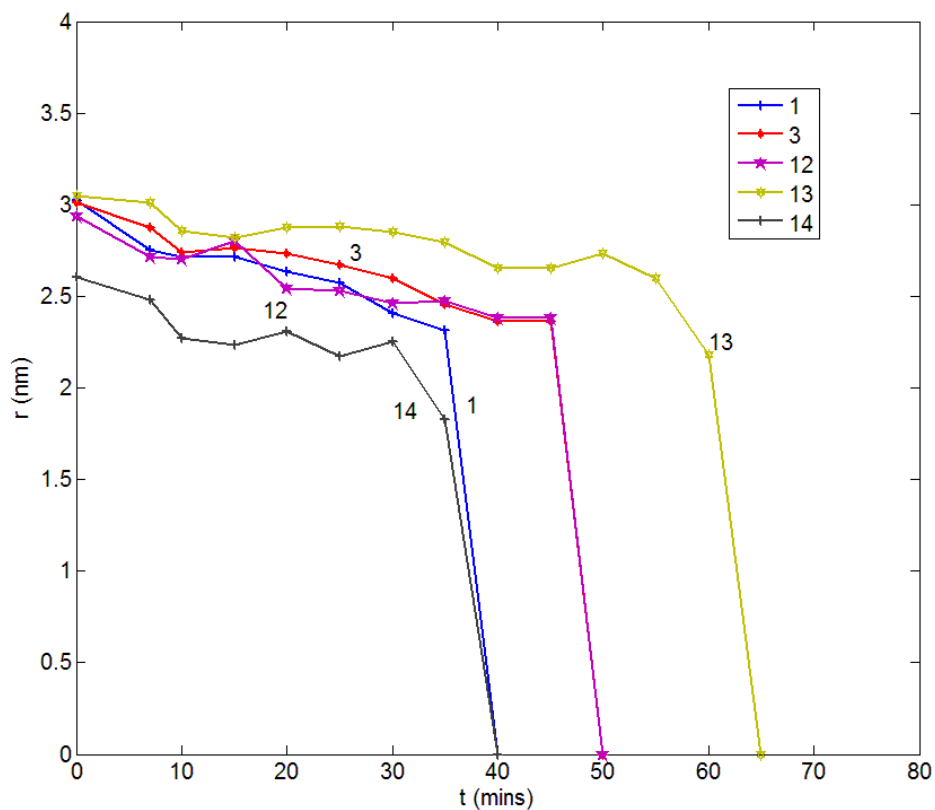


Figure 5.14: Experimental results for r less than 3.5nm at $t=0$. Error in r measurement is ± 0.11 nm. Observation frequency is 5-10mins.

Examining Figure 5.13 and Figure 5.14, there is a clear size dependence, with particles where $r(t=0)$ is greater than 4nm undergoing little observed size change (as discussed in section 5.3), whilst smaller particle decay is nearly size ordered. The observation frequency clearly influences this conclusion as differences in decay times cannot be resolved for particles such as 1 and 14. This must be considered when comparing the experimental data with WG-type models.

Both the Mean Field and Local Correlation (Figure 5.15 and Figure 5.16) models predict the lowest $t(r=0)$ for particle 14, followed by a group of 12,3 and 1. The Local Correlation model predicts a change in ρ_{local} of particle 13, due to the local extinction of particle 12. This is clearly observed by the shift in gradient observed-and also correlates with the 65 minute extinction time observed experimentally. Further improvement by the Local Correlation model is also obtained by the extinction of particle 8 within the experimental time frame, which is not predicted using the Mean Field model. However, the increase in size of particle 2 (due to alteration of ρ_{local} by particle 1) is clearly not experimentally observed and demonstrates the overestimation error introduced when calculating ρ_{local} at the edge of the experimental area.

This interesting artefact of the modelling procedure is observed because as particle 1 decays, its contribution to ρ_{local} increases exponentially as r tends to 0. If other local particles (i.e. particle 2) are large in comparison, then the contribution from particle 1 will dominate the local mean concentration. This leads to a sudden increase in the r of particle 2 just before particle 1 becomes extinct. However, in the diffusion controlled model, the driving force is a pairwise exchange of atoms from particle 1 to its nearest neighbours, including particle 2. The change in averaging (described in section 3.4) damps the effect of particle 1.

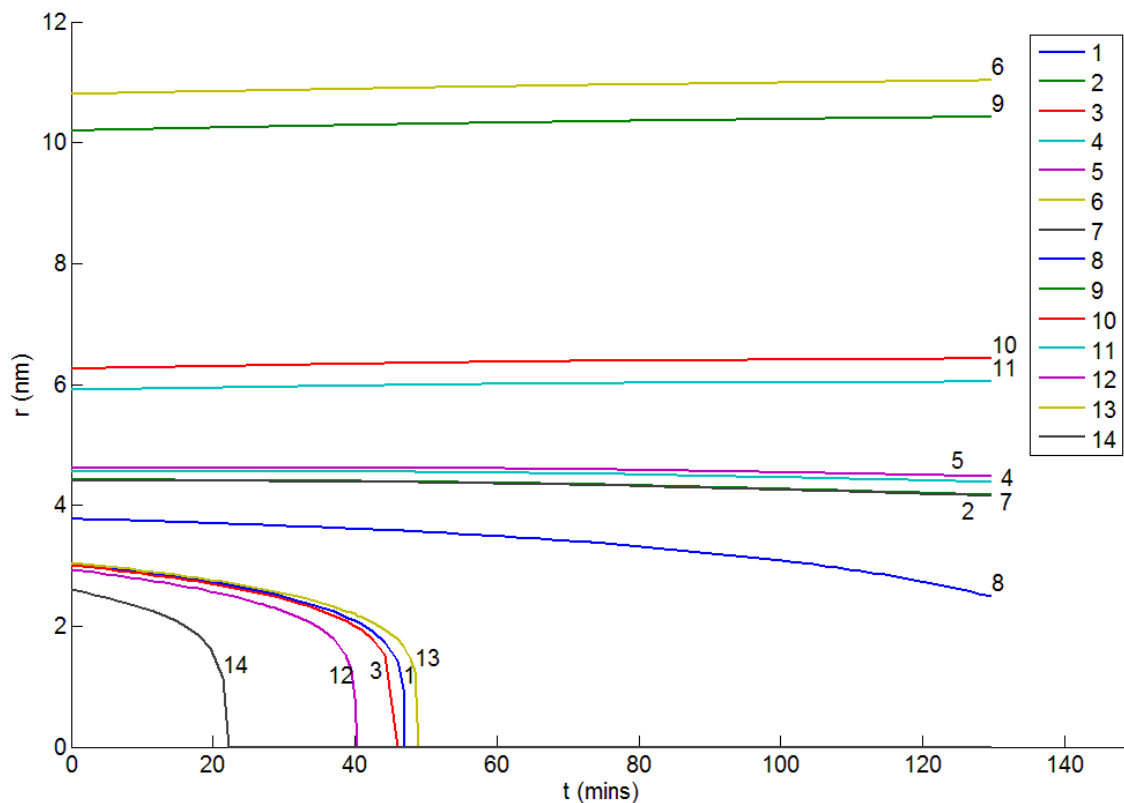


Figure 5.15: Interface limited mean field assumption used with $E_{\text{Tot}}=213.25\text{kJ/mol}$ with an error of 1.69kJ/mol .

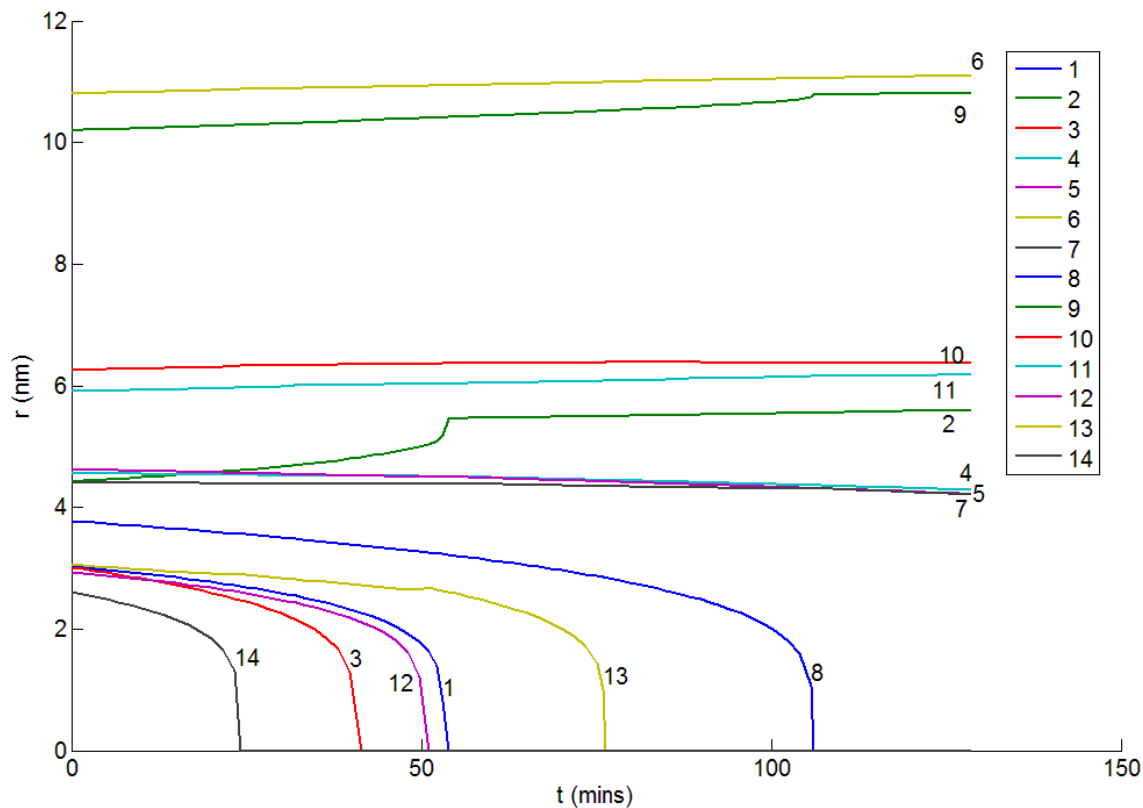


Figure 5.16: Interface limited local correlation assumption used with $E_{\text{Tot}}=209.50\pm 2.39\text{ kJ/mol}$.

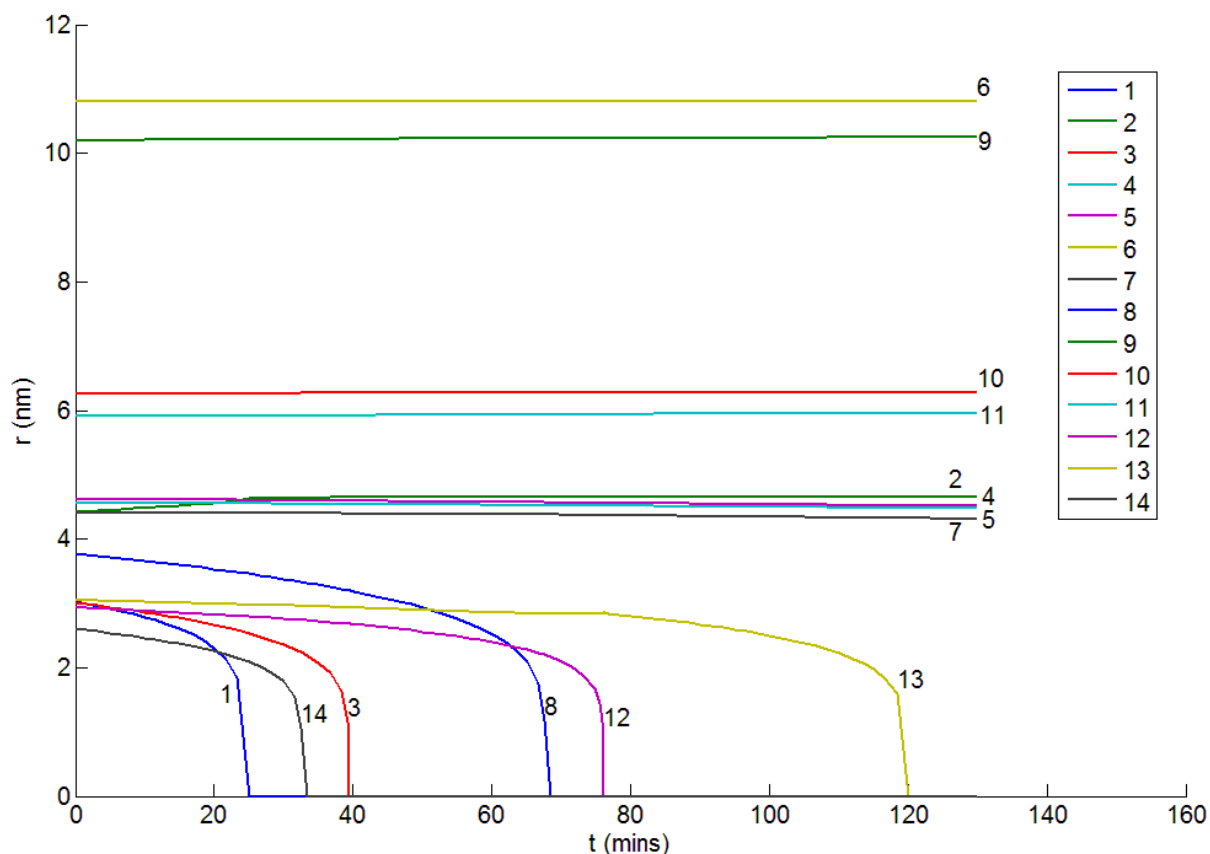


Figure 5.17: Diffusion limited local correlation assumption used with $D \cdot E_{\text{Tot}} = 453.50 \pm 3.02 \text{ kJ/mol}$

The diffusion controlled model appears to describe the decay of particle 1 more effectively than the interface controlled model, with a non size ordered decay observed experimentally. However, the decay of particle 8 is poorly described. As the descriptions of some regions are improved whilst others are not, there is obviously some inhomogeneity required in the modelling parameters. This suggests effects induced by the support or individual particle shape/crystallinity are contributing to the ripening.

As observed for the Cu/Si₃N₄ system used in section 5.3, particle decay occurs within tens of minutes of observation. The previously described H₂ dependency of OR is further investigated in the following section.

5.6.3. Cu/C at 500°C in HV

Observation of individual Cu particles at 500°C in HV, Figure 5.18, shows extinction of particles 4 and 8, with significant size changes to particles 1, 2, 7 and 12. Previous HV observations in section 5.6.1 showed no detectable change in particle size, suggesting that surface support and gas interactions have a substantial effect on E_{Tot} .

Determining E_{Tot} and applying the WG-type models would provide an inaccurate comparison with Cu/C at 500°C in H₂ (section 5.6.2), as too few particle decays are observed to accurately

fit the HV experimental data. Thus, PSDs have been used in Figure 5.19 to show the similarity of the initial distributions (in H₂ $\langle r \rangle = 4.77\text{nm}$, in HV $\langle r \rangle = 5\text{nm}$) and therefore discounting the particle size range as the driving force for increased Ostwald Ripening. After 190 mins in HV, $\langle r \rangle$ has increased to 5.77nm, reflecting the extinction of smaller particles such as 4 and 8. The comparable result in H₂ after 120 mins has not been fitted, due to the large associated error. It is probable that with a larger sample size an LSW distribution may be obtained.

The difference observed in the experimental PSDs with and without H₂ supports the previous conclusion that H₂ reduces the diffusion and/or detachment energy. However, the large difference in the values of E_{Tot} for the two systems suggest the support also plays a role, inhibiting Ostwald Ripening in the case of Si₃N₄ and advancing it in C. This is further explored by using a model system to represent an industrially relevant catalyst in the next section.

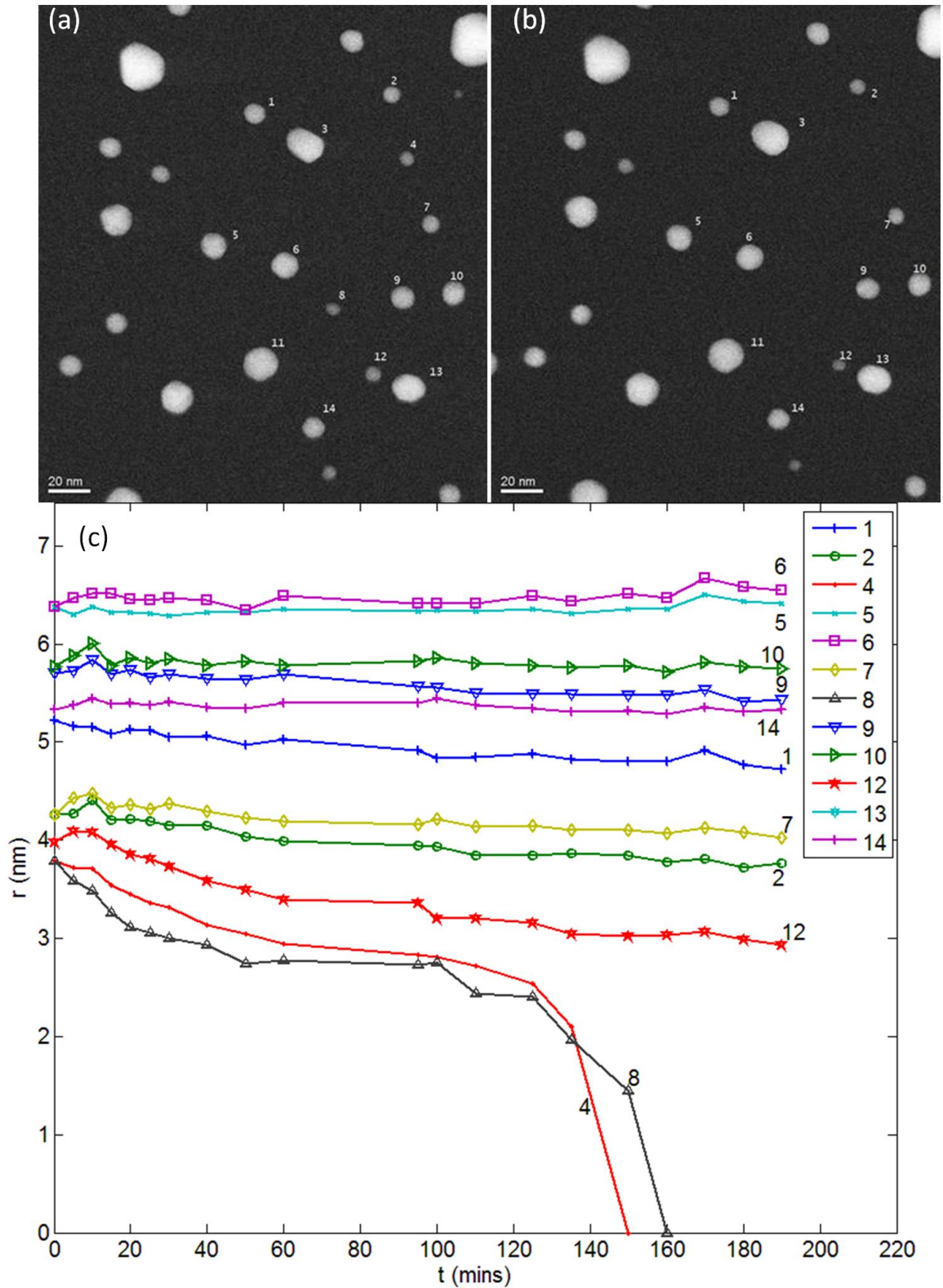


Figure 5.18: (a) Particles at $t=0$ mins, at 500°C in HV, (b) $t=190$ mins, (c) individual particle radii tracking, showing extinction of particles 4 and 8.

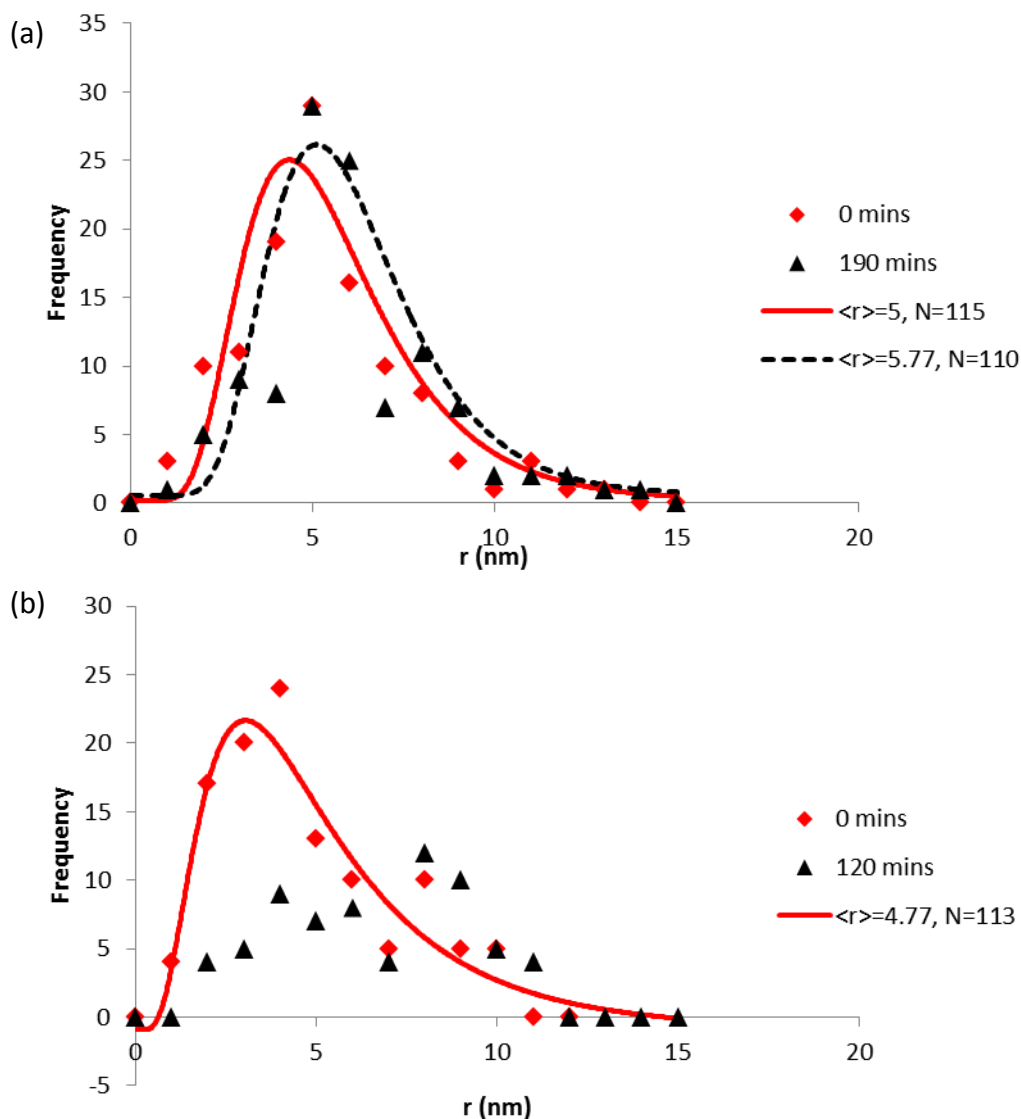


Figure 5.19: (a) 500°C, HV, PSDs with lognormal fits applied (b) 500°C, H₂, PSDs with lognormal fit applied to $t=0$ mins. $t=120$ mins may be LSW-type or a double peak.

5.6.4. Cu/Al₂O₃ at 500°C in H₂ and HV

The Cu/ZnO/Al₂O₃ catalyst system is an extremely important industrial system typically used for synthesising H₂ for CO₂ or CO mixtures [99, 114]. To provide a simplified model system for study, an 8nm film of Al was deposited onto a Si₃N₄ MEMS chip. This was heated at 570°C for 1 hour in 5mBar air to produce α -Al₂O₃ [170-173] (Figure 5.20). The form of the surface appears to be mostly amorphous, but with large 50-150nm diameter crystals present. Previous work has discussed how crystals develop at the oxide-metal interface and then amorphous alumina is gradually transformed to a crystalline form as the oxidation temperature is increased [170-173].

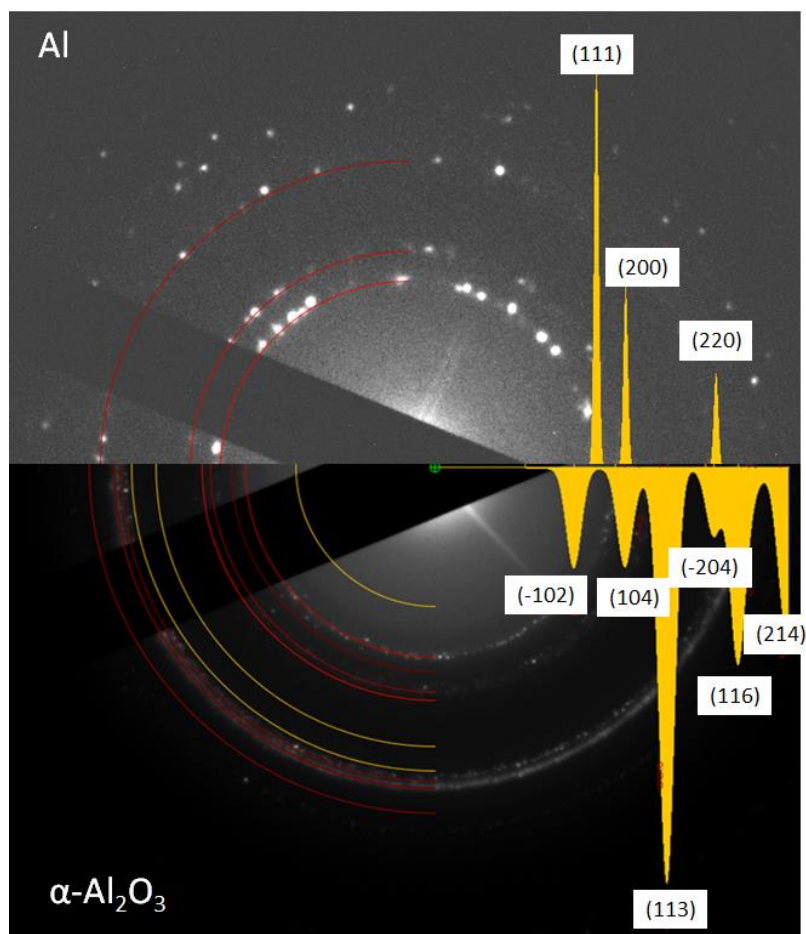


Figure 5.20: Production of model α - Al_2O_3 system by heating an 8nm thick Al film heated at 570°C for 1 hour in 5mBar air. SADPs were taken with a camera length of 30cm.

A 0.7nm film of Copper was then sputtered onto the model Al_2O_3 film. Heating the Cu film using the MEMS heating holder at 500°C for 2 minutes produced particle radii of 10-20nm. These particle sizes (using the same experimental conditions) were considerably larger than those produced on C and Si_3N_4 films.

From Figure 5.21, the average particle size percentage change over 150 minutes at 500°C , HV is 1.88%. There are no particle decays observed during this period. This could be credited as a function of the altered support or particle size, however when 3Pa H_2 gas is introduced the particle size changes over a smaller time period (see Figure 5.22).

The sintering of nanoparticles in H_2 appears to proceed by a combination of OR and PMC. These mechanisms have previously been observed simultaneously [146, 148, 174, 175]. Other interesting effects such as inverse Ostwald Ripening and particle creation and growth were also intermittently seen on the sample [146, 148, 174, 175]. It is believed that these are functions of the support inhomogeneity and thus could not be fully investigated in this experiment.

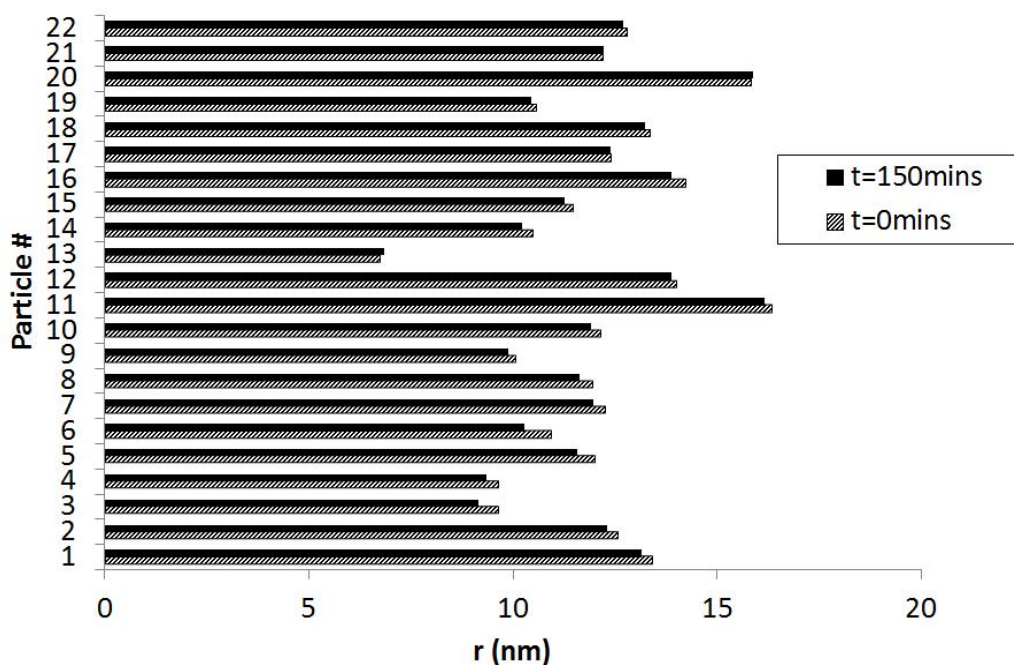
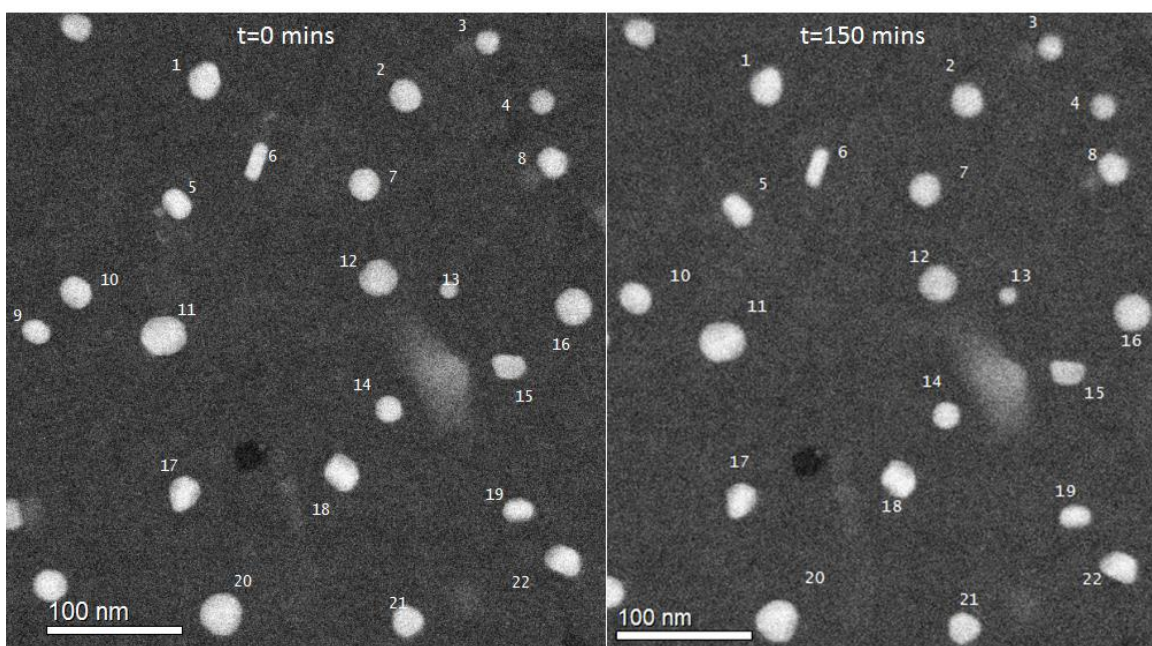


Figure 5.21: Comparison of particle size change of Cu/Al₂O₃ in HV at 500°C at t=0 minutes and t=150 minutes.

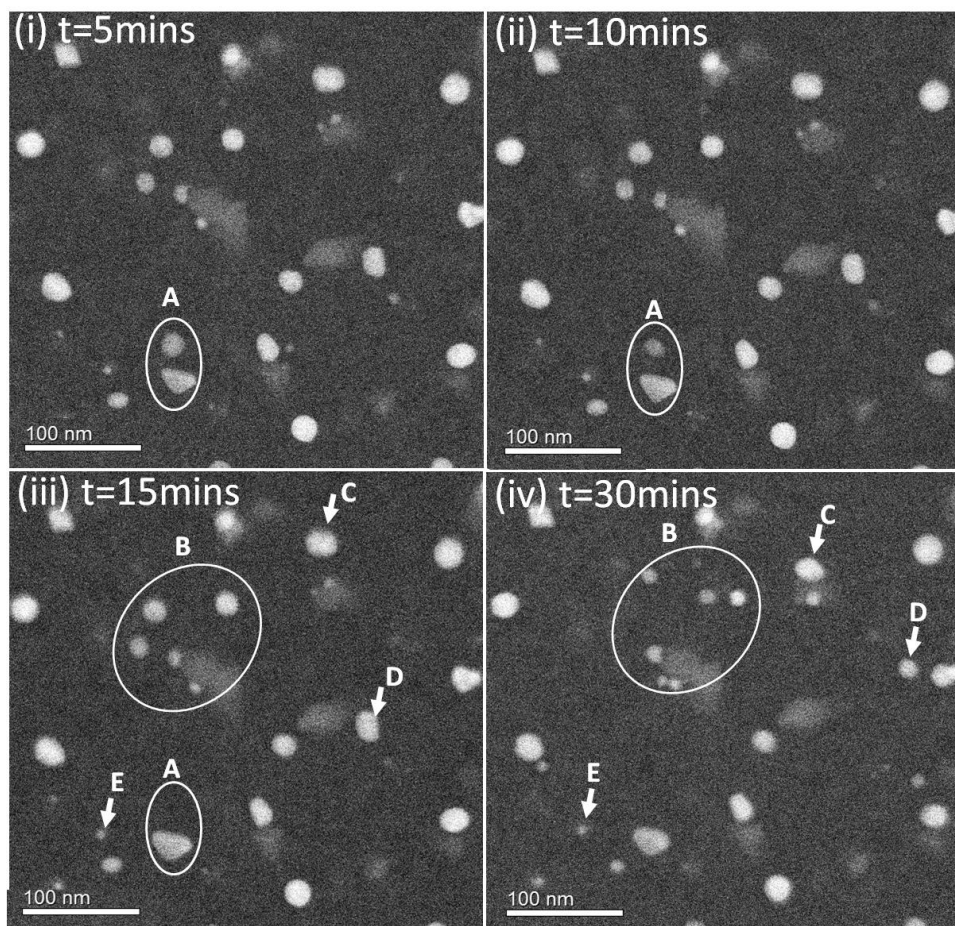


Figure 5.22: Cu on amorphous Al_2O_3 in H_2 at 500°C . The Ostwald ripening process is observed in the region labelled A, whereas PMC strongly contributes in regions B-E. From TEM and AFM (Atomic Force Microscope) measurements (Figure 5.23), the grey regions on the substrate are believed to be crystalline $\alpha\text{-Al}_2\text{O}_3$.

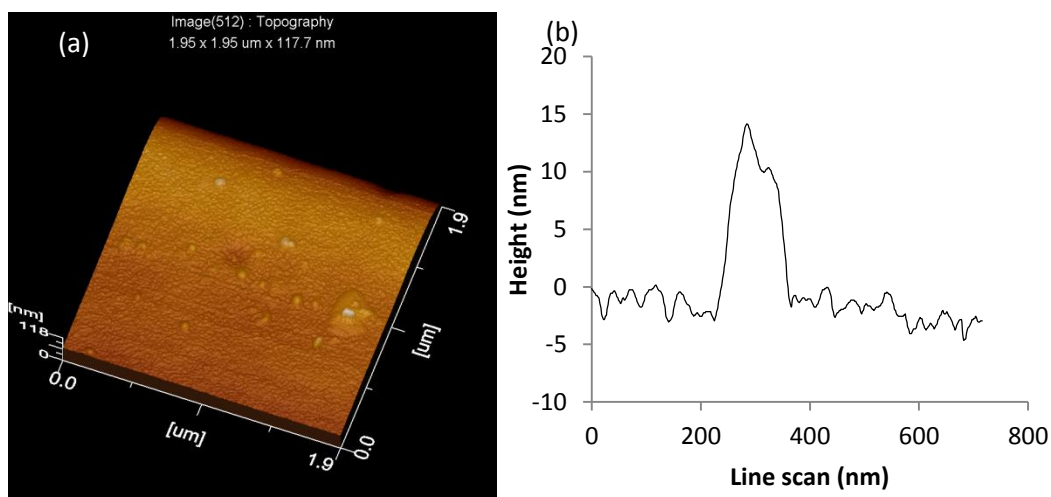


Figure 5.23: (a) AFM (Atomic Force Microscope) scan of Al_2O_3 film. TEM observations indicate the 15nm peak observed in (b), and the raised regions in (a), are believed to be $\alpha\text{-Al}_2\text{O}_3$ crystals. Previous work has indicated that these crystals originate at the oxide metal interface and grow with increased temperature in air. The amorphous Al_2O_3 surrounding the crystals has an RMS surface roughness of 4.62nm over a $700\text{nm} \times 700\text{nm}$ area (the experimental area shown in Figure 5.21 and Figure 5.22). Any $700\text{nm} \times 700\text{nm}$ region produced using this method will have approximately 2-3 crystalline peaks within it.

Particle stability appears to be enhanced by attachment to the crystalline $\alpha\text{-Al}_2\text{O}_3$ regions indicated by the light grey areas in Figure 5.22. Particle C in Figure 5.22 is seen to migrate and become trapped on the edge of one of these regions, whilst small (r less than 5nm) particles are only seen to exist trapped on the side of the crystalline areas.

The stability of crystals is also affected by nanoparticle shape. Facetted cubic or trigonal nanoparticles appear to grow at the expense of larger rounder nanoparticles (Figure 5.24). This may be an example of Ostwald Ripening occurring inversely [158, 176-178], where the net movement of mass is from larger to smaller nanoparticles. Cu nanocubes are also formed on C in H_2 when the temperature is dropped from 500°C to 20°C over the course of 10 seconds. By iteratively introducing H_2 , dropping the temperature and moving to another area (to ensure beam effects were not influencing the result) nanocubes can be created and destroyed. This process is not observed under HV conditions.

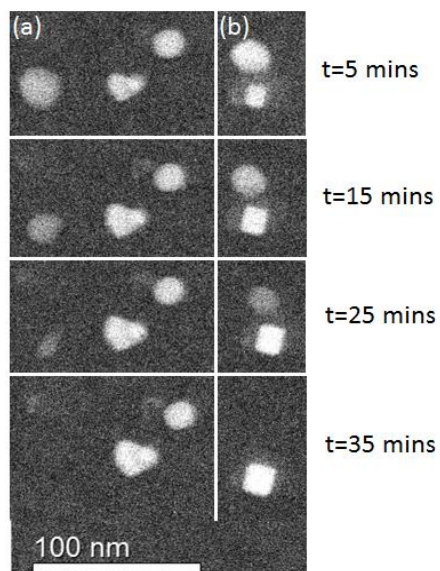


Figure 5.24: Observation of inverse Ostwald Ripening of Cu nanoparticles on Al_2O_3 in 3Pa H_2 at 500°C . In (a), the more facetted trigonal particle grows at the expense of the larger rounded particle on the left hand side. A similar observation is made in (b), where a nanocube forms and then grows at the expense of a rounded particle. The more facetted particles have greater thermodynamic stability [179] and therefore grow instead of the larger round particles.

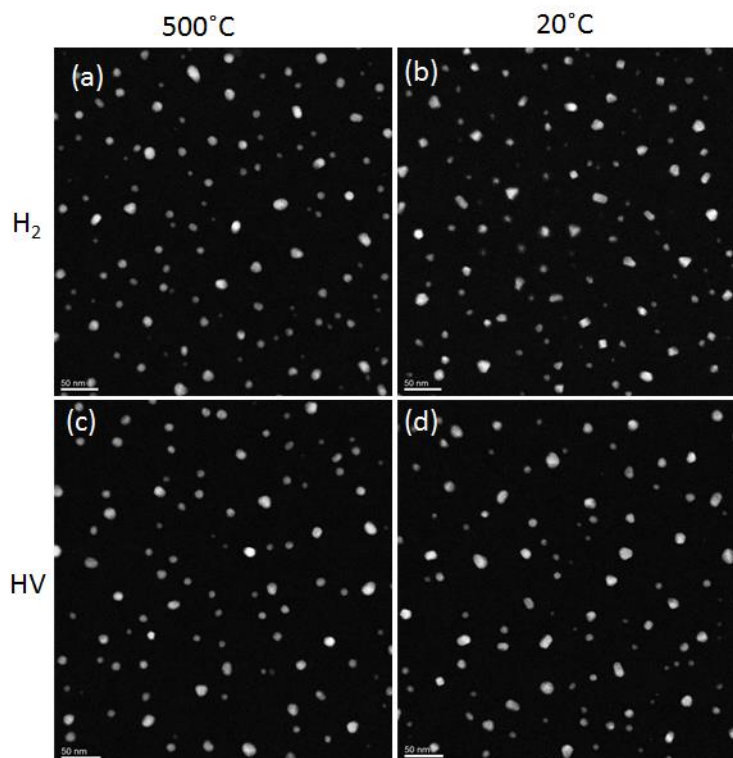


Figure 5.25: Reduction of the temperature over 10s from (a,c) 500°C to (b,d) 20°C in 3Pa H₂ environment (a,b) and HV environment (c,d) for a Cu/C sample. Observation of regions that had not been exposed to the beam shows a change to more faceted particles, with cubes and trigonal particles a common feature under H₂. No obvious change was observed after quenching in HV conditions.

It has been previously suggested that slow growth of nanoparticles allows for atoms to move to thermodynamically favourable positions [179, 180]. For FCC metals, such as Cu, it is suggested by Xia *et al.* [179] that the most thermodynamically stable shape for single crystals is a cuboctahedron. Under HV conditions, Cu/C Ostwald Ripening occurs at a slow rate (section 5.6.3). The application of H₂ likely increases the single atom population on the C support. As the temperature is rapidly dropped, the nanoparticle shape stability changes and the supply of single atoms decreases. It is likely that these factors contribute to the prevalence of nanocubes observed in Figure 5.25. The intermittent observation of nanocubes of Cu on the Al₂O₃ sample is potentially a function of the inhomogeneous nature of the support and is therefore dependent on single atom supply effects, combined with the nature of the support in the local region.

In conclusion, a thin film of amorphous Al₂O₃ with 50-150nm crystalline regions has been produced after heating an 8nm Al thin film on a Si₃N₄ MEMS chip at 570°C in 5.5mBar of air. Ostwald Ripening of Cu on Al₂O₃ occurs under H₂, but as with C and Si₃N₄, is inhibited under HV conditions. PMC is observed to occur concurrently with Ostwald Ripening at 500°C, however

due to the support inhomogeneity, it is difficult to quantify the sintering process via comparison with kinetic models.

So far in this chapter the effect of support and gas environment has been investigated with several different Cu systems. However, further theoretical understanding of the role of H₂ in the enhancement of Ostwald Ripening is difficult without knowledge of the atomic processes occurring.

Due to the Z dependence of HAADF-STEM imaging, it is difficult to image single atoms of lighter elements such as Cu, especially in gas on C-films greater than 4nm in thickness. However, an understanding of the atomic processes can be obtained by deducing whether the Ostwald Ripening is diffusion or interface limited. This can then provide information on why H₂ would enhance the process.

The following sections will examine Ostwald Ripening of Cu/C in H₂ in the temperature range from 400-550°C. Varying the experimental temperature changes the proportion of atoms that can surpass either the activation or diffusion energy barriers. Both the interface and diffusion limited cases depend exponentially on the temperature but have different activation barriers. If the temperature range is large enough, a shift between the two limits will be observed.

5.7. The Effect of Temperature on Ostwald Ripening

5.7.1. Cu/C at 550°C in H₂

The Cu systems used in this study are known to undergo PMC at higher temperatures (section 5.2). Besides the theoretical implication of equations 5.1 and 5.2 that high T will increase the ripening rate due to the assumed Gaussian dependence of the energy barriers, no further understanding of the effect of temperature has been obtained in this work. Chen and Ruckenstein [148] have previously discussed that sintering by atomic migration will occur only when the temperature is sufficient to break the metallic bonds within particles [71]. Due to variations in the support, particle morphology and bond strength between samples, no generalised model to predict the OR limiting mechanism has been produced. However, by altering the temperature the probability of adatom emission, diffusion and metal-support interactions will change and thus modify the OR limits.

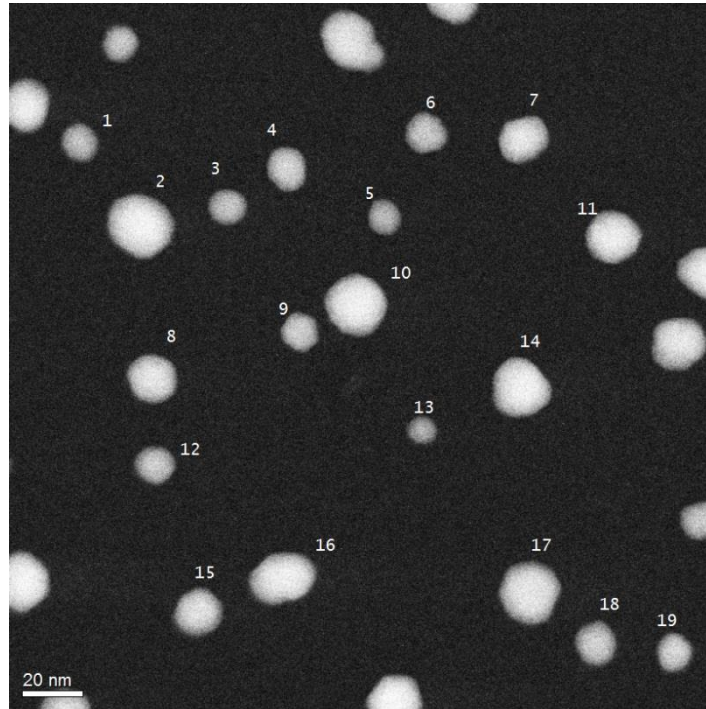


Figure 5.26: Map of experimental area used for observations of Cu/C at 550°C in H₂.

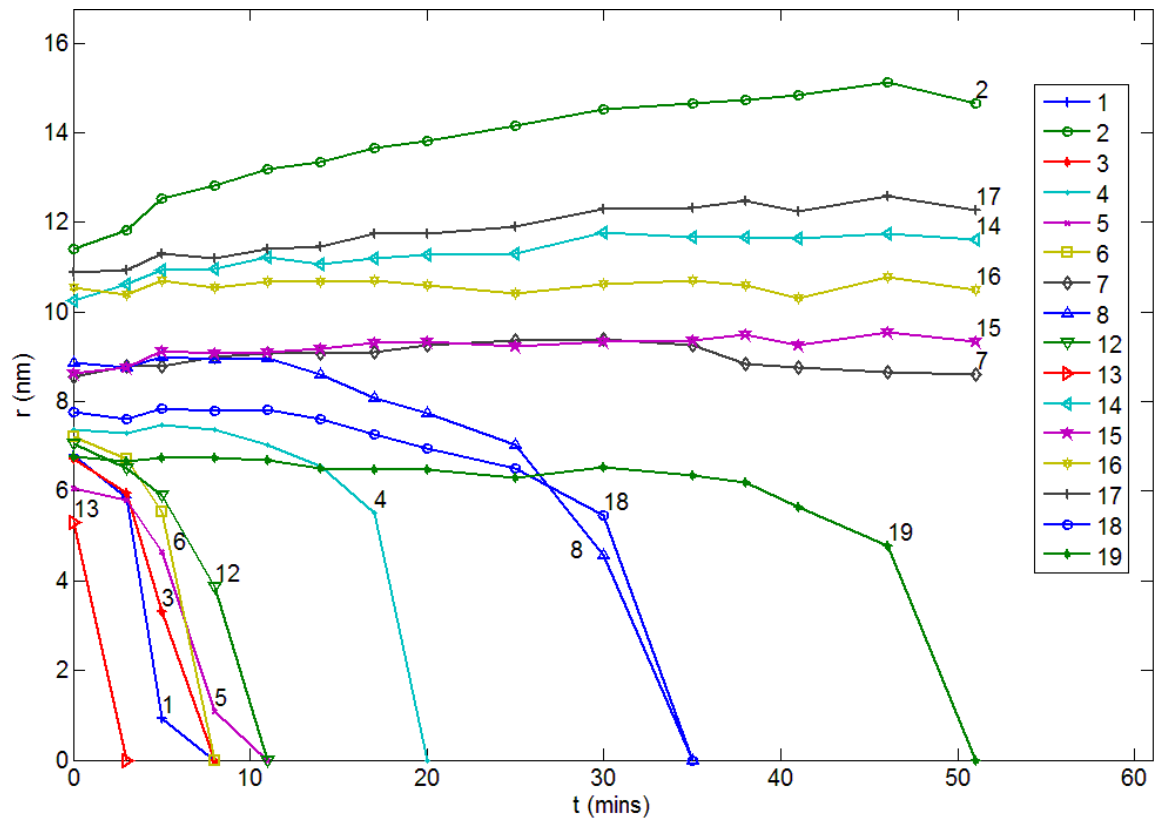


Figure 5.27: Experimental particle radii for Cu/C system at 550°C in H₂. Error in r is 0.3nm, calculated using the method developed in section 5.2.1. Particles 9, 10 and 11 are excluded due to migration being observed.

In all lower temperature experiments, OR has exclusively been detected as the sintering mechanism. Here, particle migration occurs for particles 9, 10 and 11, with particles 9 and 10 coalescing. The rate of Ostwald Ripening is enhanced by increasing the temperature to 550°C. Despite a similar size range to other Cu/C systems ($\sigma_{400}=2.06\text{nm}$, $\sigma_{500}=2.59\text{nm}$, $\sigma_{550}=1.83\text{nm}$), there is greater than a 50% particle extinction rate in 70 minutes, compared to 13% at 400°C and 29% at 500°C.

The experimental data shows an increase in size of 28% for particle 2, 13.5% for particle 14 and 12.5% for particle 17. The largest particles are observed to gain mass from the smallest. This is in contrast to the previous observation in section 5.3 where the assumption that particles are hemispherical meant that the change in radius was undetectable from the measurement error. In this system the net mass decrease is 8003nm^3 with a net mass gain of 3851nm^3 . There is therefore some lost mass, possibly to particles outside the experimental area or single atoms still trapped on the support. The assumption of hemispherical particles is also likely to be particle size dependent, and thus there may be an inherent overestimation in the mass decrease. Simonsen *et al.* [45] have previously shown that Pt/ Al_2O_3 in O_2 has a height:diameter ratio of 1 at smaller sizes (diameters approximately 2nm), with the ratio dropping to 0.8 for larger (diameter approximately 8nm) particles. This relationship is a function of support, gas environment and material. Previous studies on Cu have shown changes in morphology and wettability in different gas environments [79].

Excluding surrounding particles and assuming an equal distribution of the lost mass between the non-extinct particles, means each particle increases in size by 1334nm^3 . This provides an increase in radius of the particles 2, 14 and 17 of 18.7% (2.13nm), 24.5% (2.5nm) and 21% (2.3nm) respectively. The assumption of an equal share of the mass emitted by decaying particles is clearly incorrect, as the change in radius of particle 2 is underestimated, compared to the overestimate for particle 14 and 17. However, the estimated radius changes are an order of magnitude greater than the measurement error of 0.3nm. This indicates that the lack of a size increase in section 5.3 is a detectability issue due to the two dimensional projection observed.

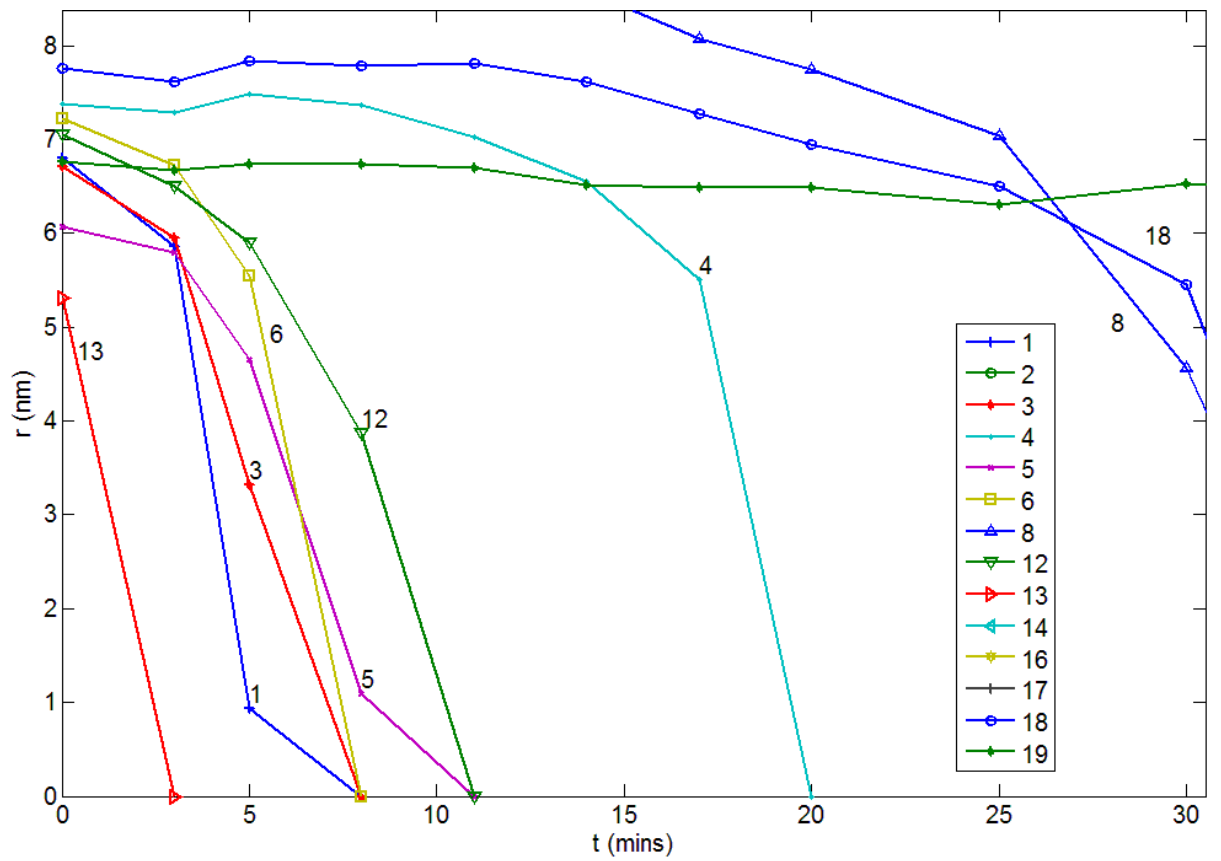


Figure 5.28: Magnified area of Figure 5.27 in the $r=0-8\text{nm}$ regions.

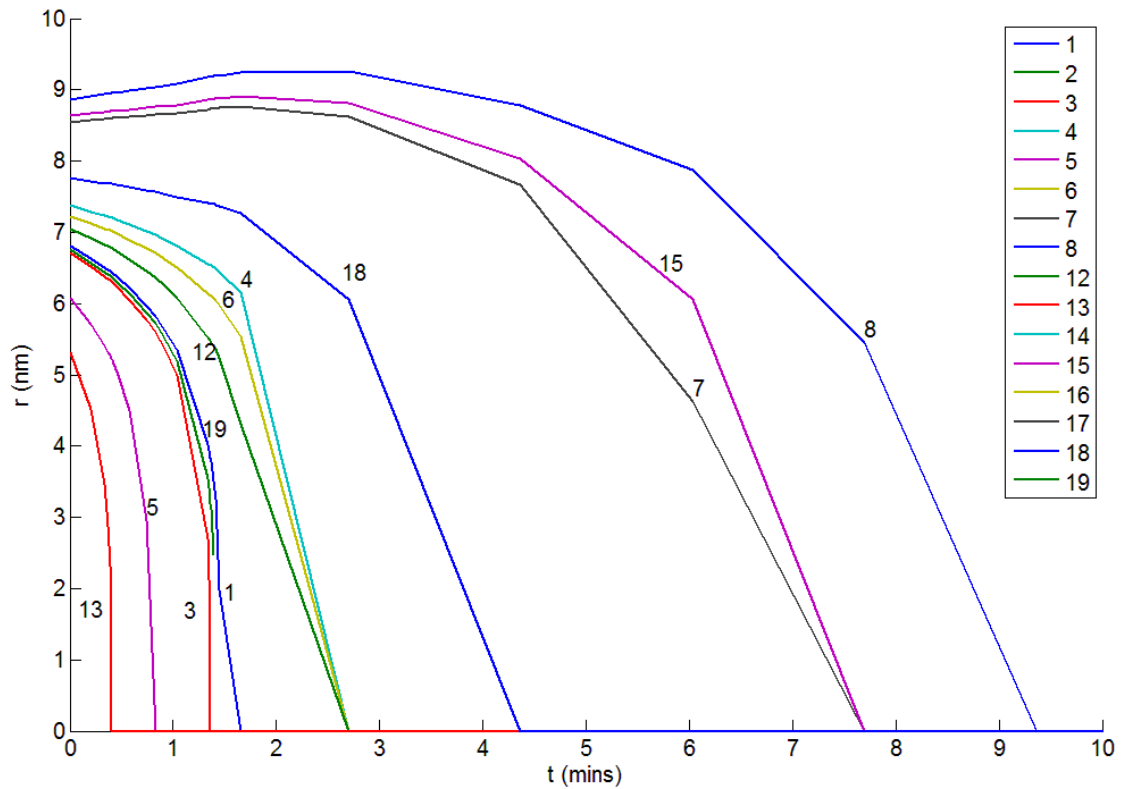


Figure 5.29: Interface controlled mean field model applied using $E_{\text{Tot}}=177.83\text{kJ/mol}$ with an error of 3.44kJ/mol . Particles displayed have an initial r less than 9nm .

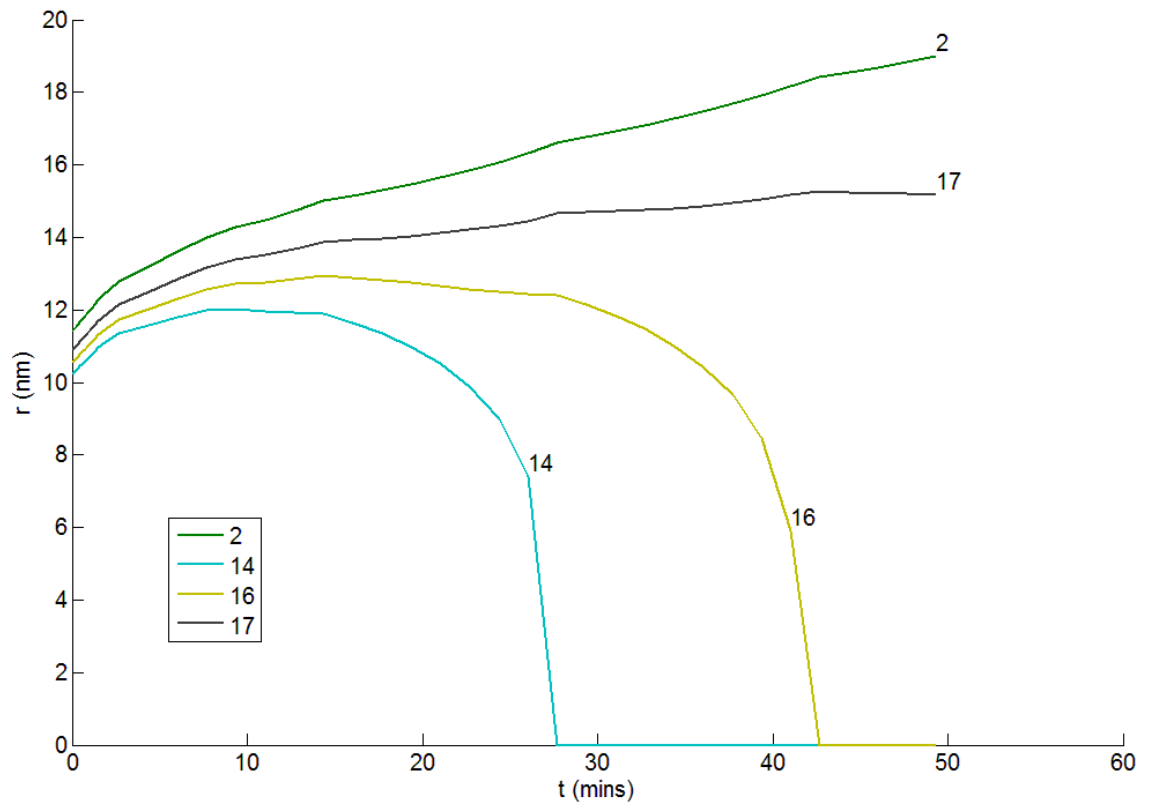


Figure 5.30: Interface controlled mean field model applied using $E_{Tot}=177.83\text{kJ/mol}$ with an error of 3.44kJ/mol . Particles displayed have an initial r greater than 9nm.

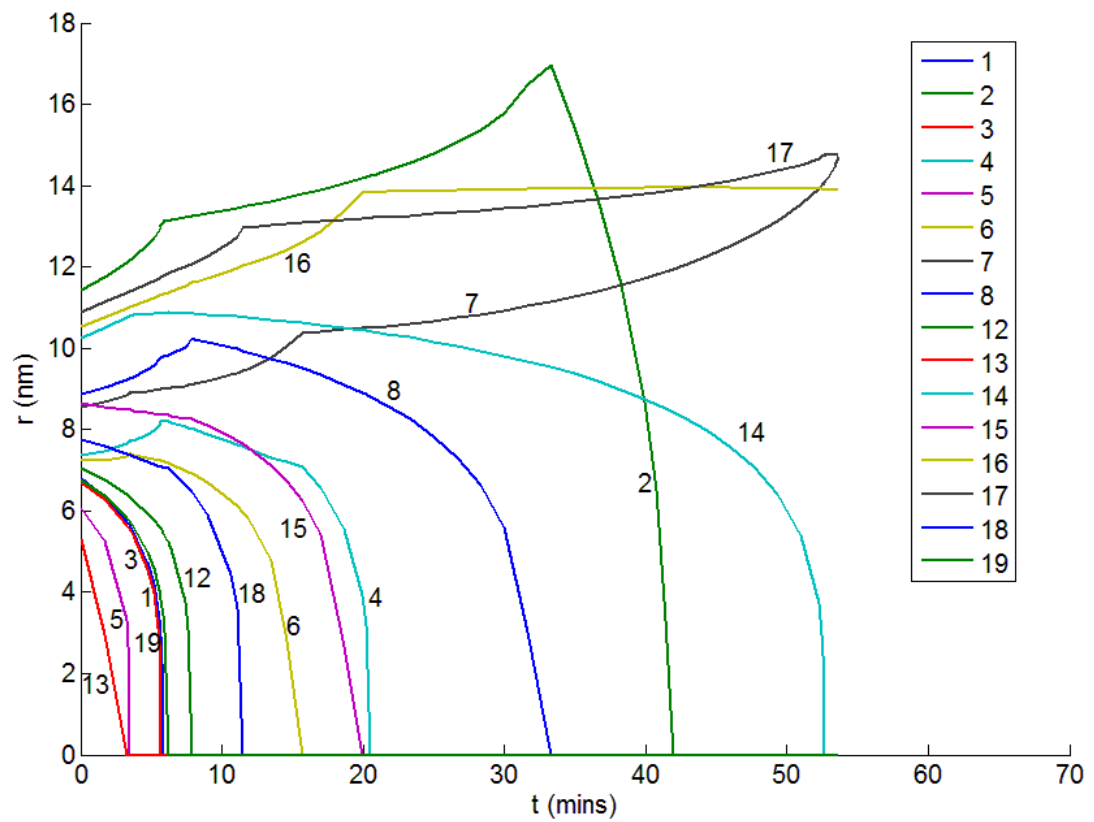


Figure 5.31: Interface controlled local correlation model applied using $E_{Tot}=184.0\text{kJ/mol}$ with an error of 4.47kJ/mol .

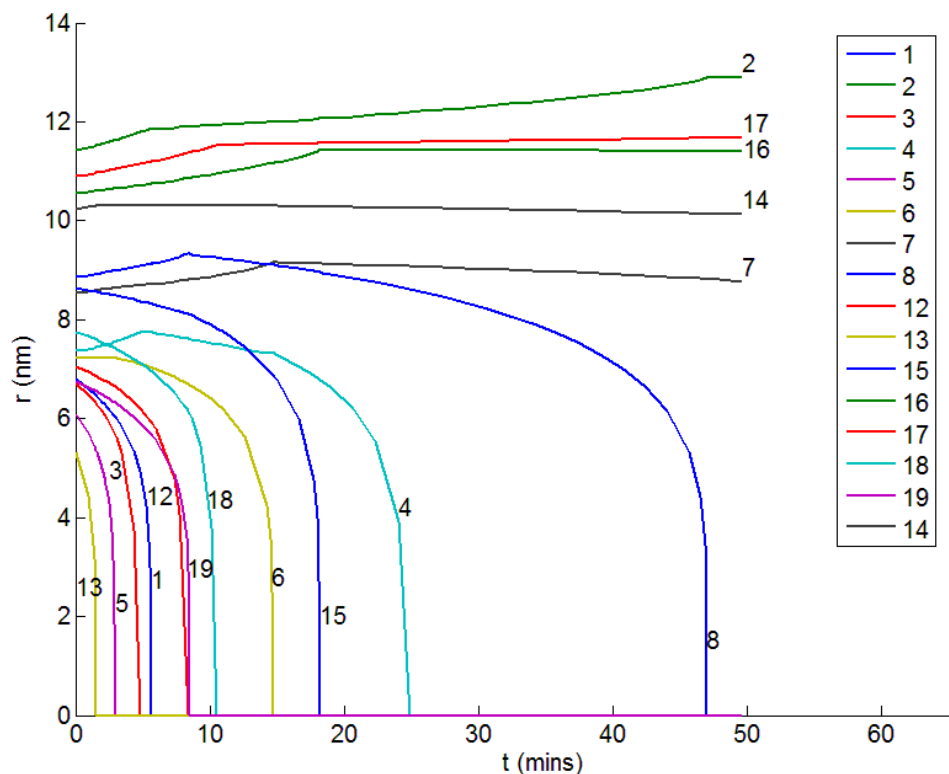


Figure 5.32: Diffusion controlled local correlation model applied using $D \cdot E_{\text{Tot}} = 432.95 \pm 1.55 \text{ kJ/mol}$

The growth of particles 2, 14 and 17 is not represented well by the mean field model (Figure 5.29 and Figure 5.30), with 2 and 17 increasing in size, whilst 14 becomes extinct within the experimental time frame. In the local interface limited model (Figure 5.31), a similar pattern is repeated, but with the addition of an unphysical decay of particle 2 after 45 minutes. This is not observed in the local diffusion limited model (Figure 5.32), as the mass change is governed by a pairwise exchange between particles, as opposed to a local concentration. This means that the greater distance between particles in the diffusion limited model damps the atom exchange. In the interface model particle 2 exchanges solely with the combined mass of particles 9 and 10 (not shown here as they coalesce during imaging) with no damping and therefore quickly decreases in size.

For smaller particles the decay times of particles 1, 5, 6, 8 and 19 are not size ordered. Out of these particles, the only outlier is particle 19, which exceeds the extinction times of similarly sized particles by almost 50 minutes. This is reflected in the diffusion controlled model, where particle 19 exceeds particle 12's extinction. However, size ordering is apparent in both the interface mean field and local interface controlled models.

Particle 8 is well represented by both the local interface and diffusion controlled models, but poorly represented in a mean field model. This is associated with the proximity to large nanoparticles such as 2 and 9/10, which increases the local adatom concentration and cause a faster decay time for particle 8 in comparison to similarly sized particles such as 7. However, the longevity of particle 15 is not well represented in these models, when compared to the experimental data.

None of the 3 models investigated represent the experimental results well, however the local diffusion controlled model appears to provide some improvement. This is corroborated by examining the Levenshtein distance for the decay order. The number of exchanges (weight of 1) and deletions/insertions (weight of 2) are counted so that the theoretical order of particle decay matches that obtained experimentally. For the interface controlled mean field and local concentration models, the Levenshtein distance is 11, whereas it is 9 for the local diffusion controlled model.

5.7.2. Cu/C at 400°C in H₂

Continuation of OR temperature investigations is undertaken by observation of Cu/C at 400°C in 3Pa of H₂ (Figure 5.33 and Figure 5.34). The experimental decay of particles is close to size ordered, however there is a 60 minute difference in the $t(r=0)$ of particles 1, 4 and 15, despite being approximately the same sizes. The decay order is not replicated by any of the 3 models implemented (Figure 5.35, Figure 5.36 and Figure 5.37), however the time spread is best represented in the local diffusion or interface controlled models where the decay times occur over a 40-55 minute period. The overall Ostwald Ripening rate is much slower than that observed at 550°C and this is reflected in the lack of an increase in the observable size of the largest particles.

Observations of Cu/C at different temperatures suggest that improvements in the decay ordering can be obtained with different kinetic models. This allows for an understanding of the ripening limiting factor and the following section will explore this further.

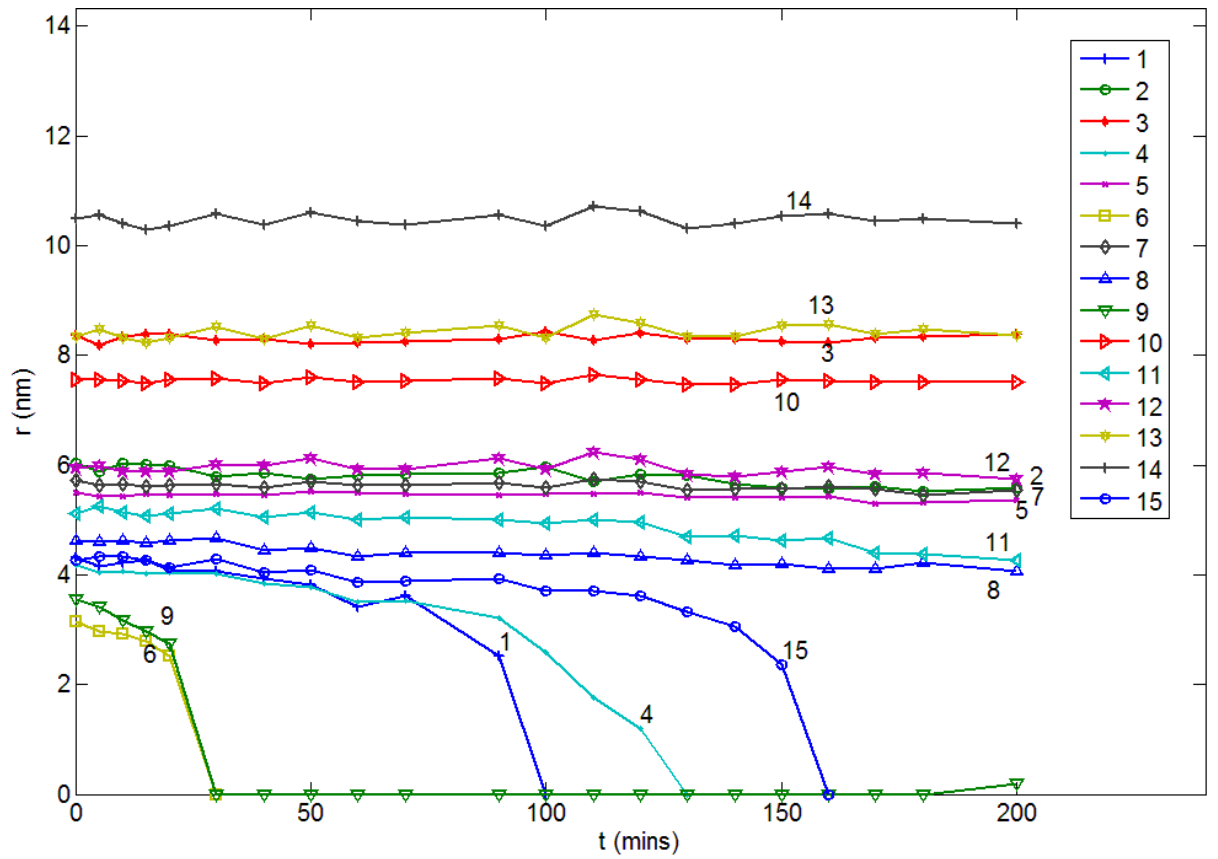


Figure 5.33: Experimental particle radii for Cu/C system at 400°C in H₂. Error is 0.12nm

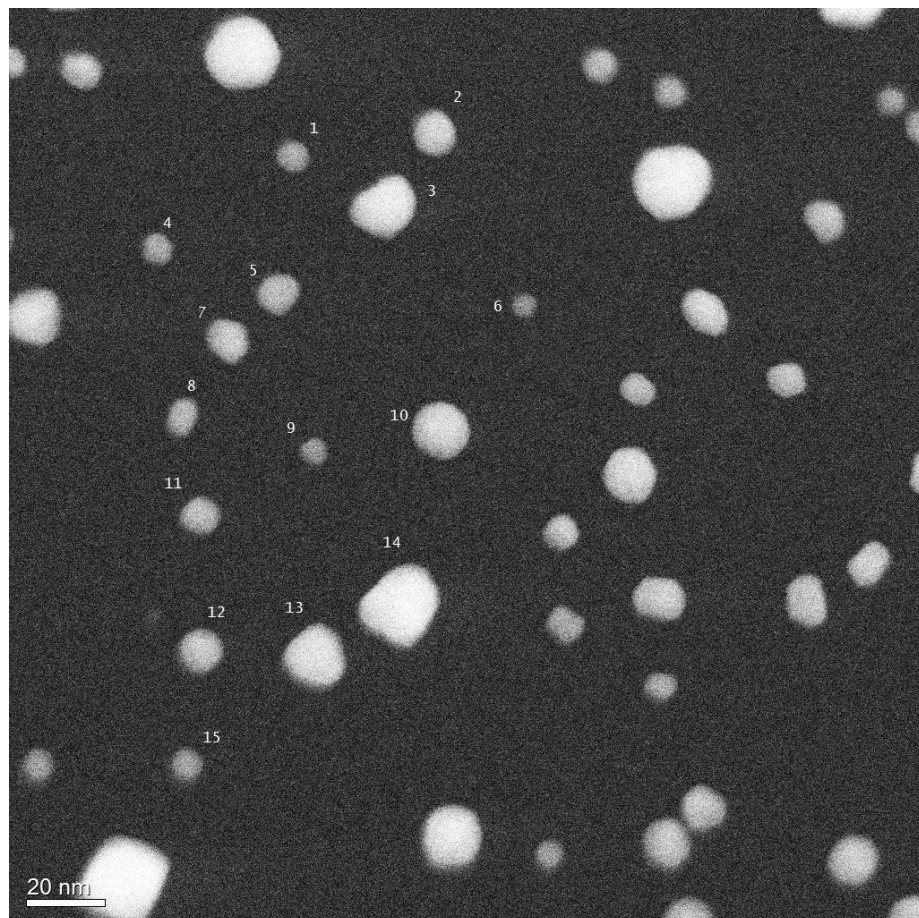


Figure 5.34: Map of experimental area used for observations of Cu/C at 400°C in H₂.

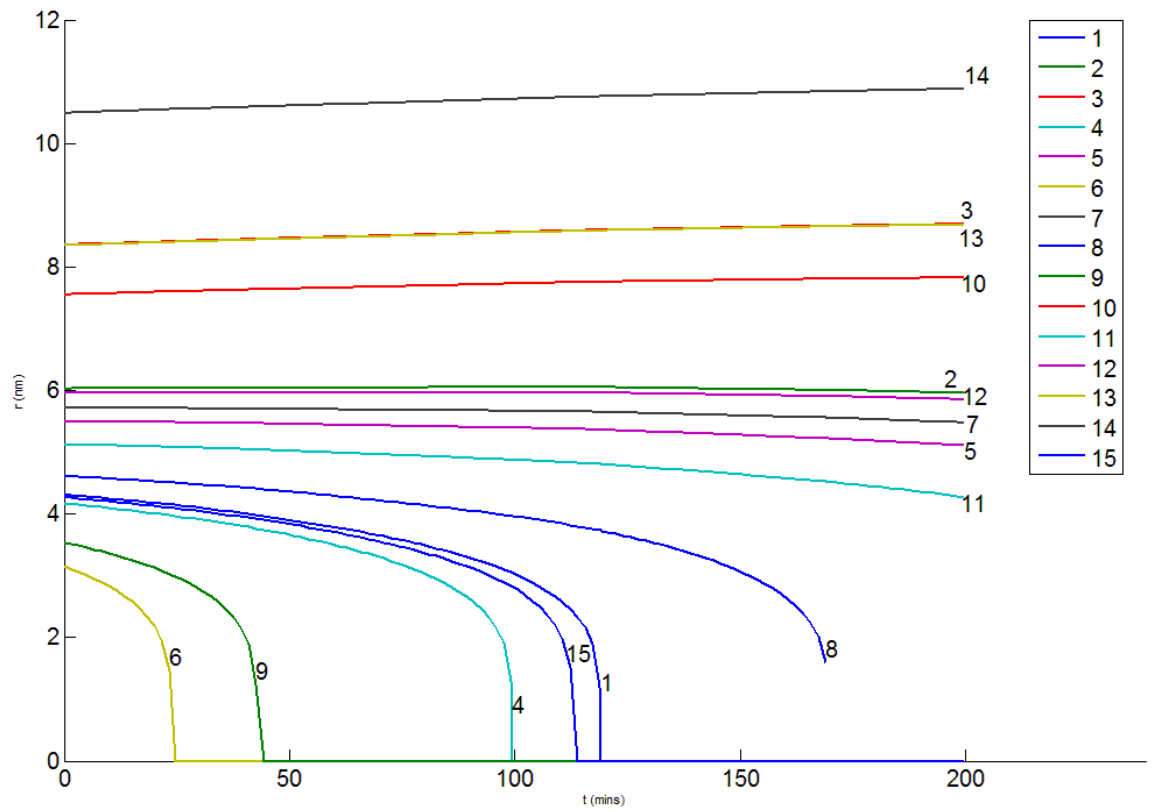


Figure 5.35: Interface controlled mean field model applied using $E_{Tot}=221.23\pm 2.01\text{kJ/mol}$.

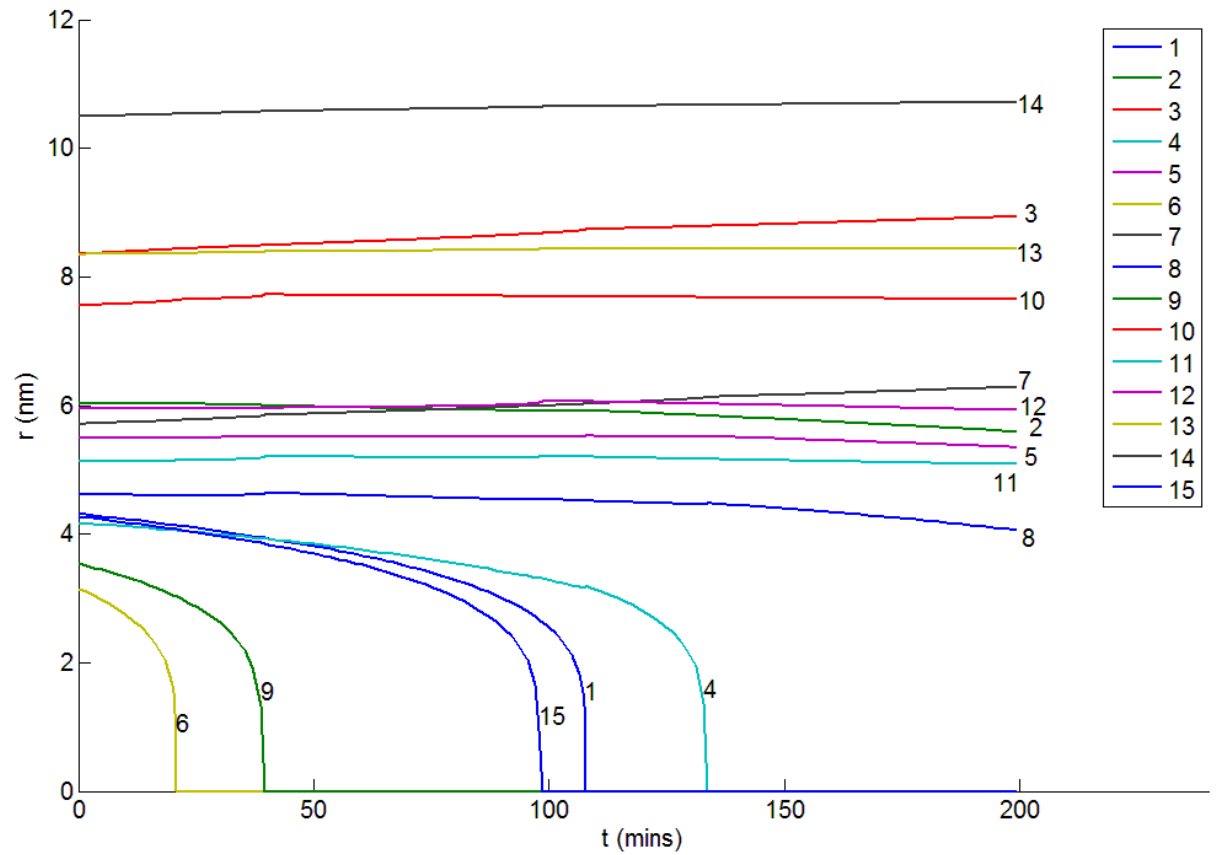


Figure 5.36: Interface controlled local correlation model applied using $E_{Tot}=216.58\pm 1.96\text{kJ/mol}$.

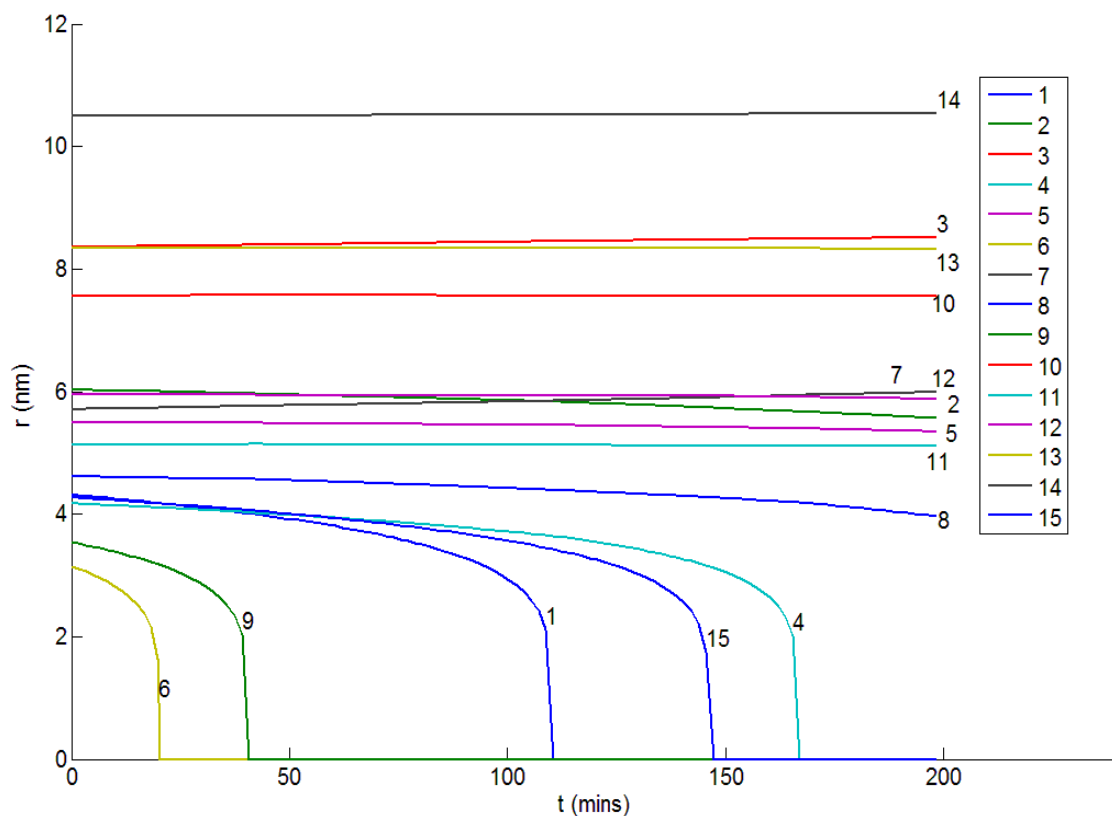


Figure 5.37: Diffusion controlled local correlation model applied using $D \cdot E_{\text{Tot}} = 387.00 \pm 2.16 \text{ kJ/mol}$.

5.8. Interface and Diffusion Limits

As previously discussed in section 5.1, Ostwald Ripening may be diffusion or interface limited. Using the approach of Wynblatt-Gjostein [43], a power law may be determined from their OR equation on an average particle size basis (equations 5.10 and 5.11). As with other treatments within Wynblatt-Gjostein's work, the Gibbs-Thomson equation is only taken in its first order form. The exponential terms mean the OR equation cannot be directly integrated, leading to the limitations discussed in section 5.1. The average size of all nanoparticle in a system $\langle r \rangle$ at time t , and at the start time, $\langle r_0 \rangle$, is related to a rate constant (K_n) encompassing the operating regime, temperature dependence and other physical parameters by:

$$\langle r \rangle^n - \langle r_0 \rangle^n = K_n t \quad 5.10$$

$$n \log \frac{\langle r \rangle}{\langle r_0 \rangle} \approx \log \frac{K_n}{\langle r_0 \rangle^n} + \log t \quad 5.11$$

A similar approach for individual particles has been previously utilised by Morgenstern et al. [62] and McLean et al. [145] (equation 5.12). Normalisation in this case is provided by

referencing to the extinction time, t_0 . However it is normally derived with an $\langle r \rangle$ dependence to allow for application to PSDs [43, 48, 63, 181]. The value of n in the interface limited regime is $1/2$, and $1/3$ for the diffusion limited case. As discussed by Harris [182] the actual value of n is not exact. Figure 5.38 shows two distinct regimes of operations, with Cu/C at 550°C and 500°C operating in a high n regime, and Cu/C at 400°C operating in a low n regime. This suggests that Ostwald Ripening is diffusion limited at lower temperatures and transitions to the interface limited regime as the temperature is increased.

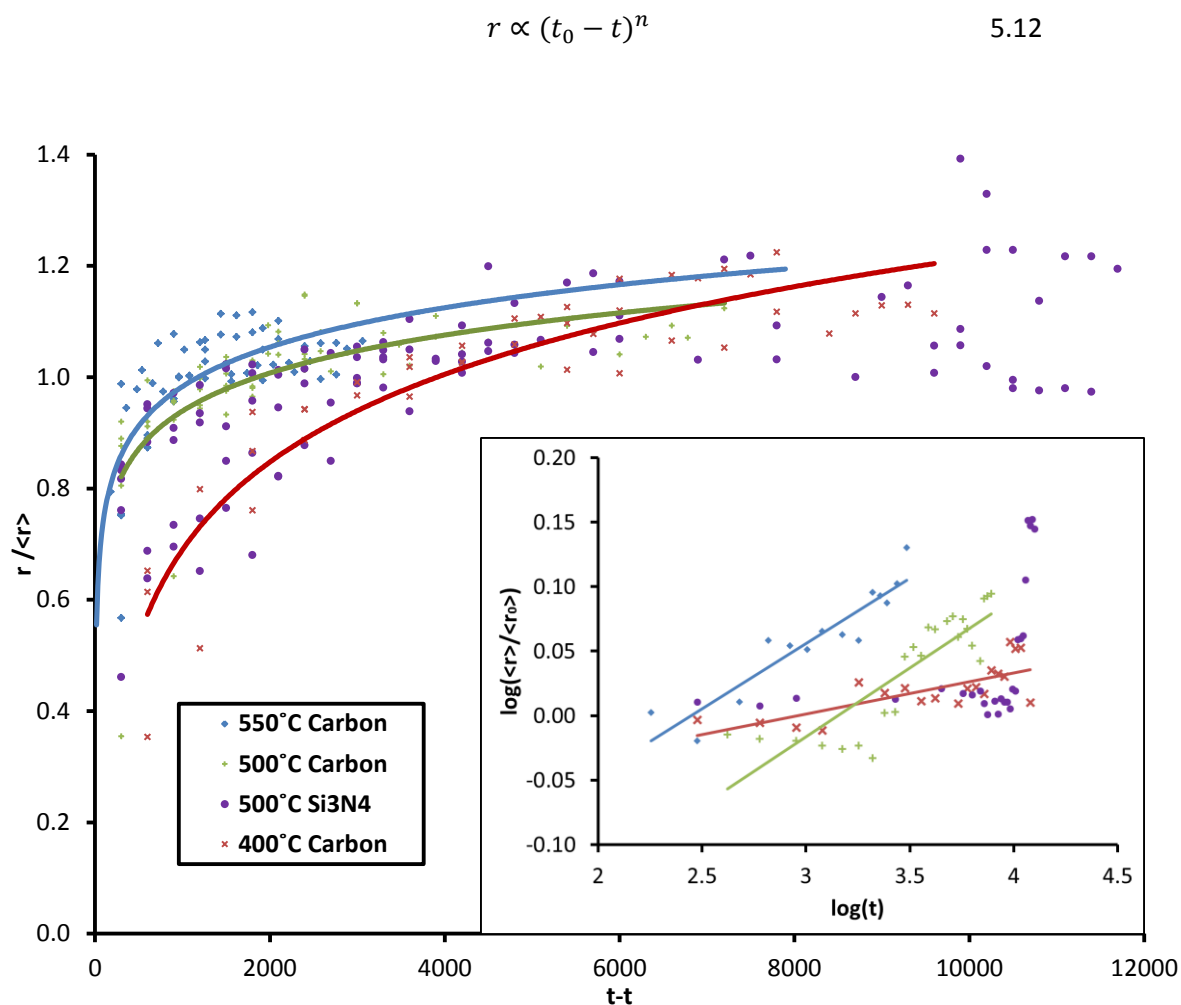


Figure 5.38: r is normalised by dividing by the average individual particle size. All individual particles are then plotted for each different temperature and material used in the previous sections. A power law fit is used as a guide to the eye indicating two operating regimes. Different nanoparticles in the Cu/Si₃N₄ system appear to be operating in both regimes. To obtain values for n , the logarithmic form is plotted (equation 5.11). The values obtained for Cu/Carbon at 550°C , 500°C and 400°C respectively are 0.10, 0.11 and 0.03.

Interestingly, Cu/Si₃N₄ appears to have some particles operating in both the surface and diffusion limited regimes. From Figure 5.39, Si₃N₄ has greater heterogeneity and, on average, a

considerably rougher surface than C-films over the 50x50nm experimental region. It is suggested that the reason for the dual regime operation on Si_3N_4 is a support property.

Measuring the substrate using an AFM (Atomic Force Microscope) an average roughness value can be obtained for the experimental area (50nm x 50nm for C and Si_3N_4 supports, 600nm x 600nm for Al_2O_3). For comparison purposes, the RMS roughness for Al_2O_3 is taken over both the Al_2O_3 experimental area (600nm x 600nm) and also the C and Si_3N_4 experimental area (50nm x 50nm). The average RMS roughness over a 50nm x 50nm area is 0.420nm, 2.59nm and 0.659nm for Carbon, Si_3N_4 and Al_2O_3 respectively. The Al_2O_3 support has ridges of diameter 50-150nm, which are not included in this calculation. Over 600nm x 600nm, the RMS roughness is 4.62nm for Al_2O_3

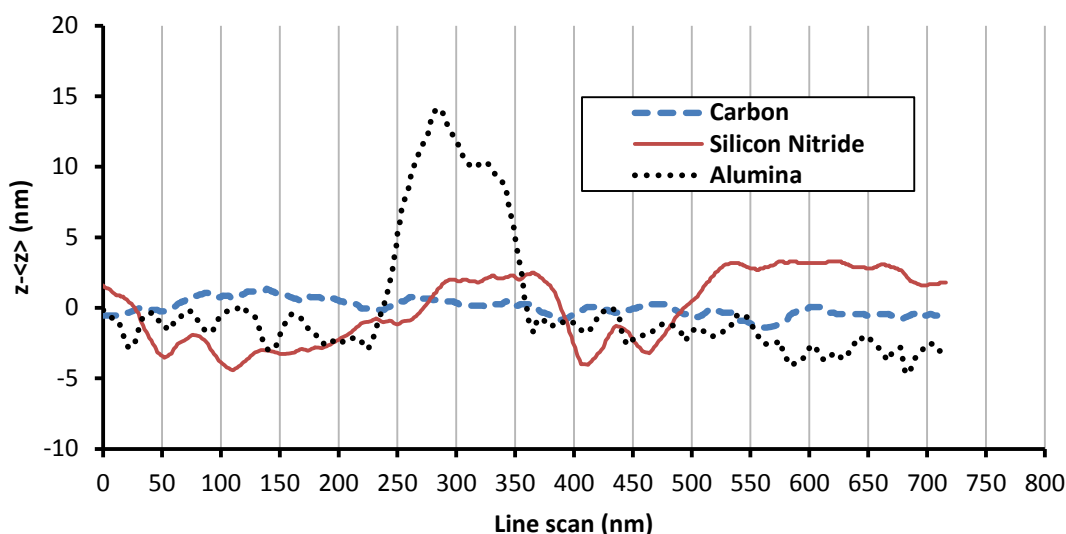


Figure 5.39: AFM linescans of regions on Carbon, Silicon Nitride and Alumina supports. The Alumina linescan is purposefully selected to include an exposed ridge, between 220-370nm. As discussed in section 5.6.4, this is likely a crystalline region. The average RMS roughness over all 50nm x 50nm regions in a $3\mu\text{m} \times 3\mu\text{m}$ scan is 0.420nm, 2.59nm and 0.659nm for Carbon, Si_3N_4 and Al_2O_3 respectively.

5.9. Conclusions

This is the first use of ESTEM to track OR of nanoparticles. This has allowed for the influence of H_2 , temperature and the support to be investigated on the OR rate. With the use of TEM, the phase contrast dependency means smaller nanoparticles are sometimes undetectable on the support. ESTEM confers the advantage that nanoparticles can be tracked until $r=0$.

Using ESTEM individual particle observations of Cu on various supports, OR has been shown to be the dominant sintering mechanism at 500°C in 3Pa of H_2 . Repeating this work in HV conditions demonstrated the same low particle migration, but with reduced transfer of atomic

species, suggesting that H₂ is enhancing the Ostwald Ripening process. This could occur via many different mechanisms such as weakening of Cu-Cu bonds, enhanced diffusion of Cu adatoms or altered wetting behaviour [68]. Adibi [183] also noted enhanced sintering of Pt in higher pressure O₂ environments, suggesting pressure dependence as an area for future study in this system.

Kinetic models have been applied to attempt to understand the rate of change of particle size using both local correlation and mean field assumptions to estimate the surface concentration of single atoms. The models do not fully replicate the non-size ordered extinction times observed experimentally. Modifying γ as a function of r and testing nearest neighbour interactions with a KMC model fail to explain the models deviation from experimental extinction times. The inhomogeneity of the substrate has to be reduced to improve the match between experiment and theory. This problem was previously noted by Simonsen *et al.* [1], who stated that the effect of the support was difficult to establish due to both morphological and chemical variations.

Ostwald Ripening has been observed to occur in both the diffusion and interface limited regimes. The systems limit was found to be a function of temperature with diffusion controlled ripening occurring past 500°C with a Cu/C system. The regime is also influenced by surface roughness. AFM measurements of the Cu/Si₃N₄ system give an RMS roughness of 2.59nm over 50nm x 50nm, with a line profile indicating a series of peaks and troughs occurring across the sample surface. This system appears to operate in both the diffusion and interface limited regimes, suggesting the variation in the surface structure is affecting the ripening at an individual particle level.

Due to the exponential dependence of the diffusion and interface barriers there is a likelihood, but not a requirement, for them to operate in either limit [184]. The application of KMC removes the requirement for assumption of a limited system when solving Fick's diffusion laws and provides information at the single atom level. This allows for heterogeneous modelling of the system, so that quantities such as surface roughness can be investigated. However, accurate parameters for simulation are required and, despite recent progress by Prevot *et al.* [143], computational costs for KMC simulations are still high.

The primary goal of research into Ostwald Ripening is to obtain a theoretical understanding of the mechanism and then implement this in terms of minimising particle size change or, in the case of single atom catalysts, maintain a high population of atomic species. Based on the work in this chapter, it seems unlikely that an accurate theoretical model could be produced for an industrial system without significant knowledge of surface roughness, particle size,

activation/diffusion barriers and particle specific surface energy. Thus, it is suggested that the focus of the work should not be to produce a system that is representative of an industrial equivalent, but one that can be modelled effectively and then tuned to provide enhanced catalytic activity in an industrial scenario.

This approach has been previously taken by Wettergren *et al.* [60]. Here, particle size was controlled and the driving force for Ostwald Ripening removed and introduced via the use of a bimodal particle size system. This allows for simplified interpretation of Ostwald Ripening; however models are still required to understand the processes occurring.

The subsequent chapter uses Pt/C, improving the Z-contrast imaging so that single atoms can be resolved in H₂. This allows for Ostwald Ripening to be measured at the atomic scale. As the mechanism is observed at its fundamental level, the requirement of modelling to interpret a change in particle size is removed. Ostwald Ripening can therefore be understood without applying the Wynblatt-Gjostein formulation that was originally imposed at a period in time (1975) when experiments were technically limited to observations of only particle size change.

6. Quantitatively studying Single Atoms using ESTEM

6.1. Introduction

Industrial supported metal catalysts typically consist of a broad size distribution from nanoparticles down to sub-nanometre clusters. Sintering mechanisms then alter this size distribution over the course of the catalysts active lifetime. This makes it difficult to maintain efficiency and identify or control the active site of interest. Recent studies [35] have focussed on reducing particle size to sub-nanometre levels, whilst improving activity and selectivity. Taking this concept to the most fundamental level leads to single atom catalysis.

The development of spherical aberration corrected ETEM allows for observation of single atoms in close to reaction conditions [31, 185]. However, the use of ETEM to detect single atoms is inhibited by the dependence on phase contrast and to quantitatively study single atoms in gas, ESTEM is required [32, 33, 36, 40].

ESTEM has been previously utilised via the application of a windowed reaction cell [5, 24, 25]. However, the recent modification of Boyes and Gai's [4] original differential pumping system design has allowed for a differentially pumped ESTEM with Angstrom level resolution [32, 33, 36, 40]. The advantage of the differential pumping system compared to windowed cells is due to the reduction in broadening of the STEM probe. This is because there is no scattering of electrons by the two 50nm thick SiN_x cell windows.

The high (greater than 1bar) pressure capability [23] of a windowed cell is clearly an advantage over a differential pumping system when related to industrial pressure conditions (approximately 100 bar [40, 117]). However, as discussed by Somorjai *et al.* in a review article discussing the 'pressure gap' of surface chemistry, [40, 117] surface reactions are highly dependent on monolayers of gas per second, rather than always requiring industrial reactor conditions.

Single Platinum atoms were first resolved in H₂ in the work of Boyes *et al.* [32]. The following chapter exploits this capability and attempts to quantitatively understand the relationship between single atom density and particle size change in Pt/C, leading to observation of single atom dynamics during Ostwald Ripening. There are clearly many challenges in quantifying single atom density, and these are discussed in the subsequent section.

6.2. Optimising Single Atom Resolution

In order to perform a statistical study on single atoms, the constraints determining their detectability must be mapped out. To begin with, the reaction conditions of temperature and pressure will be expected to alter the number and detectability of single atoms. Temperature will be discussed in section 6.4 and is held constant at 20°C for this study whilst single atom resolution in H₂ has been previously shown to be at the sub-Angstrom level [32].

The next constraint on single atom detectability, as suggested in [186], is the dependence on the migration speed of the atom versus the scan rate of the electron beam. For a scan speed much less than the migration speed, the atom will only be present under the electron beam for a fraction of the dwell time. This scenario leads to the atom not being imaged at all, imaged with a very low SNR (signal to noise ratio) and/or being imaged multiple times. If the scan speed and migration speed are approximately equal, then a smearing of the atom intensity across several pixels may occur. There are two frequencies at which this can transpire, one for the horizontal scan speed and another for the vertical scan speed. The detectability of the atom then also becomes dependent on its direction, as well as its speed.

The scan rate must therefore be much greater than the single atom migration speed for a representative population of single atoms to be detected. As the migration speed may be affected by temperature and the support, the appropriate sampling rate must be determined on a case by case basis.

In addition to these detectability constraints, there is also the question of obtaining a statistically significant sample. For relating particles to single atoms, the requirement is that many single atoms are detected per particle. The number of particles sampled must also be as large as possible. The challenge is therefore to use a low magnification, whilst maintaining single atom resolution by altering the pixel size and dwell time. The limiting factor in the case of Pt/C is the variation in the support height perpendicular to the electron beam. For magnifications less than 4MX, the electronic focus must be adjusted during image acquisition

to account for height variations. By using a 4MX magnification, this issue is avoided and a sufficient sample size (approximately 200 single atoms and 100 particles) is obtained when using the particle production setup described in section 6.3.1.

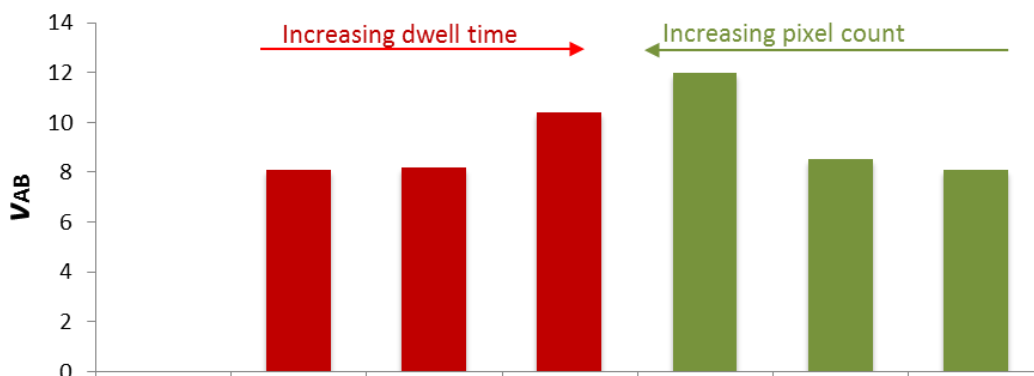
The next constraint is on sample drift. Generally, if the acquisition time is much larger than 2 minutes (clearly this value will fluctuate with microscope conditions), the position of features are perturbed relative to each other. The maximum acquisition time used is therefore 81.8s, but the proportion of this devoted to either number of pixels or dwell time can be chosen. To quantify this, pixel size and dwell time are independently varied at 4MX magnification. The signal from 30 single atoms is sampled along with 30 regions of the same size containing only the C-film. The region sampled is kept at 0.3nm x 0.3nm (although the number of pixels varies) and is therefore comparable in diameter to a Pt atom [187]. To enable contrast measurements, the mean grey value of the sample region is calculated.

Here the contrast is defined as the signal difference between a single atom (S_A) and the C-film (S_B). The contrast to noise ratio can then be defined as:

$$CNR = \frac{S_A - S_B}{\sigma_0} \quad 6.1$$

In an image a single atom occupies n pixels, each with a signal of S_A with independent additive variation between the individual measurements of standard deviation σ_0 . The effective local SNR will be improved by the number of pixels making up a single atom. The CNR is modified by \sqrt{n} , thus defining the visibility v_{AB} of an object. Rose [188] found that objects can be reliably distinguished when v_{AB} is greater than 4 or 5.

$$v_{AB} = CNR\sqrt{n} \quad 6.2$$



Dimension	512px	512px	512px	2048px	1024px	512px
Dwell Time	19.5 μ s	78 μ s	312 μ s	19.5 μ s	19.5 μ s	19.5 μ s
Acquisition Time	5.1s	20.4s	81.8s	81.8s	20.4s	5.1s

Acquisition Parameters

Figure 6.1: Plot of the visibility v_{AB} of single atoms against different acquisition parameters. Single atoms and the C-film were sampled in a 0.3nm x 0.3nm region and the average grey scale value measured. The results of 30 repeats are then used to determine S_A , S_B and σ_0 .

Figure 6.1 shows the expected improvement in v_{AB} as the acquisition time is increased from 5.1s to 81.8s. Note that there is no associated decrease in single atom number for dwell time or pixel size variations. This implies that the scan speeds used in the 5.1-81.8s range are not much less than the migration speed.

Blurring of single atoms is not observed in the range of scan speeds used, as the intensity profile typically measured is Gaussian. Thus the scan rate is not the same as the migration speed and at least a fraction of the single atoms present are being detected with a scan rate much greater than the migration speed.

The maximum dwell time used is 312 μ s, corresponding to 512x512 pixels, with a pixel size of 0.07nm. If the pixel size exceeds the probe size (greater than 0.1nm), then there will be gaps in the raster scan, potentially leading to undetected single atoms. As previously discussed, the acquisition time is limited to 81.8 μ s to reduce thermal drift. Maximising pixel count (2048x2048, 19.5 μ s) provides a v_{AB} of 12, versus 10.4 when dwell time is increased to 312 μ s, 512x512 pixels. The difference between the two is detectable, but likely not significantly different when the temperature or support is altered. However, maximising pixel count does reduce the electron beam dose rate to the sample. Most studies suggest that the significant factor in reducing beam effects is a dependency on dose rate, rather than total dose [30, 189-191]. The following work therefore uses 2048x2048 pixels, at a dwell time of 19.5 μ s. Note that

rastering of the e^- beam pauses at the beginning of each line, thus the acquisition times are slightly longer than those stated for comparison purposes above.

The final parameters of interest are the brightness and contrast levels used to interpret the HAADF detector signal. These are kept at constant values where contrast is maximised (for optimised differentiation between Pt and C) and brightness allows for visibility of internal particle structure, single atom resolution and some substrate visibility (brightness was approximately 1/3 of the maximum value).

Optimised conditions for single atom detectability at 20°C have now been developed. Further work exploring single atom density as a function of temperature and particle structure will be undertaken in section 6.4.

6.3. In situ Ostwald Ripening at the Single Atom Level

Studies of sintering have previously concentrated on determining the mechanism by observation of particle size. This has been attempted via individual particle size tracking [44, 46, 64] and fitting models to PSDs [48, 76, 181]; with only Yoshida *et al.* [31] and Alloyeau *et al.* [185] identifying OR based on single atom observations using TEM. The application of ESTEM allows for a larger observation area, as single atom detectability can be maintained at lower magnifications. The dependence of particle size on single atom density during OR can therefore be observed. Previous work has achieved an observation of the effects of OR (particle size change) and thus an inferred understanding. The focus of this work is towards a direct understanding of the relationship between the effect (particle size change) and the cause (single atom density).

There are several reasons why this approach is informative. Firstly, it allows for testing of the Mean Field and Local Correlation Wynblatt-Gjostein (WG) based [43] models. The concluding remarks in chapter 5 discuss the poor size correlation of single particle OR rates when observed on a rough support. Obviously, there are two approaches to mitigating for this. Firstly, the interparticle distance can be reduced and secondly, more homogeneity in supports could be utilised. Using Pt particles with $r=0.5-1.5\text{nm}$ allows for an interparticle spacing of 2-5nm to be obtained, thus reducing support effects on single atom migration. This allows for comparison of single atom densities with WG assumptions of local or mean field concentrations.

Another advantage is that, assuming a local model, variations in single atom density can be correlated to particle size and decay. However, this is limited by the capability to attribute a single atom to a specific (or group of) particle(s). The accuracy of the density measurement will clearly be dependent on the single atoms detected being, at a minimum, representative of the total populations. This will be limited by detection efficiency and sample size/rate as discussed in the previous section. Limits are also placed by obtaining statistically significant single atom counts. This is partially dependent on the sample preparation techniques, discussed below.

6.3.1. Experimental Conditions

A JEOL JFC2300HR sputter coater was used to deposit 0.2nm of Pt onto a 5nm thick C supported MEMS chip. Prior to experiment start, the sample was heated in HV at 600°C to produce particles with $r=0.5-1.5$ nm. The OR experiment was then performed in 3Pa of H₂. Chapter 5 clearly shows the influence of gas environment on OR rates of Cu on various supports. The influence of H₂ in the case of Pt/C has been investigated by Li *et al.* [192]. They investigate a population of disordered and crystalline Pt particles and then performed a comprehensive statistical study to show that the disordered to crystalline particle transition occurs at a lower temperature in H₂. This is corroborated by the observations of Boyes and Gai [33]. This implies that the OR rate will be considerably different in HV and H₂ conditions, and further work will explore this parameter space. However, operation in H₂ is industrially relevant [193-195] and will therefore be used in this study.

The temperature range used in chapter 5 with Cu on various supports, was from 400-550°C, with observation of PMC occurring slowly (relative to OR) at 550°C and dominating at greater than 550°C. Here, the limit was observed to be 250°C, with PMC occurring at more than 300°C as seen in Figure 6.2. As discussed in chapter 3, PMC derives from adatom diffusion on the particle surface causing the centre of mass to migrate. Mobility is greater at high temperatures for small particles [46, 186], thus as smaller particles are used in this experiment ($r=0.5-1.5$ nm rather than 3-10nm for Cu) and the interparticle distance is reduced, the OR to PMC temperature transition would be expected to be lower.

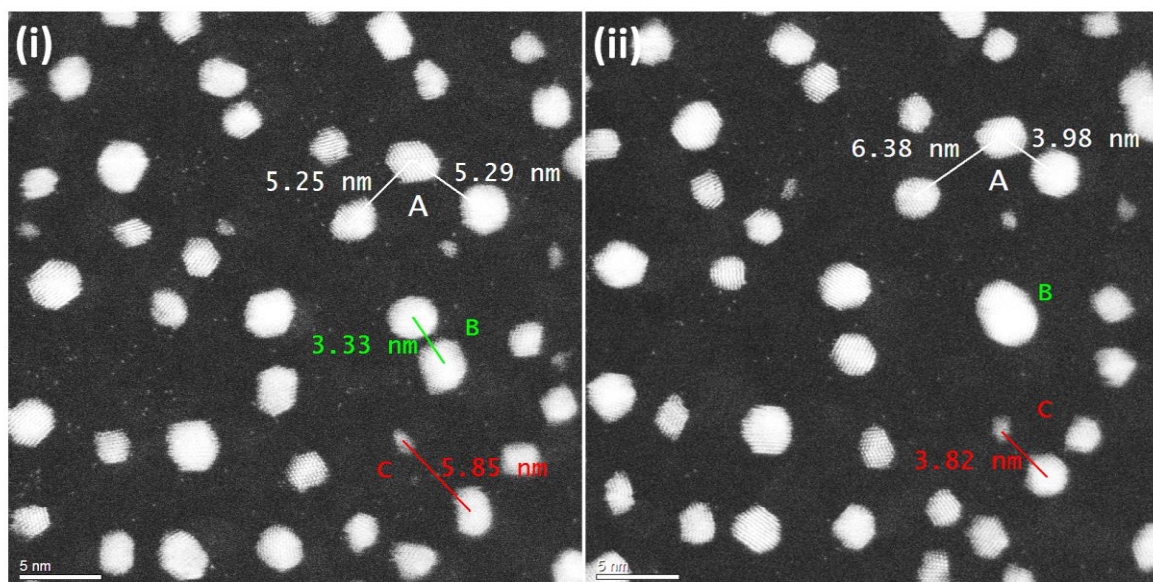


Figure 6.2: Observation of PMC at 400°C in 3Pa H₂. The time difference between (i) and (ii) is 20 minutes. Migration of several particles occurs, including those labelled A and C. Migration and coalescence is observed at B.

A 23.5nm x23.5nm area was observed continuously for 75 minutes at a sample rate of 1/5 minutes, which was previously used in chapters 4 and 5. As discussed in section 6.2, observations of single atoms were optimally performed at 4MX with a 0.017nm x0.017nm pixel size (2048x2048 pixels with a dwell time of 19.5µs). A low magnification (1.2MX) image was taken of the experimental area to attempt to quantify beam effects. From Figure 6.3, there is no obvious change in either the PSD shape or the mean particle size of the areas exposed or unexposed to the electron beam. This indicates that electron beam influence has been minimised by using a 1/5minute sample rate. However, the lighter background of the exposed area indicates that contamination, probably carbon based, has built up over the course of the experiments. This was not observed in OR experiments in chapter 5, due to the higher temperature (400-550°C) and lower magnification (600KX) used.

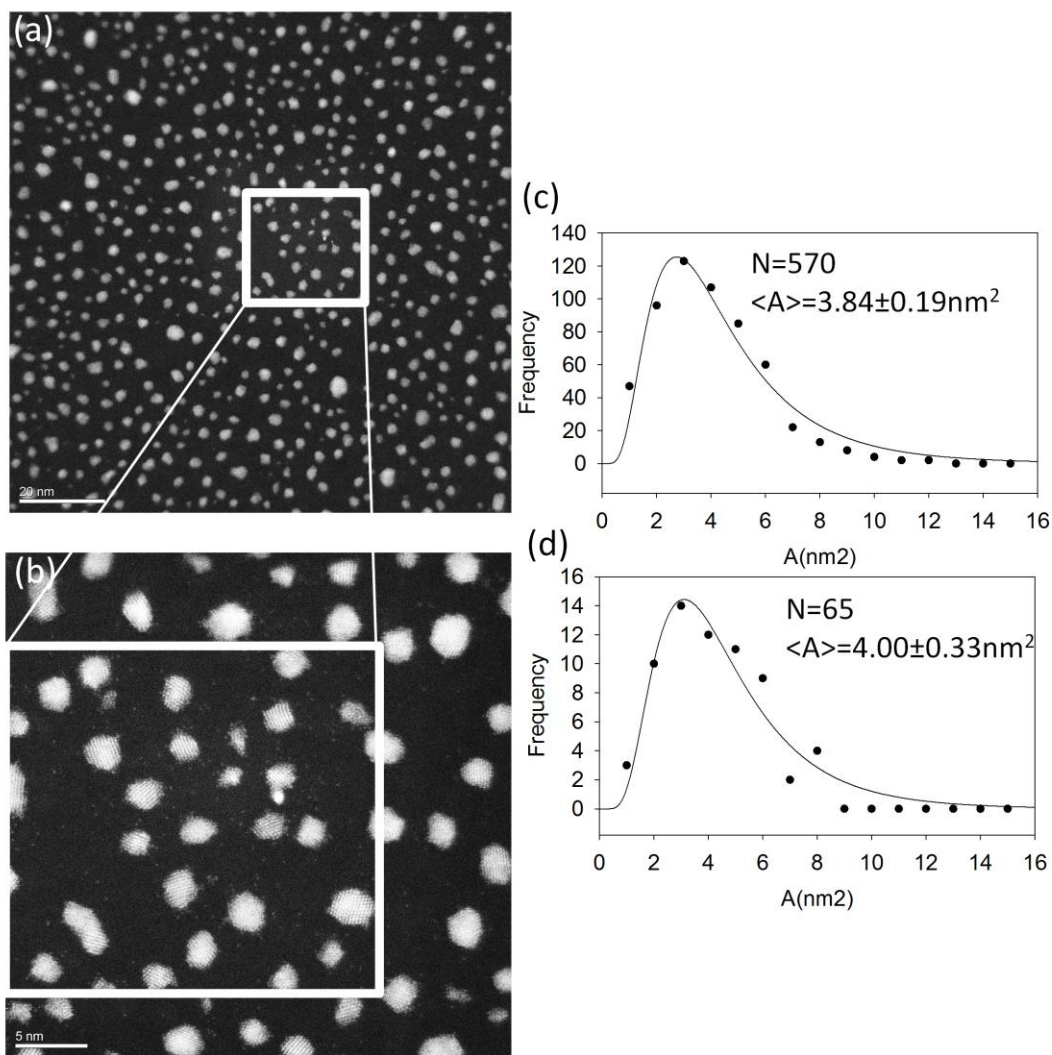


Figure 6.3: (a) Low magnification (1.2MX) image of experimental area after 75 minutes at 250°C, 3Pa H₂. (b) 4MX high magnification image of the 23.5nm x 23.5nm experimental area after 75 minutes, (c) PSD with lognormal fits of low and high (d) magnification images, showing that the mean particle size agrees within error.

Over the course of the 75 minute experiment, 16 high magnification (4MX) images were taken. The positions of the single atoms and particles in each frame were calculated relative to 4 large particles in the corners of each image. This minimises the influence of particle migration, although none was detected above the noise due to particle shape changes. The error in single atom position is thus the difference between alignment of the four particles in each image.

6.3.2. Quantifying Single Atom Density

The key issue in relating particle size and single atom density is to obtain a large enough sample to provide a representative overview of the processes occurring. Clearly, large datasets are required, with the number of single atoms detected much greater than the number of particles measured. As discussed in chapter 5, a single atom's motion is governed by random walk, and thus the probability $P(d,t)$ of its position d at time t is proportional to e^{-d^2} . If left for an infinite amount of time, the single atom would return to the original particle source with a probability of unity. However, the nearest neighbour particles provide sinks for the single atoms, thus reducing this probability to below 1.

The probability of interaction with a nearest neighbour particle depends on d and D (the diffusion coefficient). The next nearest neighbour also clearly has an influence, but has the additional constraint of angular coverage w . The proportion of single atoms interacting with the next nearest neighbours is reduced by the angular coverage, w , of the nearest neighbours, in addition to the exponential dependence of d . As more orders of next nearest neighbour are considered, the calculation becomes closer to the mean field model. In the following study, the single atom density is treated as a property of either the individual particle, or the local region (i.e. nearest neighbours). The accuracy of this treatment is clearly dependent on the parameters discussed (d,D,w), amongst others not mentioned in this simplified model (e.g. support inhomogeneity, particle structure, temperature and gas environment). There is an inherent statistical advantage in the initial assumption that nearest neighbours influence single atom density: the number of atoms considered increases with the number of nearest neighbours. The single atom density around a single particle is explored to ensure damping of trends by averaging over nearest neighbour data does not occur.

Firstly, the assumption of a mean field or local correlation single atom density is investigated. Up until 50 minutes into the experiment, particles have not begun to significantly decay. The single atom density can therefore be summed over this period ($t=0-50$ mins), whilst assuming the particle size remains roughly constant. As discussed in section 6.3.1, 11 images are obtained in this period and thus the ratio of single atoms:particles is improved approximately 11 fold.

Figure 6.4 clearly shows that the density of single atoms varies across the sample area. The diagram consists of 11 superimposed images, with each image containing a mean of 81 ± 19 single atoms. The field of view is $23.5\text{nm} \times 23.5\text{nm}$ and thus with a raster size of $0.76\text{nm} \times 0.76\text{nm}$, each bin should contain 0.08 atoms. Superimposed over 11 images this increases to 0.93 atoms per bin. This is considerably less than the approximately 14 atoms per bin observed

over some parts of the sample and thus illustrates the unsuitability of a mean field model in this case. However, the sampling rate must also be considered. In this case one image was taken every 5 mins, as previously performed in chapters 4 and 5. This could clearly have an effect on the density observations if it is too slow. For example, the data may be skewed by the presence of a large number of atoms in one region of a single image. This could lead to the Mean Field approximation being applicable over a time scale longer than the microscope acquisition time (in this case 19.5 μ s dwell time and 2048x2048 pixels). However, if the density of single atoms is approximately constant between images and the density induces size changes in the particles over the observation period, the Mean Field approximation is clearly not applicable on any timescale over an area of this size. Over the course of observation (at times greater than 50 minutes), particles 17 and 18 decay, whilst the single atom density does not increase past 2 atoms/nm² in any one image. As a change in particle size is observed, the single atom density variation can be assumed to not be a product of mean field short term fluctuations. Therefore, this observation supports the inapplicability of the mean field model in this case.

High single atom densities are observed in the area containing particles 7, 8 and 10, with a much lower density found nearby 17 and 18. Particles 17 and 18 decay (Figure 6.6), whilst 7, 8 and 10 show size fluctuations of 42%, but no decay trend. This leads to the slightly counter-intuitive conclusion that a higher density of single atoms implies high exchange rates, as opposed to high net movement of mass between particles.

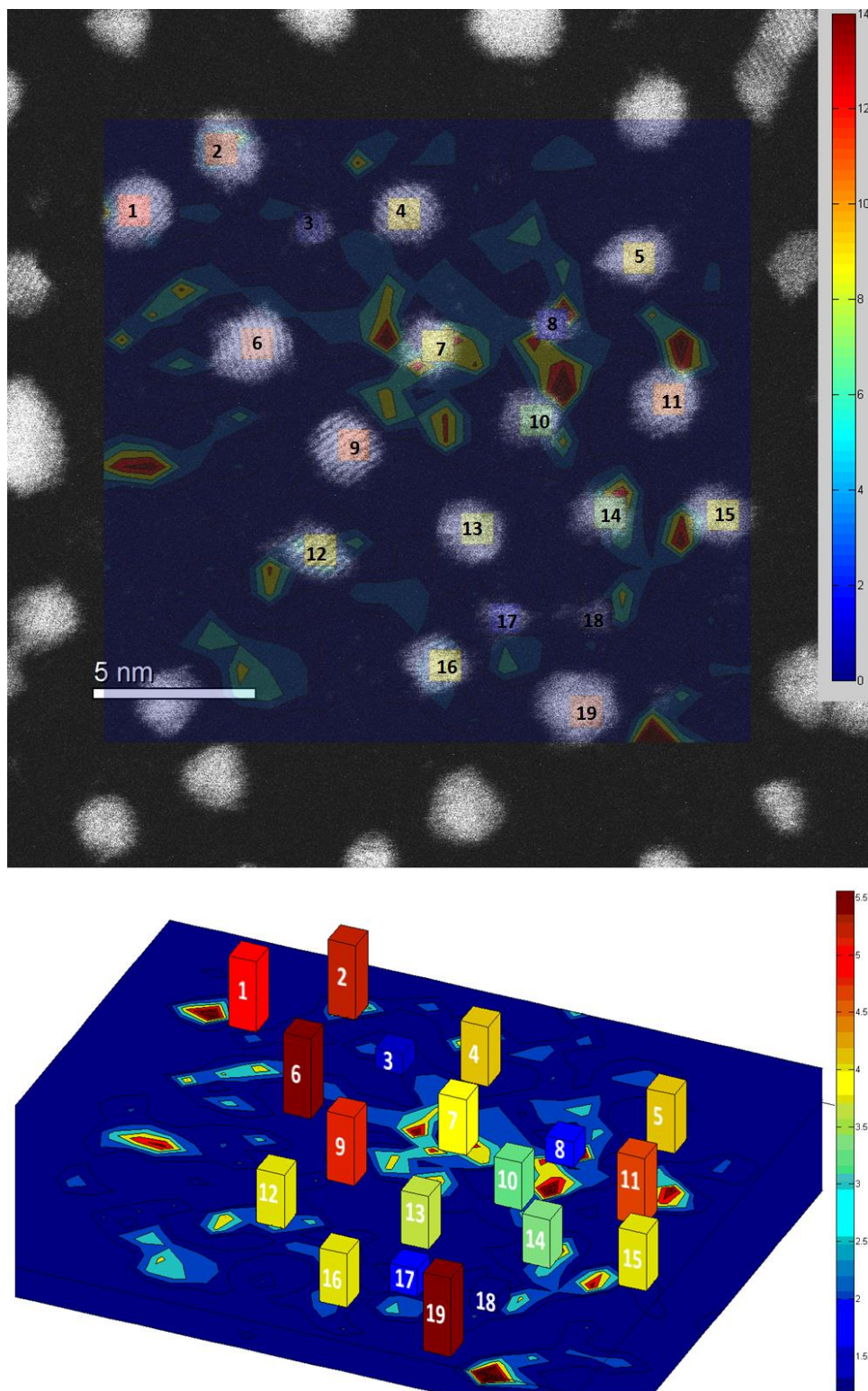


Figure 6.4: (Top): Single atom heat map from $t=0$ to $t=50$ mins, at which point no particles have become extinct. This is overlaid on a HAADF STEM image at $t=0$. Heat map is rastered with a bin size of $0.76\text{nm} \times 0.76\text{nm}$. Particles 1-19 are labelled for reference purposes and the colour bar applies to the single atom count. (Bottom): Heat map is the same, but particles in the overlaid image are replaced with bar plots to indicate particle size. Colour bar on right applies to particle area in nm^2 . Note that an averaging technique has been applied to smooth the single atom data and form a contour plot.

The idealised density of single atoms can be considered dependent on three probabilities: emission, diffusion and reattachment. A large total nearest neighbour mass will obviously increase the emission and reattachment probabilities and lead to high single atom density observations. This therefore illustrates the requirement to observe single atom densities over the local area (nearest neighbour regions) so that account of phenomena where particles are influenced by high or low local single atom emitters can be explored.

A local correlation is taken, whereby single atoms are attributed to individual, or groups of, particles. One method of achieving this is through the use of Voronoi constructions, as performed in chapter 5. The region of influence of a particle is assumed to consist of any point that is closer to that particle than to any other. Nearest neighbours are defined as particles that share a Voronoi boundary. The conversion between the raster map and the Voronoi cells can be seen in Figure 6.5. When using a nearest neighbour model, particles at the edge will be influenced by factors beyond the region of observation. Mitigation for this has been attempted by reducing the single atom observation area to the inward facing sides of edge particles. This reduced sample area can be seen in Figure 6.5(b). The solution is not ideal, as it assumes that single atoms observed on the outer facing sides of edge particles were not generated within the sample area (and vice versa for inward facing sides). The modification also disregards around 50% of the local area contributing to size changes of the edge particles, thus ideally only non-edge particles should be examined.

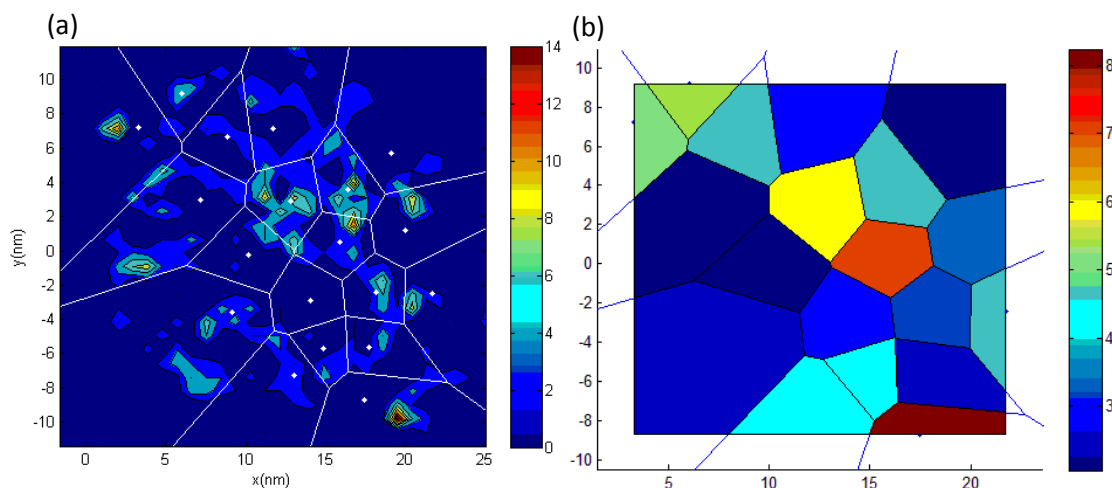


Figure 6.5: (a) Heat map of single atoms from Figure 6.4 with a Voronoi overlay (b) single atom densities calculated using the Voronoi overlay instead of the raster. The colour bar (a) displays the number of single atoms per bin, (b) displays the single atom density per nm^2 in a Voronoi cell.

6.3.3. Relating Particle Decay to Single Atom Density

Having applied a Voronoi construction to the sample area, the decay of particles 17 and 18 can now be analysed by averaging single atom numbers over a larger area (the nearest neighbour Voronoi regions) as opposed to over time. This improves the statistics sufficiently to allow for quantitative time dependent single atom density observations to be made. Looking at Figure 6.6 the single atom density at (a) $t=10$ mins, is high, decreases considerably at (b) $t=40$ mins and then increases again after particles 17 and 18 have decayed at (c) $t=70$ mins.

Figure 6.7 shows a clear correlation can be seen between the change in size of particles 17 and 18, and the density of single atoms in the nearest neighbour Voronoi cells. Interestingly, the local single atom density begins to decrease prior to particle size changes, thus suggesting that the decay of particles 17 and 18 is driven by the absence of single atoms to replace those emitted by the particles.

There is also evidence of the interaction between particles 17 and 18. Once the concentration of single atoms decreases below the rate of emission from particle 17, the particle size begins to decrease at $t=30$ minutes. This is accompanied by an increase in size of particle 18, suggesting it is emitting at a lower rate. Eventually, when their sizes are approximately equal at $t=50$ minutes, particle 18 also begins to decay, which corresponds with a spike in the size of particle 17 at $t=60$ minutes. Assuming (i) emission from both particles is a function of surface area, rather than disorder (i.e. the degree of a particles crystallinity) and (ii) the disorder reduces the influence of the Gibb-Thomson relationship on emissivity; this result also suggests that smaller particles are able to survive in a lower single atom concentration due to their assumed lower emission.

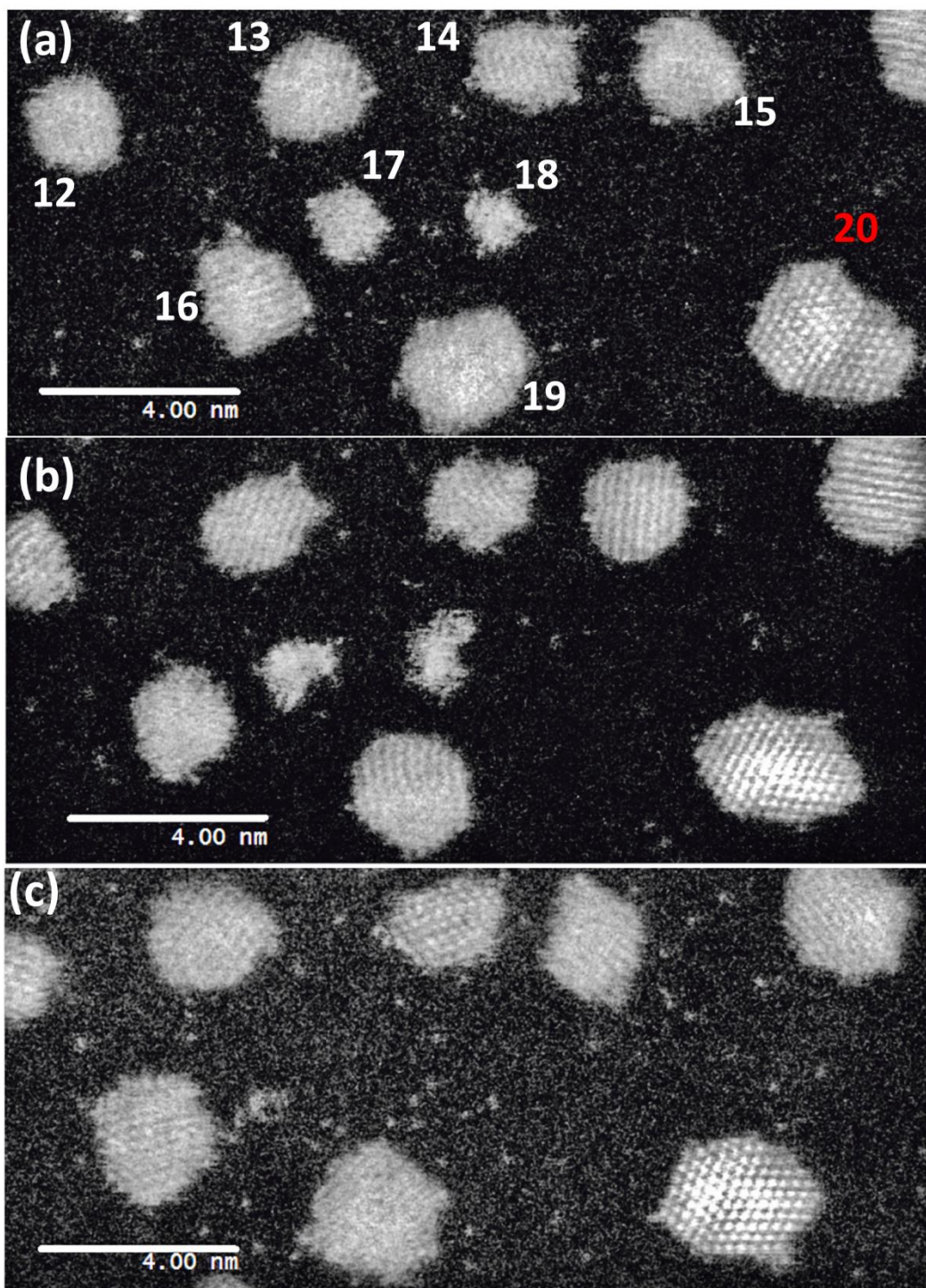


Figure 6.6: Observations taken in 3Pa H₂ at 250°C. View of the local area of particles 17 and 18 at (a) t=10 mins, (b) t=40 mins and (c) t=70 mins. A decrease in single atom density is observed in (b), with increased disorder of particles 17 and 18. Particle 20 (highlighted red) was not included in the Voronoi analysis, as it was not within the field of view of the microscope throughout the experiment. It is included here to illustrate the local environment of particle 18. Note also the increased brightness of the support between (a)-(c). Experimental brightness and contrast conditions were kept constant over the experiment, but due to the low temperature (250°C) some contamination has built up on the sample area. The low level of contamination that builds up has little influence on the OR rate (Figure 6.3), and may therefore be occurring on the underside of the substrate as discussed in [7]

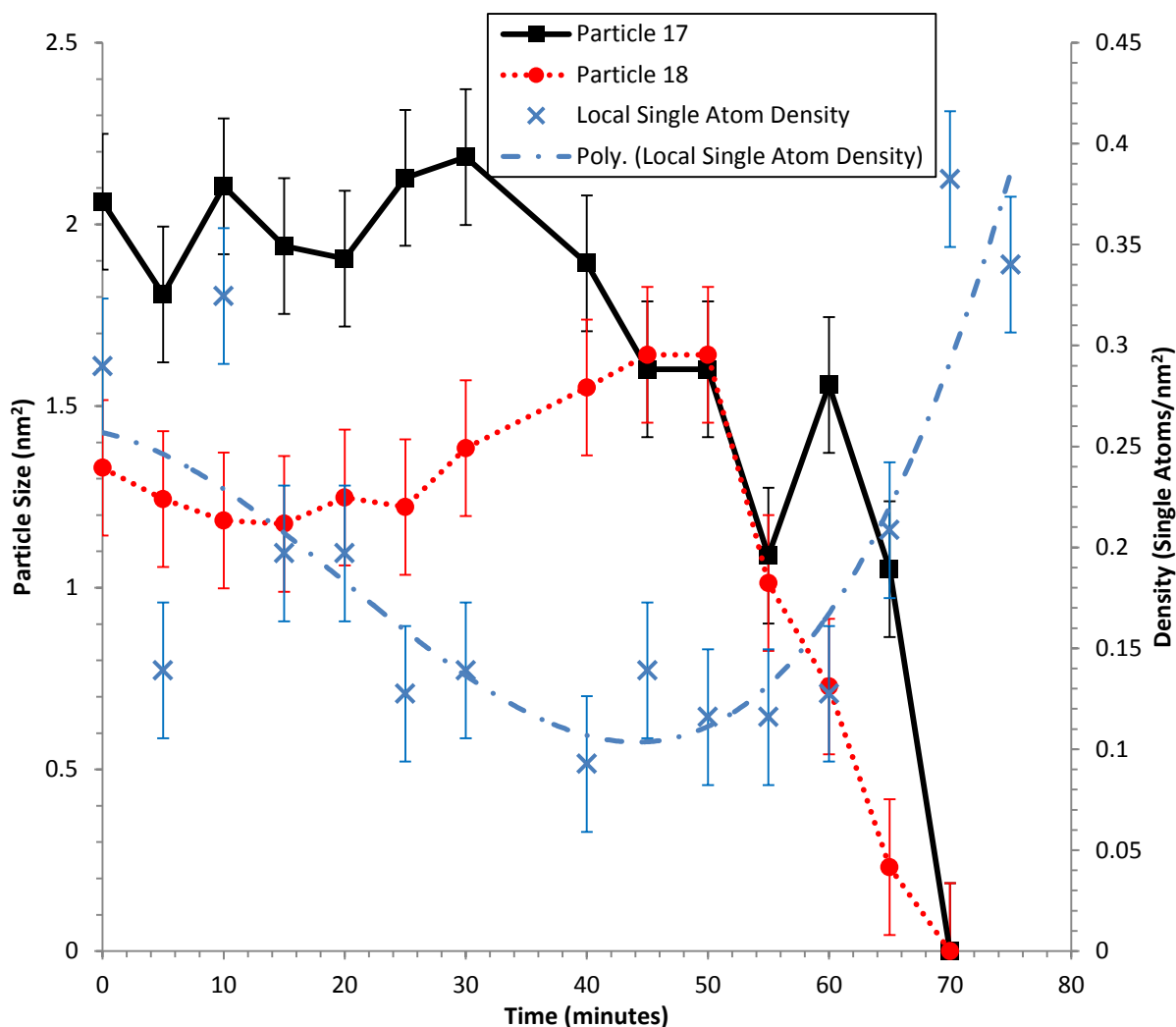


Figure 6.7: Size of particles 17 and 18 during experimental time frame of 75 minutes. Sampling rate is 1/5 minutes. The local single atom density is calculated from Voronoi cells neighbouring particles 17 and 18, the cells included are: 12, 13, 14, 15, 16, 17, 18, and 19. A third order polynomial has been fitted to the local single atom density data, indicated by the dot-dash line. Errors in particle size are calculated by measuring the average image to image change in particle size, as performed in chapter 5. The error in the single atom density is calculated by taking 5 successive images, counting the number of single atoms, then finding the corresponding single atom density variation.

Towards the end of the experiment at $t=60-70$ minutes, the single atom density appears to increase again. Particles 17 and 18 decay to $r=0$ at $t=70$ minutes, thus intuitively one would expect a reduction in the single atom density once these net emitters have disappeared. The increase in density over 4 observations (20 minutes) strongly implies that the single Pt atoms are being anchored by the C support. Diffusion then proceeds via a series of jumps between anchor sites, with single atoms remaining approximately stationary between hops. This is similar to the conclusion reached by Batson [189], who found the Au atoms remain stable on C

for around 15s before hopping a distance of around 2nm. The principle of anchoring migratory single atoms so that stabilised active sites are provided for reactions is an area of increasing interest, with a review article by Yang *et al.* [35] citing examples such as anchoring of Pt single atoms on $\gamma\text{-Al}_2\text{O}_3$ by Kwak *et al.* [86]. Further exploration of single atom anchoring using in situ HAADF STEM would be even more intriguing if performed on an industrially relevant system, as done by Kwak *et al.* [86], but is outside the scope of this work.

The above analysis assumes that the local correlation model (using a Voronoi averaging technique) is applicable to this situation. To ensure that the single atom density changes are not an averaging effect, the observation area was changed to the individual Voronoi cells surrounding particles 17 and 18, Figure 6.8. This shows a similar decrease in single atom density at $t=25$ mins, and increase at $t=55$ mins, showing that the trend is not an artefact introduced by surrounding particles and their nearest neighbours. The single atom density can also obviously be affected by focussing errors or other misalignments when acquiring images. If this was influencing the ‘bathtub’ trend from Figure 6.7, then the single atom count across the image would follow the same trend. From Figure 6.9, it can be seen that this is clearly not the case.

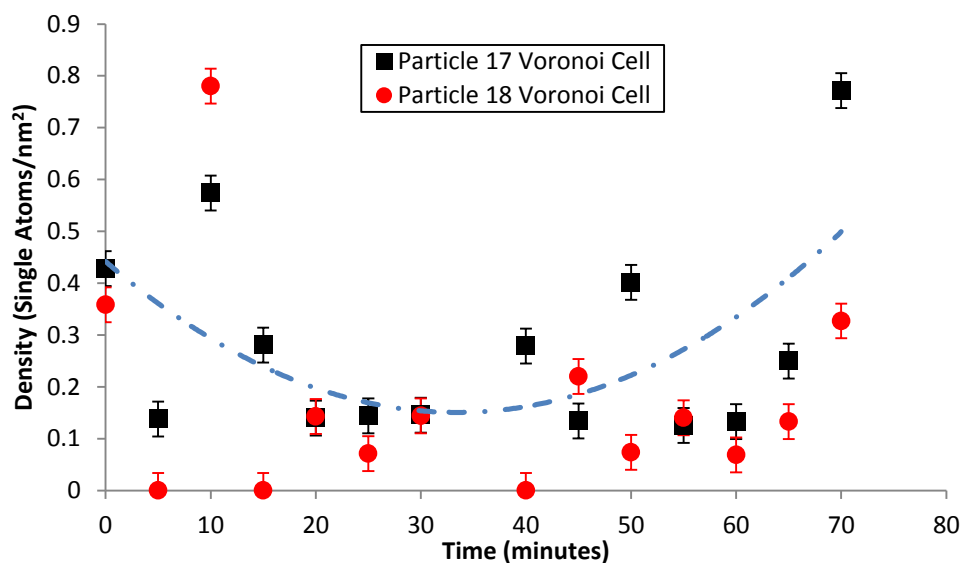


Figure 6.8: Single Atom density in individual Voronoi cells of particle 17 and 18. A second order polynomial fit is shown by the dashed blue line. The initial decrease and post decay increase in single atom density is shown to be representative of particle 17 and 18 Voronoi cells.

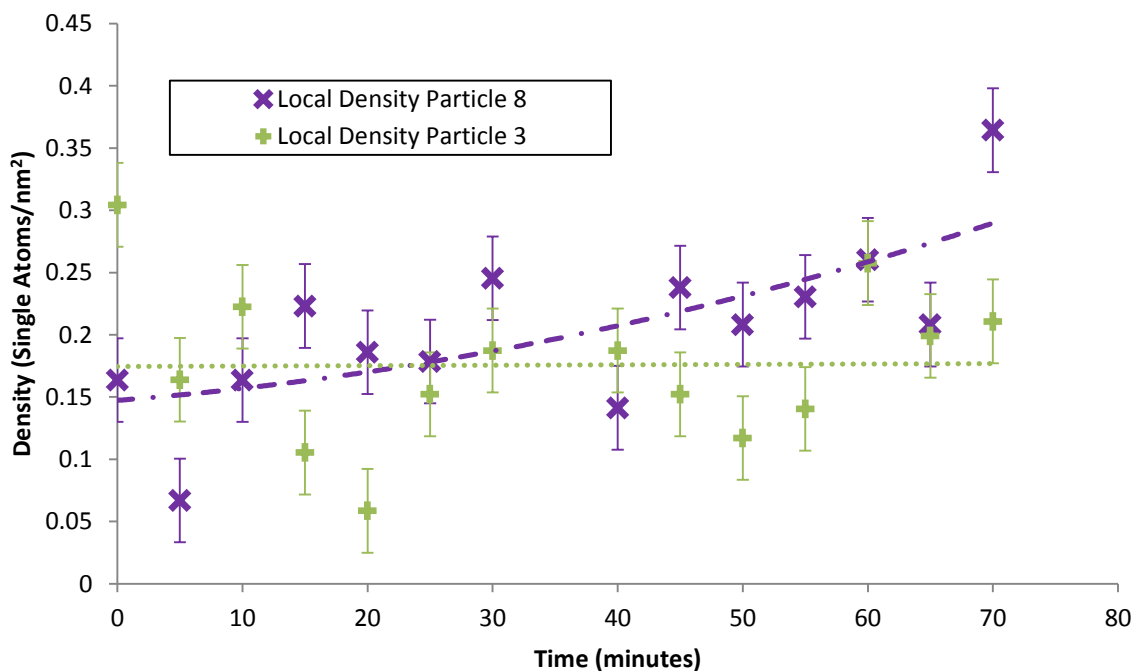


Figure 6.9: The single atom density in the nearest neighbour regions of particles 3 and 8. Particles 3 and 8 are disordered and of similar size to particles 17 and 18. However, the local single atom density does not decrease during the experimental time frame, possibly due to the influence of nearest neighbour particles.

The initial change in single atom density around particles 17 and 18 may be dependent on the changing particle structure of the nearest neighbours. In Figure 6.6(a) particles 12, 13, 14, 15, 19 appear to have no faceting and very little lattice resolution. Particle 20 is oriented in the [101] axis with a twin boundary and may have undergone a coalescence event prior to the first observation. After 40 mins, Figure 6.6 (b) shows increased faceting of particles 19 and 20, and clear observation of lattice fringes in particles 12, 13, 14 and 15. The exception to this is particle 16, where lattice fringe resolution is poorer. From Figure 6.7, there is a reduction in the single atom density of particle 17 from 0.67 atoms/nm² at t=0 minutes to 0.15 atoms/nm² at 40 minutes. The reduced surface free energy indicated by the increased ordering of the nanoparticles likely affects the decrease in single atom density, however is difficult to quantify.

From Figure 6.9, the density of the regions surrounding particles 3 and 8 can be seen. Particles 3 and 8 are similarly disordered and (from Figure 6.10), with 17 and 18, make up the smallest 4 particles observed. However, their local single atom density appears to increase or stay constant over the experimental time frame, despite increasing crystallinity being observed in the surrounding particles. In order to quantitatively correlate particle structure with single atom density, a through focal series is required to determine crystallinity. A through focal series has been previously used by Li et al. [192] to study a sample of more than 3000 particles

disorder-crystalline transition. However, particles may not be in zone axis orientation, thus making quantification difficult. It is suggested that particles with controlled initial size, and perhaps shape, are required to undertake this study more readily, whilst crystallinity analysis could be simplified by using nanodiffraction.

6.3.4. Application of Local Correlation Models

Application of the WG local correlation model discussed in chapter 5 allows for an exploration of particle decay based on mass and geometry. Figure 6.10 shows the non-size ordered decay of the smallest four particles observed, particles 3, 8, 17 and 18. Particles 17 and 18 are the first to become extinct, despite particle 17 being the largest of the four. Application of the local correlation WG interface model (Figure 6.11) shows a size ordered decay. Interestingly, applying the diffusion controlled model (Figure 6.12) causes the extinction times of particles 8 and 17 to be equal. As discussed by Morgenstern *et al.* [64], application of the local correlation model is inherently more pronounced in a diffusion limited case. The previous observation of a high single atom density after particle decay implies that the diffusion speed of single atoms cannot be approximated as being much greater than the rate of atom detachment. The diffusion controlled local model should therefore be more applicable in this case, and the prediction of an equalised extinction time for particles 8 and 17 provides a closer match to experimental results than that obtained with the interface controlled model.

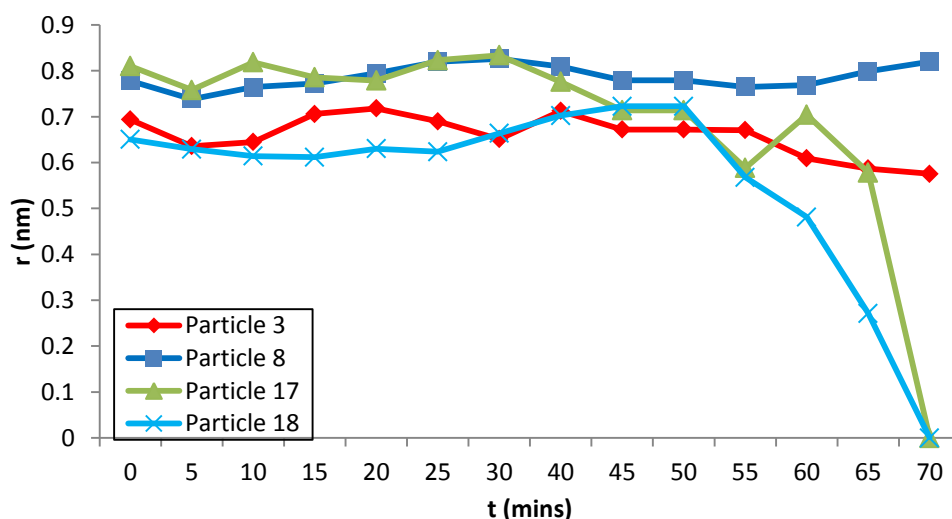


Figure 6.10: Particle radius (r) against time for experimental HAADF STEM observations of the smallest four particles. Note that r is used rather than particle size to directly compare with WG models, where particles are assumed to be hemispherical. The error in r , $\sigma_r=0.04\text{nm}$, is calculated by measuring the average image to image change in r , as performed in chapter 5. Only particles where a trend in particle size change was (by eye) indiscernible from noise were included.

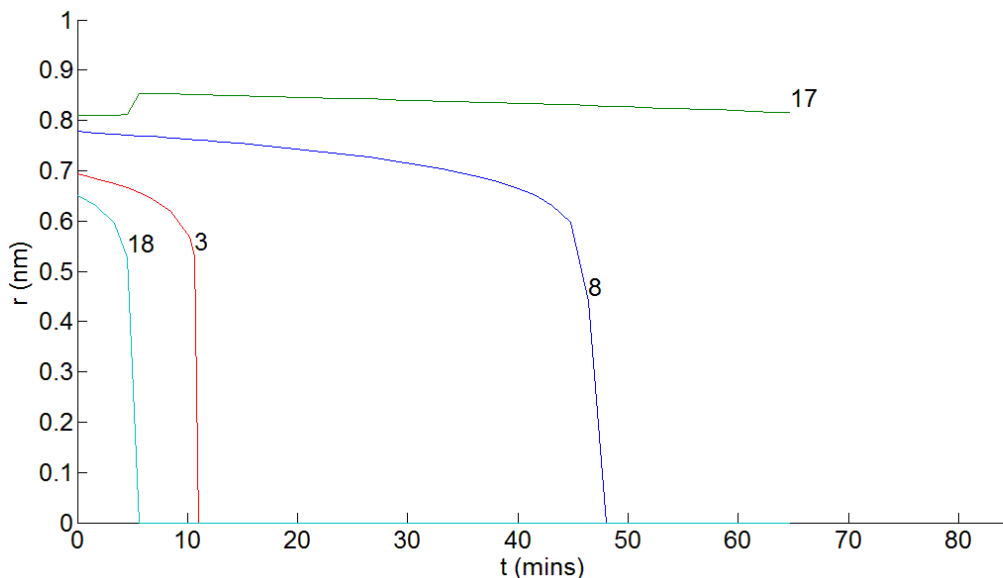


Figure 6.11: Application of the local correlation interface controlled model with surface free energy (γ) of 1.7J/m^2 , $E_{\text{Tot}}=190\text{kJ/mol}$. Surface free energies in ripening and WG models typically ranges from $1.5\text{-}2\text{ J/m}^2$ [44, 181, 183, 196, 197].

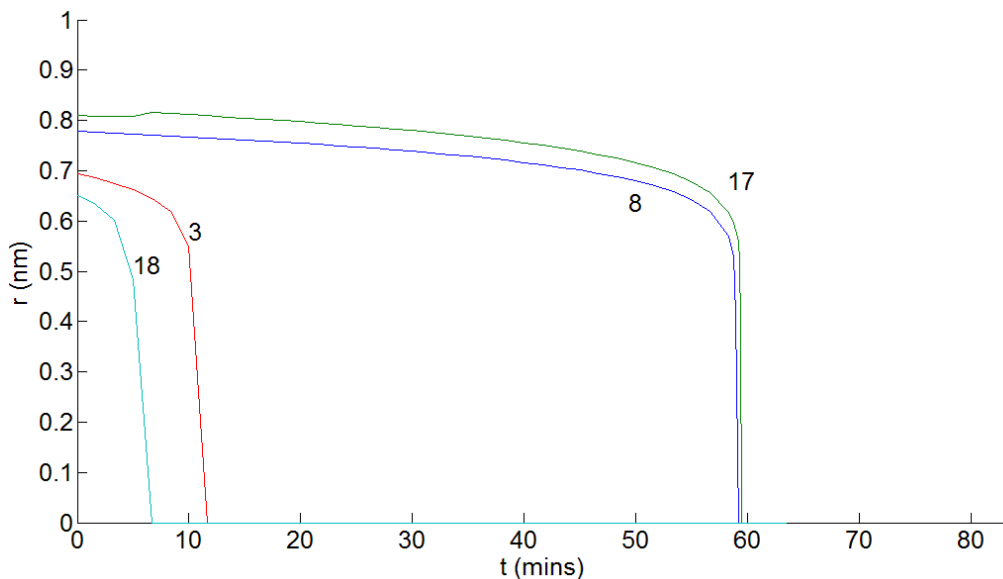


Figure 6.12: Application of the local correlation diffusion controlled model with $\gamma=1.7\text{J/m}^2$, $D \cdot E_{\text{Tot}}=368\text{kJ/mol}$.

In summary, the single atom density has been investigated by sampling over the local area of a particle defined by nearest neighbour Voronoi cells. This has provided improved single atom statistics and thus the decay of two particles (17 and 18) can be related to the single atom density changes. An increase in single atoms post decay suggests that atoms are anchoring on the C-support. Qualitative analysis of particle structure indicates that there are 2 particle types: disordered and crystalline. These particles likely have different single atom emissivity characteristics and this will be investigated in the following section.

6.4. Single Atom Density as a Function of Environment

As discussed in the previous section, the particle structure has influence on the local single atom density. The most extreme example of this is encountered when observing small disordered particles compared to larger ones with a much greater degree of crystallinity. This has been previously investigated by Boyes *et al.* [33], where faceting of Pt nanoparticles was found to occur at 400°C in H₂. The addition of H₂ was seen to increase the overall crystallinity observed, compared to HV conditions. This is in agreement with work by Li *et al.* [192], who found that approximately 80% of Pt particles with a diameter of 1.7nm are crystalline. This is reduced to 55% when HV conditions are used. The environmental conditions used for this study were 1 Torr H₂ at a temperature of 385°C.

The following work uses the same microscope conditions as discussed in section 6.3.1. However, Pt nanoparticles are synthesised without annealing, thus leading to a sample of small disordered clusters and 'rafts' (Figure 6.14a). As reported by Li *et al.* [192] and Boyes *et al.* [33], increasing the temperature leads to increased faceting of the nanoparticles (Figure 6.14b,c). Temperature will also clearly have an effect on both the emission rate and diffusion speed of single atoms. Therefore, there are three parameters changing with temperature that affect single atom visibility or density: particle structure; single atom emission rate; and diffusion speed. Ideally, these variables would be investigated separately by using Pt nanoparticles with controlled crystallinity and size [60]. In this exploratory work, the effect of changing particle structure has been mitigated for via annealing for 5 minutes at 600°C. This enables a subsequent temperature series with reduced influence of particle structure on the single atom density.

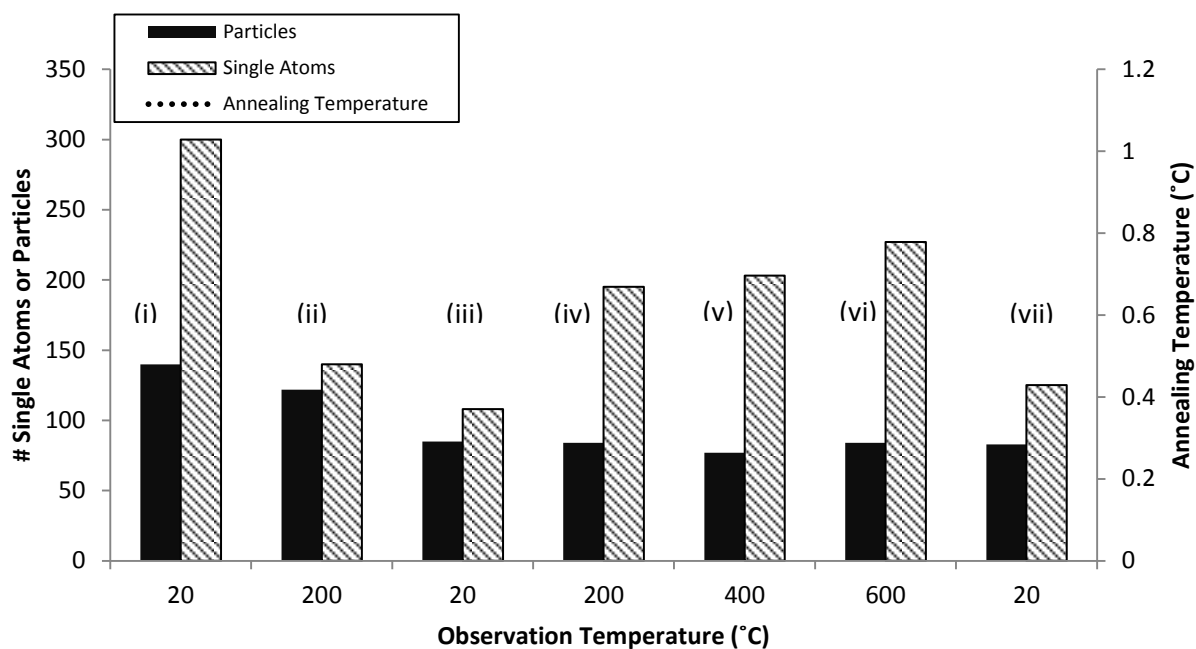


Figure 6.13: Temperature profile during the experiment with a count of the number of single atoms and particles observed in each case. For observations (i) and (ii), the annealing temperature is the same as the observation temperature. For observations (iii)-(vii), the annealing temperature is 600°C. Each observation was taken after 5 minutes at the stated temperature.

The experimental structure can be seen in Figure 6.13. Measurements are made without annealing above the observation temperature (i)-(ii), and these are followed by a temperature series post 600°C annealing (iii)-(vi). The change in particle number during the temperature series shows a maximum variation of 8. This suggests that particle migration and coalescence (PMC) is minimised during the data acquisition by allowing only 5 minutes at each temperature step. Note that each observation is of a different sample area so as to avoid contamination influencing subsequent results and also reduce beam influenced effects.

At room temperature (i), with no annealing, the disordered clusters emit a high number of single atoms, with a low diffusion speed. As the temperature is increased to 200°C (ii), the number of single atoms reduces from 300 in (i) to 140. More discrete particles are formed with some crystallinity, although most appear disordered at the surface. Short term observation indicates that particle size change occurs primarily via PMC. The annealing temperature is increased to 600°C to produce more thermodynamically stable particles. The proportion of disordered particles is thus reduced, along with the tendency of particles to change their shape or structure between temperature steps. This is demonstrated by the stability in particle

number in studies (iii)-(vii). Post annealing, single atom density as a function of temperature can be investigated.

Observations (iii) and (vii) show a reduction in single atom number at room temperature compared to (iv)-(vi). This suggests that at a temperature as low as 200°C, the activation energy for single atom emission is exceeded. When the sample is quenched by decreasing the temperature to 20°C, single atom numbers decrease possibly because there is no additional emission. The single atoms remaining are presumably strongly anchored to the C-support, whilst weakly anchored atoms diffuse to nearby particles. This suggests that, at least in this system, quenching does not allow for enhanced detectability of single atoms by reducing the diffusion speed.

There is a slight increase in single atom number observed between (iv) 200°C, (v) 400°C and (vi) 600°C. Assuming a Gaussian based emission probability, then it can be expected that the number of single atoms emitted will increase with temperature. However, the number of single atoms detected at higher temperatures may decrease. The higher temperature will probably cause the mean residence time of a Pt atom on C to reduce (i.e. the migration speed increases). At some temperature, it is hypothesised that the diffusion speed of the single atoms may have increased to such an extent that it far exceeds the microscope dwell time, thus reducing the single atom detectability. Without a highly homogenous support and knowledge of the Pt single atom residence times and preferred anchoring sites (perhaps obtained via DFT calculations) the effect of temperature on single atom count cannot be fully investigated. However, the observations here suggest that once the activation energy for atom emission is exceeded by going from 20-200°C, neither increased emission or reduced detectability dominate in the 200-600°C range. This explains the approximately constant number of single atoms observed in (iv)-(vi).

6.4.1. Effect of Particle Structure

Both section 6.3.3 and 6.4 indicate the presence of small disordered nanoparticles, as well as larger, highly ordered crystalline ones. Boyes *et al.* [33, 40] find increased crystallinity at higher temperatures, and this is observed here in Figure 6.14, when the temperature is increased from (a) 20°C to (c) 400°C (note there is no annealing of the sample beforehand).

The decay of the small disordered nanoparticles (17 and 18) in section 6.3.3 indicates that, as would be expected, they are inherently unstable. This intuitively suggests that single atom density could be used to predict the disorder of a nanoparticle. Unfortunately, this becomes

almost impossible as the density magnitude can be offset by the local particle size, disorder and particle geometry. The statistical noise introduced by these factors make it very difficult to identify differences in the emission probabilities of disordered and crystalline particles when using an averaging technique on a sample of several hundred particles.

To relate particle structure with single atom density without doing a much larger scale study, the approach is taken where the proportion of disordered particles is altered in different experiments. Thus, the proof that single atom emission probabilities change with particle structure is gained from a change in relationship, offsetting the large error due to statistical noise. This is achieved by increasing the temperature and therefore reducing the number of disordered particles.

At low temperature Figure 6.14(a,b), there are typically disordered particles at all sizes, thus the single atom density is mostly dependent on the mass of the local particles. The single atom density therefore increases with the minimum local particle size. However, in Figure 6.14(c) much more faceting of the larger particles can be seen. Note that the smallest particles are often still disordered. The single atom density is seen to decrease with increasing minimum particle size. This shows that regions of high single atom density have a local small ($0.25\text{-}1\text{nm}^2$) particle, whereas regions of lower single atom density often do not. If all particles were disordered, as in Figure 6.14(a), then a smaller particle would indicate a lower total local mass and therefore a lower single atom density. The fact that there is an inverse relationship of single atom density with minimum particle size observed in Figure 6.14(c) shows that there are two populations (disordered and crystalline) of nanoparticles, and the emissivity of the disordered type is greater than the crystalline type.

The differences in particle structure can also be highlighted by observing the local density histogram (Figure 6.15). If high emitting particles are common, then regions of high density should occur frequently in comparison to the mean density. By taking local single atom density histograms of (a) and (c) from Figure 6.14 and then calculating the Fano factor (σ^2/mean) in each case, a measure of the dispersion of the Gaussian distribution can be obtained. The dispersion at (c) 400°C is 0.04, compared to 0.1 at (a) 20°C . This supports the conclusion from Figure 6.14 that there are fewer disordered, high emitting particles at high temperatures.

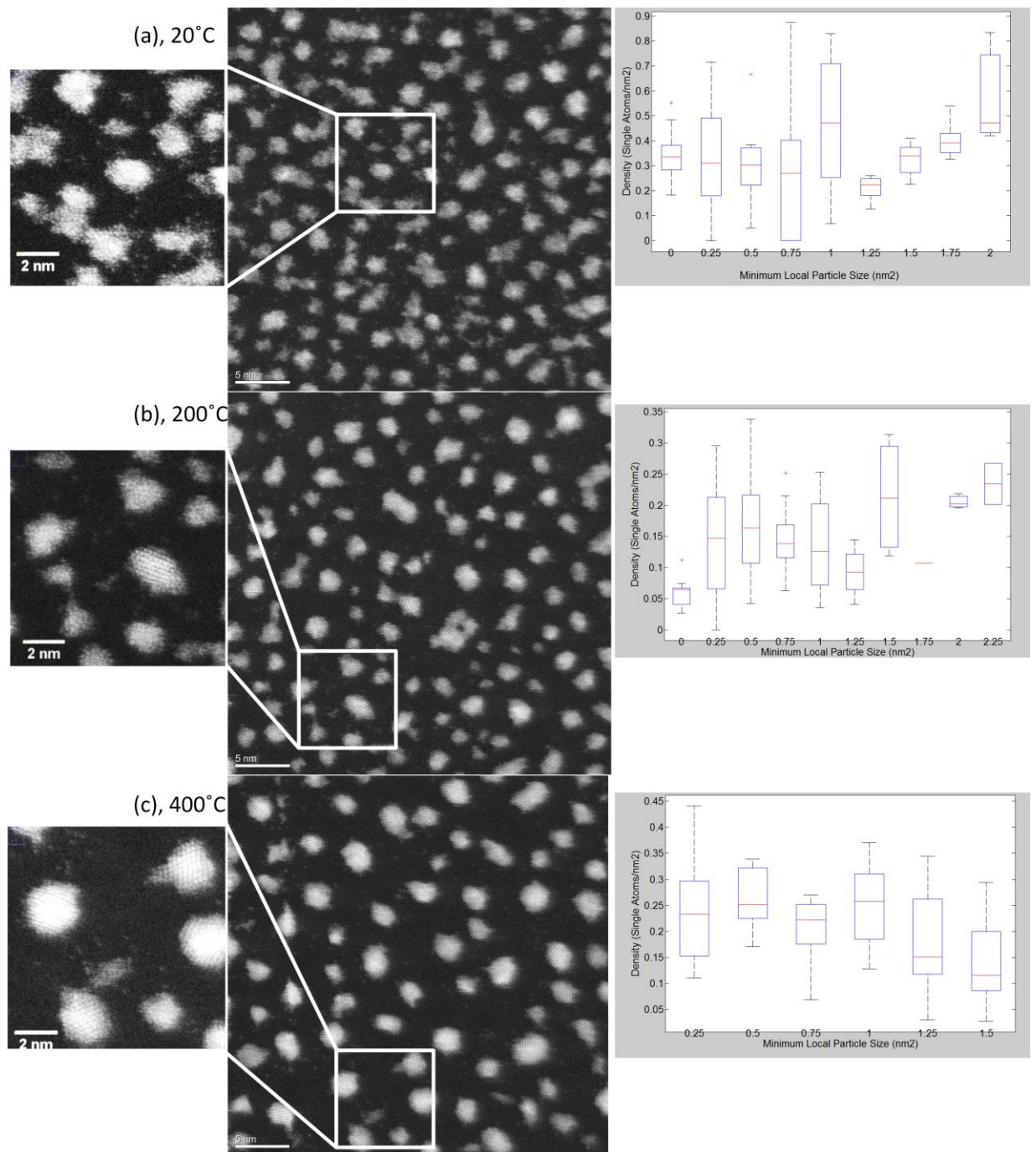


Figure 6.14: (a) Heated to 20°C with many disordered particles present. As temperature is increased to (b) 200°C and (c) 400°C, the number of disordered particles decreases, and more crystallinity is observed. On the right hand side of (a-c) the smallest nearest neighbour particle size (binned to 0.25 nm²) has been plotted against the particle in question's single atom density. A boxplot has been used to show the distribution in each case, with the mean indicated by the red line, standard deviation the blue box and the range by the dotted black bars. Outliers are plotted with a red cross.

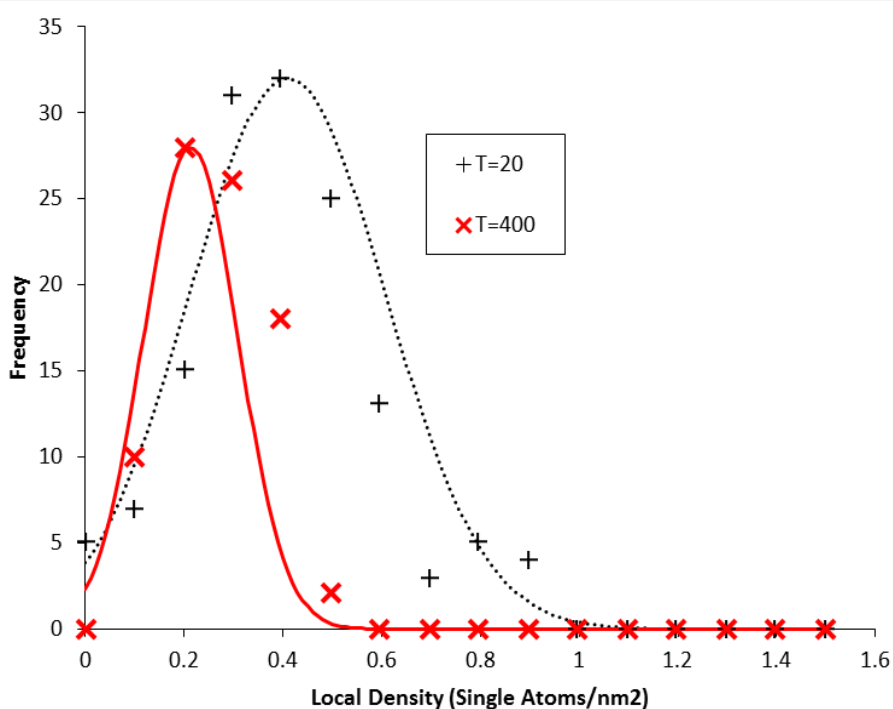


Figure 6.15: Histogram of Voronoi cell local single atom densities at 20°C and 400°C (no annealing has been performed). Gaussian curves fitted to the distributions show mean=0.21 and $\sigma=0.09$ single atoms/nm² when T=400°C and mean=0.41 and $\sigma=0.2$ single atoms/nm² when T=20°C.

6.5. Conclusions

This work has exploited the capability developed by Boyes and Gai [32, 33, 36, 40] to detect single Pt atoms in H₂ gas by relating single atom density to particle size changes and structure. Observation of a 23.5nm x 23.5nm region over 70 minutes shows that single atom density varies across the sample surface, with the single atom count 14 times greater than that expected from the mean field approximation. The approximation [43], where an averaged sea of adatoms exchange with particles, is thus shown to be unsuitable for modelling purposes in this case.

The region of influence of a particle is defined using a Voronoi construction thus enabling relation of single atom density with a specific particle, or its nearest neighbours. This has facilitated the in situ investigation of Ostwald Ripening for the first time at the atomic scale, yielding the observation that particle decay is initiated by a lack of local single atoms. An increase in single atom density post decay suggests that anchoring sites exist on the C support, with the diffusion of single atoms therefore limiting Ostwald Ripening. This is supported by

application of a local correlation based WG model with diffusion limited migration of single atoms. Extension of this via the use of different gas environments (HV, O₂) could be undertaken in the future.

Production of particles yields two distinct types: disordered and crystalline. As discussed by Li *et al.* [192] and Boyes *et al.* [33], there appears to be a disordered to crystalline transition observed at high temperatures. The single atom-particle relationship has been investigated and shown a probable enhancement in emissivity for disordered particles. Further explanation of this will require the use of size and shape controlled nanoparticles, thus reducing the impact of anomalous single atom densities due to particle size, crystallinity or geometry factors.

7. Final Remarks and Further Work

The development of spherical aberration corrected (S)TEMs [2, 3] has led to a wealth of stunning research in electron microscopy. However, the novel ESTEM at the York JEOL Nanocentre, provides the unique ability to image single atoms in gas at temperature [32, 33, 36, 40]. This allows single atom level in situ imaging of nanoparticle catalysts, shedding light on processes that have previously been explained using more indirect, or ex situ, techniques.

In this work, the activation and deactivation (via Ostwald Ripening) of a model Cu catalyst has been observed. Discussion of the reduction mechanisms of CuO has shown two processes by which O is removed from a nanoparticle, whilst also finding that a Cu₂O intermediate phase is observed in low H₂ pressure conditions. This is in agreement with similar XRD based studies [102, 104, 105, 124].

Once the Cu is formed, the dominant sintering mechanism under the environmental conditions used (500°C in 3Pa H₂) was found to be Ostwald Ripening. By increasing the temperature a change in the OR limiting factor was induced. It was also found that the ripening rate was inhibited in HV conditions, a result that appears to be independent of the support used. Variation in the support roughness is a probable cause of the discrepancy between the experiments and kinetic models used to explore them.

Prediction of OR with theoretical models is extremely difficult without accurate knowledge or control of parameters such as surface roughness, particle size, activation/diffusion barriers and particle specific surface energy. In order to provide improved specimen control and Z-contrast, a model Pt/C system was used to explore OR single atom dynamics.

The mean field approximation to the adatom surface concentration during OR was inappropriate for use in the Pt/C system. Particle decay was found to be initiated by a lack of local single atoms, whilst the increase in single atom density post particle decay suggests that anchoring sites exist on the C support. This work has provided a new approach to experimentally understanding OR, by looking at the single atom level, as opposed to previous work [44, 64] which was technically limited to particle size changes.

To conclude, the work in this thesis has utilised new technical capabilities to explore the importance of single atoms. There are three core outcomes relating to this thesis and its potential extensions. Firstly, the ability to understand and reduce OR of nanoparticles by investigating the migration of single atoms. Secondly, the ability to understand catalytic systems by reducing them to the simplest level (single atoms) and then introducing layers of complexity; as opposed to attempting to quantitatively describe the intricacy of an industrial catalyst. Finally, single atoms may actually be the active sites instead of nanoparticles. This would mean a drastic reduction in the necessary mass of precious metals used worldwide, improving both the environmental and economic situation.

There are several approaches that may develop these outcomes. The work here has focussed on single atom statistics as opposed to tracking of individual single atoms. Clearly, if a single atom can be tracked, then much of the sampling approach taken here becomes redundant. The limiting factor in this is the frame rate of ESTEM. At a minimum, the requirement is probable identification of the same single atom between images, therefore necessitating the image acquisition frequency to be greater than the single atom migration speed. This clearly suits the parallel illumination of TEM, rather than the focussed beam raster scan in STEM, however the requirement of Z-contrast remains. The development of HAADF ETEM [198, 199] could yield single atom tracking in the future.

Whilst this would address the migration of atoms, their emission is a property dependent on the nanoparticle in question [35]. Within a catalytic system, there is a large dependency of emission probability on the crystallinity of the sample. At an extreme, there are disordered and crystalline nanoparticles (as observed in the Pt/C samples used here), but as discussed in many studies different crystal planes often provide completely different energetics [112]. Knowledge of the crystallinity of individual nanoparticles is required, when those nanoparticles are not necessarily orientated in the zone axis. Some mitigation is provided by specimen tilting however, it is often unwieldy and makes sampling of many nanoparticles time consuming. One potential alternative is the use of nanobeam diffraction, already a well established electron microscopy technique [7].

However, neither of the two approaches mentioned above alleviate the variation in atomic scale processes that occur across the model systems used in this work. What is required is fine control of the sample variables so that changes can be understood as a function of a single parameter of interest. For instance, the use of controlled size, shape and crystallinity nanoparticles should theoretically reduce the variation in ripening rates between nanoparticles to substrate or local environment effects. A similar study could be performed by controlling the support morphology, and therefore influencing single atom migration. This

level of sample control enables greater resolution of the impact of parameters such as pressure, temperature, support and nanoparticle chemistry.

In summary, through ESTEM the technical capability is now in place to obtain an atomic picture of catalysts in situ. The problem now lies in designing experiments that are constrained enough to provide a comprehensible result. Two obvious approaches to this are to obtain a large enough sample to average out statistical fluctuations, or to control the specimen observed. This is perhaps best expressed using a quote from Williams and Carter [7]: *“Know the forest before you start looking at the veins in the leaves on the trees”*. As with much of electron microscopy, macroscopic sampling is problematic, and thus we are left with the possibility of furthering our understanding by improved specimen control.

List of Acronyms

CNR	Contrast to noise ratio
SNR	Signal to noise ratio
AFM	Atomic Force Microscope
DFT	Density Functional Theory
E(S)TEM	Environmental (Scanning) Transmission Electron Microscope
EDX	Energy Dispersive X-ray spectroscopy
EELS	Electron Energy Loss Spectroscopy
EELS	Electron Energy Loss Spectroscopy
EM	Electromagnetic
ETEM	Environmental Transmission Electron Microscope
FCC	Face Centred Cubic
FFT	Fast Fourier Transform
FOV	Field of View
GT	Gibbs-Thomson
HAADF	High Angle Annular Dark Field
HV	High Vacuum
KMC	Kinetic Monte Carlo
LSW	Lifshitz-Slyozov-Wagner theory
MD	Molecular Dynamics
MEMS	Micro-electromechanical System
MMO	Mixed Metal Oxide
MTP	Multiply Twinned Particle
OR	Ostwald Ripening
PMC	Particle Migration and Coalescence
PSD	Particle Size Distribution
RMS	Root mean square
SAC	Single Atom Catalyst
SADP	Selected Area Diffraction Pattern

STEM	Scanning Transmission Electron Microscope
STM	Scanning Tunnelling Microscopy
TEM	Transmission Electron Microscope
TOF	Turnover Frequency
WG	Wynblatt-Gjostein
WGS	Water Gas Shift reaction
XANES	X-ray Absorption Near Edge Structure
XPS	X-ray Photoelectron Spectroscopy
XRD	X-ray Diffraction

List of Symbols

$\langle \rho_s \rangle$	Concentration of adatoms at L
ΔE	Activation energy
a	Interatomic spacing
D	Diffusion coefficient
E_{Ads}^s	Energy of adsorption of a metal adatom
E_{Tot}	Sum of activation energies for Ostwald Ripening
G	Gibbs free energy
H_{rs}	Energy barrier between a support site and the particle edge site
H_s	Activation energy for diffusion of the adatom on the substrate surface
J_r	Net rate at which single atoms attach to the nanoparticle from the substrate
J_s	Net rate at which single atoms diffuse toward the nanoparticle on the substrate
L	Distance for the adatom concentration to be a function of the average particle size
n_r	Refractive index
P	Pressure
$P(\Delta E)$	Probability of transition with activation energy ΔE
R	Microscope resolution
r	Radius
r_c	Critical particle radius, equal to mean particle radius
S	Entropy
S_A	Surface area
S_A	Signal from a single atom
S_B	Signal from the substrate
T	Temperature
t	Time
t_0	Extinction time, i.e. $t(r=0)$
V	Volume
V_{AB}	Rose Criterion
γ	Surface free energy

ΔH	Heat of sublimation of the metal
θ	Particle/support contact angle
λ	Wavelength
μ	Chemical potential
μ_{∞}	Chemical potential (bulk contribution)
μ_A	Chemical potential (surface contribution)
μ_r	Chemical potential (particle)
ν	Substrate site vibrational frequency
ν_r	Vibrational frequencies of atoms on the particle
ν_s	Vibrational frequencies of atoms on the support
ρ'_s	Adatom concentration close to the particle
ρ_{∞}	Concentration of adatoms on the substrate in equilibrium with an infinitely sized particle
ρ_{local}	Local atomic concentration
ρ_r	Concentration of adatoms on the edge of the particle
ρ_s	Concentration of adatoms on the substrate sites adjacent to the particle
σ	Standard deviation
ϕ	Semi-angle of collection
Ω	Atomic volume
ϵ_j	Set of mutually independent random variables
w	Angular coverage

Bibliography

1. Simonsen, S.B., et al., *Sintering of oxide-supported Pt and Pd nanoparticles in air studied by in situ TEM*. Technical University of Denmark, Haldor Topsoe
2. Krivanek, O., N. Dellby, and A. Lupini, *Towards sub-Å electron beams*. *Ultramicroscopy*, 1999. **78**(1): p. 1-11.
3. Haider, M., et al., *Electron microscopy image enhanced*. *Nature*, 1998. **392**(6678): p. 768-769.
4. Boyes, E. and P. Gai, *Environmental high resolution electron microscopy and applications to chemical science*. *Ultramicroscopy*, 1997. **67**(1): p. 219-232.
5. Allard, L.F., et al., *Novel MEMS-based gas-cell/heating specimen holder provides advanced imaging capabilities for in situ reaction studies*. *Microscopy and Microanalysis*, 2012. **18**(04): p. 656-666.
6. Zhang, S., et al., *In-situ studies of nanocatalysis*. *Accounts of chemical research*, 2013. **46**(8): p. 1731-1739.
7. D B Williams, C.B.C., *Transmission Electron Microscopy*. 1996: Plenum Press.
8. Hirsch, P.B., *Electron Microscopy of Thin Crystals*. 1965: Butterworths.
9. Pennycook, S.J. and P.D. Nellist, *Scanning transmission electron microscopy: imaging and analysis*. 2011: Springer Science & Business Media.
10. Edington, J.W., *Practical Electron Microscopy in Materials Science. 3. Interpretation of Transmission Electron Micrographs*. Macmillan Press, 1975, 1975.
11. Hutchinson, A.I.K.a.J.L., *Nanocharacterisation*. 2007: Royal Society of Chemistry.
12. Walsh, M.J., *Aberration corrected In-Situ Electron Microscopy of Nanoparticle Catalysts*, in *Department of Physics*. 2012, University of York: York.
13. Crewe, A.V., J. Wall, and J. Langmore, *Visibility of single atoms*. *Science*, 1970. **168**(3937): p. 1338-1340.
14. Hytch, M. and W. Stobbs, *Quantitative comparison of high resolution TEM images with image simulations*. *Ultramicroscopy*, 1994. **53**(3): p. 191-203.
15. Batson, P., N. Dellby, and O. Krivanek, *Sub-ångstrom resolution using aberration corrected electron optics*. *Nature*, 2002. **418**(6898): p. 617-620.
16. Pennycook, S.J., et al., *Scanning Transmission Electron Microscopy for Nanostructure Characterization*, in *Scanning Microscopy for Nanotechnology*, W. Zhou and Z. Wang, Editors. 2007, Springer New York. p. 152-191.
17. Gabor, D., *A new microscopic principle*. *Nature*, 1948. **161**(4098): p. 777-778.
18. Kirkland, A.I. and R.R. Meyer, *"Indirect" High-Resolution Transmission Electron Microscopy: Aberration Measurement and Wavefunction Reconstruction*. *Microscopy and Microanalysis*, 2004. **10**(04): p. 401-413.
19. Coene, W., et al., *Maximum-likelihood method for focus-variation image reconstruction in high resolution transmission electron microscopy*. *Ultramicroscopy*, 1996. **64**(1): p. 109-135.
20. Scherzer, O., *Sphärische und chromatische korrektur von elektronen-linsen*. *Optik*, 1947. **2**: p. 114-132.
21. Bleloch, A. and A. Lupini, *Imaging at the picoscale*. *Materials Today*, 2004. **7**(12): p. 42-48.

22. Christensen, C.H. and J.K. Nørskov, *A molecular view of heterogeneous catalysis*. The Journal of chemical physics, 2008. **128**(18): p. 182503-182503-8.
23. Creemer, J., et al., *Atomic-scale electron microscopy at ambient pressure*. Ultramicroscopy, 2008. **108**(9): p. 993-998.
24. De Jonge, N., W.C. Bigelow, and G.M. Veith, *Atmospheric pressure scanning transmission electron microscopy*. Nano letters, 2010. **10**(3): p. 1028-1031.
25. Mehraeen, S., et al., *A (S) TEM Gas Cell Holder with Localized Laser Heating for In Situ Experiments*. Microscopy and Microanalysis, 2013. **19**(02): p. 470-478.
26. Banhart, F., *In-situ electron microscopy at high resolution*. 2008: World Scientific.
27. Boyes, E.D. and P.L. Gai, *Environmental high resolution electron microscopy and applications to chemical science*. Ultramicroscopy, 1997. **67**(1-4): p. 219-232.
28. Hansen, T.W., et al., *Atomic-resolution in situ transmission electron microscopy of a promoter of a heterogeneous catalyst*. Science, 2001. **294**(5546): p. 1508-1510.
29. Hansen, T.W., J.B. Wagner, and R.E. Dunin-Borkowski, *Aberration corrected and monochromated environmental transmission electron microscopy: challenges and prospects for materials science*. Materials Science and Technology, 2010. **26**(11): p. 1338-1344.
30. Jinschek, J., *Advances in the environmental transmission electron microscope (ETEM) for nanoscale in situ studies of gas-solid interactions*. Chemical Communications, 2014. **50**(21): p. 2696-2706.
31. Yoshida, K., A. Bright, and N. Tanaka, *Direct observation of the initial process of Ostwald ripening using spherical aberration-corrected transmission electron microscopy*. Journal of electron microscopy, 2012. **61**(2): p. 99-103.
32. Boyes, E.D., et al., *ESTEM imaging of single atoms under controlled temperature and gas environment conditions in catalyst reaction studies*. Annalen der Physik, 2013. **525**(6): p. 423-429.
33. Boyes, E.D. and P.L. Gai, *Visualising reacting single atoms under controlled conditions: Advances in atomic resolution in situ Environmental (Scanning) Transmission Electron Microscopy (E (S) TEM)*. Comptes Rendus Physique, 2014. **15**(2): p. 200-213.
34. Thomas, J., Z. Saghi, and P. Gai, *Can a Single Atom Serve as the Active Site in Some Heterogeneous Catalysts?* Topics in Catalysis, 2011. **54**(10-12): p. 588-594.
35. Yang, X.-F., et al., *Single-Atom Catalysts: A new Frontier in heterogeneous catalysis*. Accounts of chemical research, 2013. **46**(8): p. 1740-1748.
36. Gai, P.L., et al., *Visualisation of single atom dynamics and their role in nanocatalysts under controlled reaction environments*. Chemical Physics Letters, 2014. **592**: p. 355-359.
37. Qiao, B., et al., *Single-atom catalysis of CO oxidation using Pt1/FeOx*. Nat Chem, 2011. **3**(8): p. 634-641.
38. Ranocchiari, M., et al., *Single-atom active sites on metal-organic frameworks*. Proceedings of the Royal Society A: Mathematical, Physical and Engineering Science, 2012. **468**(2143): p. 1985-1999.
39. Sun, S., et al., *Single-atom Catalysis Using Pt/Graphene Achieved through Atomic Layer Deposition*. Sci. Rep., 2013. **3**.
40. Boyes, E. and P. Gai. *Aberration corrected environmental STEM (AC ESTEM) for dynamic in-situ gas reaction studies of nanoparticle catalysts*. in *Journal of Physics: Conference Series*. 2014. IOP Publishing.
41. Gai, P.L., Boyes, E, *Electron Microscopy in Heterogeneous Catalysis*. 2003, Institute of Physics.
42. Hansen, T.W., *Sintering and Particle dynamics in Supported Metal Catalysts*. 2006, Technical University of Denmark: Lynberg.
43. Wynblatt, P. and N. Gjostein, *Supported metal crystallites*. Progress in solid state chemistry, 1975. **9**: p. 21-58.
44. Simonsen, S.B., et al., *Ostwald ripening in a Pt/SiO2 model catalyst studied by in situ TEM*. Journal of Catalysis, 2011. **281**(1): p. 147-155.

45. Simonsen, S.B., et al., *Effect of particle morphology on the ripening of supported Pt nanoparticles*. The Journal of Physical Chemistry C, 2012. **116**(9): p. 5646-5653.
46. Hansen, T.W., et al., *Sintering of Catalytic Nanoparticles: Particle Migration or Ostwald Ripening?* Accounts of chemical research, 2013.
47. Finsy, R., *On the critical radius in Ostwald ripening*. Langmuir, 2004. **20**(7): p. 2975-2976.
48. Datye, A.K., et al., *Particle size distributions in heterogeneous catalysts: What do they tell us about the sintering mechanism?* Catalysis today, 2006. **111**(1): p. 59-67.
49. Lifshitz, I.M. and V.V. Slyozov, *The kinetics of precipitation from supersaturated solid solutions*. Journal of Physics and Chemistry of Solids, 1961. **19**(1): p. 35-50.
50. Granqvist, C. and R. Buhrman, *Size distributions for supported metal catalysts: Coalescence growth versus ostwald ripening*. Journal of Catalysis, 1976. **42**(3): p. 477-479.
51. Nichols, F., *Coalescence of two spheres by surface diffusion*. Journal of Applied Physics, 1966. **37**(7): p. 2805-2808.
52. Ruckenstein, E. and B. Pulvermacher, *Growth kinetics and the size distributions of supported metal crystallites*. Journal of Catalysis, 1973. **29**(2): p. 224-245.
53. De Smet, Y., L. Deriemaeker, and R. Finsy, *A simple computer simulation of Ostwald ripening*. Langmuir, 1997. **13**(26): p. 6884-6888.
54. De Smet, Y., et al., *Ostwald ripening in the transient regime: a cryo-TEM study*. Langmuir, 2000. **16**(3): p. 961-967.
55. Wanke, S.E., *Comments on the sintering mechanism of supported metal catalysts*. Journal of Catalysis, 1977. **46**(2): p. 234-237.
56. Su, D.S., B. Zhang, and R. Schlögl, *Electron Microscopy of Solid Catalysts - Transforming from a Challenge to a Toolbox*. Chemical reviews, 2015.
57. Sohlberg, K., et al., *Insights into the physical chemistry of materials from advances in HAADF-STEM*. Physical Chemistry Chemical Physics, 2015.
58. Jak, M., et al., *Scanning tunnelling microscopy study of the growth of small palladium particles on TiO₂(110)*. Surface science, 2000. **457**(3): p. 295-310.
59. Fuentes, G.A. and E. Salinas-Rodríguez, *Realistic particle size distributions during sintering by Ostwald ripening*. Studies in Surface Science and Catalysis, 2001. **139**: p. 503-510.
60. Wettergren, K., et al., *High sintering resistance of size-selected platinum cluster catalysts by suppressed ostwald ripening*. Nano letters, 2014. **14**(10): p. 5803-5809.
61. Simonsen, S.B., et al., *Direct observations of oxygen-induced platinum nanoparticle ripening studied by in situ TEM*. Journal of the American Chemical Society, 2010. **132**(23): p. 7968-7975.
62. Morgenstern, K., et al., *Stability of two-dimensional nanostructures*. Applied Physics A, 1999. **69**(5): p. 559-569.
63. Morgenstern, K., G. Rosenfeld, and G. Comsa, *Decay of two-dimensional Ag islands on Ag (111)*. Physical review letters, 1996. **76**(12): p. 2113.
64. Morgenstern, K., G. Rosenfeld, and G. Comsa, *Local correlation during Ostwald ripening of two-dimensional islands on Ag (111)*. Surface science, 1999. **441**(2): p. 289-300.
65. Bartelt, N., W. Theis, and R. Tromp, *Ostwald ripening of two-dimensional islands on Si (001)*. Physical Review B, 1996. **54**(16): p. 11741.
66. Theis, W., N. Bartelt, and R. Tromp, *Chemical potential maps and spatial correlations in 2D-island ripening on Si (001)*. Physical review letters, 1995. **75**(18): p. 3328.
67. Campbell, C.T., S.C. Parker, and D.E. Starr, *The effect of size-dependent nanoparticle energetics on catalyst sintering*. Science, 2002. **298**(5594): p. 811-814.
68. Ouyang, R., J.-X. Liu, and W.-X. Li, *Atomistic Theory of Ostwald Ripening and Disintegration of Supported Metal Particles under Reaction Conditions*. Journal of the American Chemical Society, 2013. **135**(5): p. 1760-1771.

69. Yang, F., M. Chen, and D. Goodman, *Sintering of Au particles supported on TiO₂ (110) during CO oxidation*. The Journal of Physical Chemistry C, 2008. **113**(1): p. 254-260.
70. Di Vece, M., et al., *Hydrogen-induced ostwald ripening at room temperature in a Pd nanocluster film*. Physical review letters, 2008. **100**(23): p. 236105.
71. Fukamori, Y., et al., *Fundamental Insight into the Substrate-Dependent Ripening of Monodisperse Clusters*. ChemCatChem, 2013. **5**(11): p. 3330-3341.
72. Alloyeau, D., et al., *Ostwald ripening in nanoalloys: when thermodynamics drives a size-dependent particle composition*. Physical review letters, 2010. **105**(25): p. 255901.
73. Heinemann, K. and F. Soria, *On the detection and size classification of nanometer-size metal particles on amorphous substrates*. Ultramicroscopy, 1986. **20**(1): p. 1-14.
74. Datye, A.K., *Electron microscopy of catalysts: recent achievements and future prospects*. Journal of Catalysis, 2003. **216**(1): p. 144-154.
75. Zhang, B., W. Zhang, and D.S. Su, *Towards a More Accurate Particle Size Distribution of Supported Catalyst by using HAADF-STEM*. ChemCatChem, 2011. **3**(6): p. 965-968.
76. Challa, S.R., et al., *Relating rates of catalyst sintering to the disappearance of individual nanoparticles during Ostwald ripening*. J Am Chem Soc, 2011. **133**(51): p. 20672-5.
77. Starr, D.E., S.K. Shaikhutdinov, and H.-J. Freund, *Gold supported on oxide surfaces: environmental effects as studied by STM*. Topics in catalysis, 2005. **36**(1-4): p. 33-41.
78. Dent, A.J., et al., *Rhodium dispersion during NO/CO conversions*. Angewandte Chemie International Edition, 2007. **46**(28): p. 5356-5358.
79. Hansen, P.L., et al., *Atom-resolved imaging of dynamic shape changes in supported copper nanocrystals*. Science, 2002. **295**(5562): p. 2053-2055.
80. Zhou, J., et al., *Adsorbate-induced dissociation of metal clusters: TiO₂ (110)-supported Cu and Ni clusters exposed to oxygen gas*. Surface science, 2004. **562**(1): p. 113-127.
81. Kuechen, C. and U. Hoffmann, *Investigation of simultaneous reaction of carbon monoxide and carbon dioxide with hydrogen on a commercial copper/zinc oxide catalyst*. Chemical engineering science, 1993. **48**(22): p. 3767-3776.
82. Rasmussen, D.B., et al., *The energies of formation and mobilities of Cu surface species on Cu and ZnO in methanol and water gas shift atmospheres studied by DFT*. Journal of Catalysis, 2012. **293**: p. 205-214.
83. Judai, K., et al., *Low-Temperature Cluster Catalysis*. Journal of the American Chemical Society, 2004. **126**(9): p. 2732-2737.
84. Kyriakou, G., et al., *Isolated metal atom geometries as a strategy for selective heterogeneous hydrogenations*. Science(Washington), 2012. **335**(6073): p. 1209-1212.
85. Mao, K., et al., *A Theoretical Study of Single-Atom Catalysis of CO Oxidation Using Au Embedded 2D h-BN Monolayer: A CO-Promoted O₂ Activation*. Scientific reports, 2014. **4**.
86. Kwak, J.H., et al., *Coordinatively unsaturated Al³⁺ centers as binding sites for active catalyst phases of platinum on γ -Al₂O₃*. Science, 2009. **325**(5948): p. 1670-1673.
87. Liang, J.-X., et al., *Theoretical and Experimental Investigations on Single-Atom Catalysis: Ir₁/FeO_x for CO Oxidation*. The Journal of Physical Chemistry C, 2014. **118**(38): p. 21945-21951.
88. Tang, W., et al., *Methane complete and partial oxidation catalyzed by Pt-doped CeO₂*. Journal of Catalysis, 2010. **273**(2): p. 125-137.
89. Hackett, S.F., et al., *High-Activity, Single-Site Mesoporous Pd/Al₂O₃ Catalysts for Selective Aerobic Oxidation of Allylic Alcohols*. Angewandte Chemie, 2007. **119**(45): p. 8747-8750.
90. Zhai, Y., et al., *Alkali-stabilized Pt-OH_x species catalyze low-temperature water-gas shift reactions*. Science, 2010. **329**(5999): p. 1633-1636.
91. Wei, H., et al., *FeO_x-supported platinum single-atom and pseudo-single-atom catalysts for chemoselective hydrogenation of functionalized nitroarenes*. Nature communications, 2014. **5**.
92. Xing, J., et al., *Stable isolated metal atoms as active sites for photocatalytic hydrogen evolution*. Chemistry-A European Journal, 2014. **20**(8): p. 2138-2144.

93. Xing, J., et al., *Active sites on hydrogen evolution photocatalyst*. J. Mater. Chem. A, 2013. **1**(48): p. 15258-15264.
94. Shi, Y., et al., *Single-Atom Catalysis in Mesoporous Photovoltaics: The Principle of Utility Maximization*. Advanced Materials, 2014. **26**(48): p. 8147-8153.
95. Lin, J., et al., *Little do more: a highly effective Pt₁/FeO_x single-atom catalyst for the reduction of NO by H₂*. Chemical Communications, 2015.
96. Liu, Y., et al., *Highly active iron oxide supported gold catalysts for CO oxidation: how small must the gold nanoparticles be?* Angewandte Chemie International Edition, 2010. **49**(33): p. 5771-5775.
97. O'Mullane, A.P., *From single crystal surfaces to single atoms: investigating active sites in electrocatalysis*. Nanoscale, 2014. **6**(8): p. 4012-4026.
98. Wang, Y.-G., et al., *Dynamic formation of single-atom catalytic active sites on ceria-supported gold nanoparticles*. Nature communications, 2015. **6**.
99. Kunkes, E. and M. Behrens, *5.3 Methanol Chemistry*. Chemical Energy Storage, 2012.
100. Avgouropoulos, G., et al., *Reforming methanol to electricity in a high temperature PEM fuel cell*. Applied Catalysis B: Environmental, 2009. **90**(3): p. 628-632.
101. Papavasiliou, J., G. Avgouropoulos, and T. Ioannides, *CuMnOx catalysts for internal reforming methanol fuel cells: application aspects*. international journal of hydrogen energy, 2012. **37**(21): p. 16739-16747.
102. Rodriguez, J.A., et al., *Reduction of CuO in H₂: in situ time-resolved XRD studies*. Catalysis letters, 2003. **85**(3-4): p. 247-254.
103. Ciston, J., et al., *Morphological and Structural Changes during the Reduction and Reoxidation of CuO/CeO₂ and Ce_{1-x}Cu_xO₂ Nanocatalysts: In Situ Studies with Environmental TEM, XRD, and XAS*. The Journal of Physical Chemistry C, 2011. **115**(28): p. 13851-13859.
104. Kim, J.Y., et al., *Reduction of CuO and Cu₂O with H₂: H embedding and kinetic effects in the formation of suboxides*. Journal of the American Chemical Society, 2003. **125**(35): p. 10684-10692.
105. Wang, X., et al., *Time-resolved studies for the mechanism of reduction of copper oxides with carbon monoxide: complex behavior of lattice oxygen and the formation of suboxides*. The Journal of Physical Chemistry B, 2004. **108**(36): p. 13667-13673.
106. Gai, P.L., *Developments in in situ environmental cell high-resolution electron microscopy and applications to catalysis*. Topics in catalysis, 2002. **21**(4): p. 161-173.
107. Long, N.J. and A.K. Petford-Long, *In-situ electron-beam-induced reduction of CuO: A study of phase transformations in cupric oxide*. Ultramicroscopy, 1986. **20**(1): p. 151-159.
108. Zhou, W., I.E. Wachs, and C.J. Kiely, *Nanostructural and chemical characterization of supported metal oxide catalysts by aberration corrected analytical electron microscopy*. Current Opinion in Solid State and Materials Science, 2012. **16**(1): p. 10-22.
109. Pike, J., et al., *Formation of stable Cu₂O from reduction of CuO nanoparticles*. Applied Catalysis A: General, 2006. **303**(2): p. 273-277.
110. Thalinger, R., et al., *Formation and stability of small well-defined Cu- and Ni oxide particles*. Materials Chemistry and Physics, 2013. **143**(1): p. 184-194.
111. Yuan, L., et al., *CuO reduction induced formation of CuO/Cu₂O hybrid oxides*. Chemical Physics Letters, 2013. **590**(0): p. 92-96.
112. Huang, W., *Crystal plane-dependent surface reactivity and catalytic property of oxide catalysts studied with oxide nanocrystal model catalysts*. Topics in Catalysis, 2013. **56**(15-17): p. 1363-1376.
113. Bao, H., et al., *Shape-dependent reducibility of cuprous oxide nanocrystals*. The Journal of Physical Chemistry C, 2010. **114**(14): p. 6676-6680.
114. Behrens, M., *Meso- and nano-structuring of industrial Cu/ZnO/(Al₂O₃) catalysts*. Journal of Catalysis, 2009. **267**(1): p. 24-29.

115. Behrens, M., et al., *The potential of microstructural optimization in metal/oxide catalysts: higher intrinsic activity of copper by partial embedding of copper nanoparticles*. ChemCatChem, 2010. **2**(7): p. 816-818.
116. Behrens, M., et al., *The active site of methanol synthesis over Cu/ZnO/Al₂O₃ industrial catalysts*. Science, 2012. **336**(6083): p. 893-897.
117. Somorjai, G.A., et al., *The evolution of model catalytic systems; studies of structure, bonding and dynamics from single crystal metal surfaces to nanoparticles, and from low pressure (< 10⁻³ Torr) to high pressure (> 10⁻³ Torr) to liquid interfaces*. Physical Chemistry Chemical Physics, 2007. **9**(27): p. 3500-3513.
118. Yanase, A., et al., *Optical observation of oxidation and reduction of small supported copper particles*. Surface Science Letters, 1989. **219**(3): p. L601-L606.
119. Lee, S., et al., *Copper oxide reduction through vacuum annealing*. Applied Surface Science, 2003. **206**(1): p. 102-109.
120. Zhou, G. and J.C. Yang, *Temperature effect on the Cu₂O oxide morphology created by oxidation of Cu(0 0 1) as investigated by in situ UHV TEM*. Applied Surface Science, 2003. **210**(3-4): p. 165-170.
121. Liu, Y., Q. Fu, and M. Stephanopoulos, *Preferential oxidation of CO in H₂ over CuO-CeO₂ catalysts*. Catalysis Today, 2004. **93**: p. 241-246.
122. Fernández-García, M., et al., *Tracking down the reduction behavior of copper-on-alumina catalysts*. Journal of Catalysis, 1998. **178**(1): p. 253-263.
123. Svintsitskiy, D., et al., *Study of cupric oxide nanopowders as efficient catalysts for low-temperature CO oxidation*. Journal of Molecular Catalysis A: Chemical, 2013. **368**: p. 95-106.
124. Svintsitskiy, D.A., et al., *In situ XRD, XPS, TEM, and TPR study of highly active in CO oxidation CuO nanopowders*. The Journal of Physical Chemistry C, 2013. **117**(28): p. 14588-14599.
125. Holse, C., et al., *The Dynamic Behavior of CuZn Nanoparticles Under Oxidizing and Reducing Conditions*. The Journal of Physical Chemistry C, 2014.
126. Maimaiti, Y., M. Nolan, and S.D. Elliott, *Reduction mechanisms of the CuO (111) surface through surface oxygen vacancy formation and hydrogen adsorption*. Physical Chemistry Chemical Physics, 2014. **16**(7): p. 3036-3046.
127. Syed-Hassan, S.S.A. and C.Z. Li, *Effects of crystallite size on the kinetics and mechanism of NiO reduction with H₂*. International Journal of Chemical Kinetics, 2011. **43**(12): p. 667-676.
128. Richardson, J.T., R. Scates, and M.V. Twigg, *X-ray diffraction study of nickel oxide reduction by hydrogen*. Applied Catalysis A: General, 2003. **246**(1): p. 137-150.
129. Jeangros, Q., et al., *Reduction of nickel oxide particles by hydrogen studied in an environmental TEM*. Journal of Materials Science, 2013. **48**(7): p. 2893-2907.
130. Rodriguez, J.A., et al., *Physical and chemical properties of MoP, Ni₂P, and MoNiP hydrodesulfurization catalysts: Time-resolved X-ray diffraction, density functional, and hydrodesulfurization activity studies*. The Journal of Physical Chemistry B, 2003. **107**(26): p. 6276-6285.
131. Rodriguez, J.A., et al., *Experimental and theoretical studies on the reaction of H₂ with NiO: role of O vacancies and mechanism for oxide reduction*. Journal of the American Chemical Society, 2002. **124**(2): p. 346-354.
132. Kasatkin, I., et al., *Role of lattice strain and defects in copper particles on the activity of Cu/ZnO/Al₂O₃ catalysts for methanol synthesis*. Angewandte Chemie, 2007. **119**(38): p. 7465-7468.
133. Nagase, K., et al., *Dynamic study of the oxidation state of copper in the course of carbon monoxide oxidation over powdered CuO and Cu₂O*. Journal of Catalysis, 1999. **187**(1): p. 123-130.
134. Sá, S., et al., *Catalysts for methanol steam reforming—A review*. Applied Catalysis B: Environmental, 2010. **99**(1): p. 43-57.

135. Grunwaldt, J.-D., et al., *In situ investigations of structural changes in Cu/ZnO catalysts*. Journal of Catalysis, 2000. **194**(2): p. 452-460.
136. Kurtz, M., et al., *Deactivation of supported copper catalysts for methanol synthesis*. catalysis Letters, 2003. **86**(1-3): p. 77-80.
137. Bart, J. and R. Sneed, *Copper-zinc oxide-alumina methanol catalysts revisited*. Catalysis Today, 1987. **2**(1): p. 1-124.
138. Parker, S.C. and C.T. Campbell, *Kinetic model for sintering of supported metal particles with improved size-dependent energetics and applications to Au on TiO₂ (110)*. Physical Review B, 2007. **75**(3): p. 035430.
139. Ostwald, Z., *phys. 34, 405 (1900)*. Hulett, Z. phys, 1901. **37**: p. 385.
140. Wagner, C., *Ostwald ripening theory*. Ber. Bunsenges. Phys. Chem, 1961. **65**: p. 581-591.
141. Chakraverty, B., *Grain size distribution in thin films—1. Conservative systems*. Journal of Physics and Chemistry of Solids, 1967. **28**(12): p. 2401-2412.
142. Houk, L.R., et al., *The Definition of "Critical Radius" for a Collection of Nanoparticles Undergoing Ostwald Ripening*. Langmuir, 2009. **25**(19): p. 11225-11227.
143. Prévot, G., *Ostwald ripening of three-dimensional clusters on a surface studied with an ultrafast kinetic Monte Carlo algorithm*. Physical Review B, 2011. **84**(4): p. 045434.
144. Fitting, L., et al., *Influence of strain, surface diffusion and Ostwald ripening on the evolution of nanostructures for erbium on Si (001)*. Journal of applied physics, 2003. **93**(7): p. 4180-4184.
145. McLean, J.G., et al., *Decay of isolated surface features driven by the Gibbs-Thomson effect in an analytic model and a simulation*. Physical Review B, 1997. **55**(3): p. 1811.
146. Paal, Z. and P. Menon, *Hydrogen effects in catalysis*. M. Dekker, 1988.
147. Sushumna, I. and E. Ruckenstein, *Role of physical and chemical interactions in the behavior of supported metal catalysts: Iron on alumina—A case study*. Journal of catalysis, 1985. **94**(1): p. 239-288.
148. Chen, J.J. and E. Ruckenstein, *Sintering of palladium on alumina model catalyst in a hydrogen atmosphere*. Journal of Catalysis, 1981. **69**(2): p. 254-273.
149. Larsson, H. and J. Ågren, *A random-walk approach to diffusion controlled growth*. Scripta materialia, 2003. **49**(6): p. 521-526.
150. Vitos, L., et al., *The surface energy of metals*. Surface Science, 1998. **411**(1): p. 186-202.
151. Tyson, W. and W. Miller, *Surface free energies of solid metals: Estimation from liquid surface tension measurements*. Surface Science, 1977. **62**(1): p. 267-276.
152. Zhang, J.-M., F. Ma, and K.-W. Xu, *Calculation of the surface energy of FCC metals with modified embedded-atom method*. Applied Surface Science, 2004. **229**(1): p. 34-42.
153. Meier, G.H., *Thermodynamics of Surfaces and Interfaces: Concepts in Inorganic Materials*. 2014: Cambridge University Press.
154. Jia, M., et al., *Calculation of the surface free energy of fcc copper nanoparticles*. Modelling and Simulation in Materials Science and Engineering, 2009. **17**(1): p. 015006.
155. Stewart, K.L., *Copper Surface Chemistry Relevant to Chemical Mechanical Planarization (CMP)*. 2008: ProQuest.
156. Yang, L. and A.E. DePristo, *On the compact structure of small fcc metal clusters*. Journal of Catalysis, 1994. **149**(1): p. 223-228.
157. Schwind, M. and J. Ågren, *A random walk approach to Ostwald ripening*. Acta materialia, 2001. **49**(18): p. 3821-3828.
158. Lucas, S. and P. Moskovkin, *Simulation at high temperature of atomic deposition, islands coalescence, Ostwald and inverse Ostwald ripening with a general simple kinetic Monte Carlo code*. Thin Solid Films, 2010. **518**(18): p. 5355-5361.
159. Voter, A., *Introduction to Kinetic Monte Carlo Methods*, in *Radiation Effects in Solids*, K. Sickafus, E. Kotomin, and B. Uberuaga, Editors. 2007, Springer Netherlands. p. 1-23.

160. Yang, L., A. Karim, and J.T. Muckerman, *Density Functional Kinetic Monte Carlo Simulation of Water–Gas Shift Reaction on Cu/ZnO*. The Journal of Physical Chemistry C, 2013. **117**(7): p. 3414-3425.
161. Larsson, M.I., *Kinetic monte carlo simulations of adatom island decay on cu (111)*. Physical Review B, 2001. **64**(11): p. 115428.
162. Pomeroy, J.M., et al., *Kinetic Monte Carlo–molecular dynamics investigations of hyperthermal copper deposition on Cu (111)*. Physical Review B, 2002. **66**(23): p. 235412.
163. Morgenstern, K., E. Lægsgaard, and F. Besenbacher, *Motion of vacancy islands on an anisotropic surface: Theory and kinetic Monte Carlo simulations*. Physical Review B, 2002. **66**(11): p. 115408.
164. Zoontjens, P., et al., *A kinetic Monte Carlo study of Pt on Au (111) with applications to bimetallic catalysis*. Journal of Physics: Condensed Matter, 2011. **23**(1): p. 015302.
165. Šljivančanin, Ž. and B. Hammer, *Oxygen dissociation at close-packed Pt terraces, Pt steps, and Ag-covered Pt steps studied with density functional theory*. Surface science, 2002. **515**(1): p. 235-244.
166. Van Hardeveld, R. and F. Hartog, *The statistics of surface atoms and surface sites on metal crystals*. Surface Science, 1969. **15**(2): p. 189-230.
167. Sun, J.T., I.S. Metcalfe, and M. Sahibzada, *Deactivation of Cu/ZnO/Al₂O₃ methanol synthesis catalyst by sintering*. Industrial & engineering chemistry research, 1999. **38**(10): p. 3868-3872.
168. Martínez-Suárez, L., J. Frenzel, and D. Marx, *Cu/ZnO nanocatalysts in response to environmental conditions: surface morphology, electronic structure, redox state and CO₂ activation*. Physical Chemistry Chemical Physics, 2014.
169. Jalili, S., et al., *Molecular dynamics simulation of a graphite-supported copper nanocluster: thermodynamic properties and gas adsorption*. Molecular Physics, 2012. **110**(5): p. 267-276.
170. Shih, T.-S. and Z.-B. Liu, *Thermally-formed oxide on aluminum and magnesium*. Materials transactions, 2006. **47**(5): p. 1347-1353.
171. Doherty, P. and R. Davis, *Direct Observation of the Oxidation of Aluminum Single-Crystal Surfaces*. Journal of Applied Physics, 1963. **34**(3): p. 619-628.
172. Beck, A., et al., *The kinetics of the oxidation of Al in oxygen at high temperature*. Corrosion science, 1967. **7**(1): p. 1-22.
173. Eldridge, J., et al., *Thermal oxidation of single-crystal aluminum at 550 C*. Oxidation of metals, 1988. **30**(5-6): p. 301-328.
174. Chen, J.J. and E. Ruckenstein, *Role of interfacial phenomena in the behavior of alumina-supported palladium crystallites in oxygen*. The Journal of Physical Chemistry, 1981. **85**(11): p. 1606-1612.
175. Menon, P. and G. Froment, *Modification of the properties of Pt Al₂O₃ catalysts by hydrogen at high temperatures*. Journal of Catalysis, 1979. **59**(1): p. 138-147.
176. Rizza, G., et al., *Ion irradiation of gold inclusions in SiO₂: Experimental evidence for inverse Ostwald ripening*. Nuclear Instruments and Methods in Physics Research Section B: Beam Interactions with Materials and Atoms, 2001. **178**(1): p. 78-83.
177. Heinig, K.-H., et al. *Inverse Ostwald ripening and self-organization of nanoclusters due to ion irradiation*. in *MRS Proceedings*. 2000. Cambridge Univ Press.
178. Burlakov, V., et al., *Reversing Ostwald Ripening*. arXiv preprint arXiv:1412.6280, 2014.
179. Xia, Y., et al., *Shape-Controlled Synthesis of Metal Nanocrystals: Simple Chemistry Meets Complex Physics?* Angewandte Chemie International Edition, 2009. **48**(1): p. 60-103.
180. LaGrow, A.P., et al., *Synthesis, alignment, and magnetic properties of monodisperse nickel nanocubes*. Journal of the American Chemical Society, 2011. **134**(2): p. 855-858.
181. Zhdanov, V.P., E.M. Larsson, and C. Langhammer, *Novel aspects of Ostwald ripening of supported metal nanoparticles*. Chemical Physics Letters, 2012. **533**: p. 65-69.

182. Harris, P., *Growth and structure of supported metal catalyst particles*. International materials reviews, 1995. **40**(3): p. 97-115.
183. Tabib Zadeh Adibi, P., et al., *Transient Bimodal Particle Size Distributions During Pt Sintering on Alumina and Silica*. The Journal of Physical Chemistry C, 2014.
184. Petersen, M., A. Zangwill, and C. Ratsch, *Homoeptaxial ostwald ripening*. Surface science, 2003. **536**(1): p. 55-60.
185. Alloyeau, D., et al., *Following Ostwald ripening in nanoalloys by high-resolution imaging with single-atom chemical sensitivity*. Applied Physics Letters, 2012. **101**(12): p. 121920.
186. Morgenstern, K., *Fast scanning tunnelling microscopy as a tool to understand changes on metal surfaces: from nanostructures to single atoms*. physica status solidi (b), 2005. **242**(4): p. 773-796.
187. Slater, J.C., *Atomic radii in crystals*. The Journal of Chemical Physics, 1964. **41**(10): p. 3199-3204.
188. Rose, A., *The sensitivity performance of the human eye on an absolute scale*. JOSA, 1948. **38**(2): p. 196-208.
189. Batson, P.E., *Motion of gold atoms on carbon in the aberration-corrected STEM*. Microscopy and Microanalysis, 2008. **14**(01): p. 89-97.
190. Helveg, S., et al., *Observing gas-catalyst dynamics at atomic resolution and single-atom sensitivity*. Micron, 2015. **68**: p. 176-185.
191. Woehl, T.J., et al., *Direct in situ determination of the mechanisms controlling nanoparticle nucleation and growth*. ACS nano, 2012. **6**(10): p. 8599-8610.
192. Li, L., et al., *Noncrystalline-to-Crystalline Transformations in Pt Nanoparticles*. Journal of the American Chemical Society, 2013. **135**(35): p. 13062-13072.
193. Behafarid, F., et al., *An in situ transmission electron microscopy study of sintering and redispersion phenomena over size-selected metal nanoparticles: environmental effects*. Physical Chemistry Chemical Physics, 2014. **16**(34): p. 18176-18184.
194. Cameron, D.S., *Fuel Cells Science and Technology 2010*. Platinum Metals Rev, 2011. **55**(2): p. 108-116.
195. Hu, S., et al., *Proton transport through one-atom-thick crystals*. Nature, 2014.
196. Larsson, E.M., et al., *Real time indirect nanoplasmonic in situ spectroscopy of catalyst nanoparticle sintering*. ACS Catalysis, 2012. **2**(2): p. 238-245.
197. Prestat, E., et al., *Coarsening of Pt nanoparticles on amorphous carbon film*. Surface Science, 2013. **609**: p. 195-202.
198. Bals, S., et al., *Annular dark field imaging in a TEM*. Solid State Communications, 2004. **130**(10): p. 675-680.
199. Dupouy, G., *Contrast improvement in electron microscopic images of amorphous objects*. Journal of electron microscopy, 1967. **16**(1): p. 5-16.